X-Ray Absorption Spectroscopy of Actinide Speciation in Solid Solutions

by

Virginia Curran

SB, Nuclear Engineering
Massachusetts Institute of Technology (1999)

SM Nuclear Engineering
Massachusetts Institute of Technology (2001)

Submitted to the Department of Nuclear Engineering
in Partial Fulfillment of the Requirements for the Degree of
Doctor of Science in Nuclear Chemical Engineering and Waste Management

at the

Massachusetts Institute of Technology

September 2003

Signature of Author.....
Department of Nuclear Engineering
June 11, 2001

Certified by.....
Kenneth R. Czerwinski
Associate Professor of Nuclear Engineering
Thesis Supervisor

Certified by.....
Patrick G. Allen
Lawrence Livermore National Laboratory
Thesis Reader

Accepted by.....
Jeffrey A. Coderre
Chairman, Graduate Thesis Committee

X-Ray Absorption Spectroscopy of Actinide Speciation in Solid Solutions

by

Virginia Curran

Submitted to the Department of Nuclear Engineering

on 11 June 2003 in Partial Fulfillment of the Requirements

for the Degree of Doctor of Science in Nuclear Chemical Engineering

Abstract

It is widely recognized that the behavior of actinides in the environment is dictated by their speciation, or chemical form. It is therefore imperative to have a clear understanding of a waste form or environmental contaminant in order to effectively assess and treat the affected area. Current methodology utilizes the distribution coefficient (K_d), a rough measure of contaminant mobility in environmental systems, however neither the empirical nor theoretical determination of K_d is well defined. Although we understand the limitation of the K_d parameter, the reality is that the K_d is often the only parameter used in environmental fate and transport models to account for the mobile fraction of contaminate in predicting total risk. A fresh approach to the problem incorporating speciation that can be applied to a wide range of conditions is required.

X-ray absorption spectroscopy (XAS), a nondestructive technique that is ideal for determining the molecular composition of materials in dilute quantities in solution and solid forms, was used to determine the speciation of actinides in various solid nuclear materials including nuclear fuel, environmental contaminants, and advanced nuclear materials. This data could then be applied to individual systems to evaluate the environmental impact of the material via empirical or theoretical modeling. The fuels examined include Th_3UO_8, UC and a mixture of UC and US. In addition, an actual contaminant, metallic uranium-bearing samples recovered from the environment several decades after their accidental formation, was evaluated. The technique was also used to determine the structure of actinide templated resins and evaluate their reusability, and to look at the mechanism of uranium sorption to the metal reducing bacteria *Shewanella oneidensis*.

The results show that current methods for evaluating actinide transport/solubility in the environment do not accurately predict the empirical results. Our speciation method is shown to produce equilibrium data that can be used to develop more accurate K_d determination and to validate environmental models. This combination of empirical laboratory methods and speciation modeling improves upon current environmental remediation methods, and provides an improvement over direct K determinations. The method can also be used with advanced remediation techniques to target the critical actinide chemical forms that require treatment.

Thesis Supervisor:	Ken Czerwinski
Title:	Associate Professor, Nuclear Engineering
Thesis Reader:	Dr. Patrick G. Allen
Title:	Deputy Division Leader for Science, Chemical Engineering Division Chemistry and Materials Science Directorate Lawrence Livermore National Laboratory

Acknowledgements

Part of this work was performed under the auspices of the U.S. Department of Energy (DOE) by the University of California Lawrence Livermore National Laboratory under Contract No. W-7405-Eng-48. This work was done (partially) at SSRL, which is operated by the Department of Energy, Division of Chemical Sciences. The thorium-uranium solids work was funded partially by Idaho National Engineering and Environmental Laboratory under the auspices of the University Research Consortium and LDRD. This work was also partially funded by the Seaborg Institute for Transactinium Science at Lawrence Livermore National Laboratory through the Darlene Hoffman Fellowship. Supplemental funding was provided by the American Nuclear Society through the scholarship program, including but not limited to the Pittsburg Local Section scholarship.

The thorium-uranium solids work was performed with the assistance of Wendy Rattray and Yoann Sevestre of the Actinide Research Group. XAS data was collected with the assistance of Erik Nelson at Lawrence Livermore National Laboratory, as well as Karen Noyes and Lisa Mullen of the Actinide Research Group. The uranium carbide and sulfide solids were prepared by Jonathan Plaue, also of the Actinide Research group. Resins were prepared by Karen Noyes, bacteria were inoculated and fed uranium and killed and packed and shipped by Lisa Mullen. Victoria Anderson dissolved the U_3O_8. Marc Vial contributed the Np speciation data. Major Dan Caputo, PhD, CHP, provided the U slag samples.

Dedicated to Joe, the love of my life, who toiled away at Sea Grant for three years so that I could pursue this degree. I'm sorry we won't be able to stay in MA long enough for you to get your PhD at MIT. Maybe I could convince the Company to move here...

Table of Contents

List of Figures

List of Tables

1 Summary

1.1 Abstract

It is widely recognized that the behavior of actinides in the environment is dictated by their speciation, or chemical form. It is therefore imperative to have a clear understanding of a waste form or environmental contaminant in order to effectively assess and treat the affected area. Current methodology utilizes the distribution coefficient (K_d), a rough measure of contaminant mobility in environmental systems, however neither the empirical nor theoretical determination of K_d is well defined. Although we understand the limitation of the K_d parameter, the reality is that the K_d is often the only parameter used in environmental fate and transport models to account for the mobile fraction of contaminate in predicting total risk. A fresh approach to the problem incorporating speciation that can be applied to a wide range of conditions is introduced.

X-ray absorption spectroscopy (XAS), a nondestructive technique that is ideal for determining the molecular composition of materials in dilute quantities in solution and solid forms, was used to determine the speciation of actinides in various solid nuclear materials including nuclear fuel, environmental contaminants, and advanced nuclear materials. This data could then be applied to individual systems to evaluate the environmental impact of the material via empirical or theoretical modeling. The fuels examined include Th_3UO_8, UC, and a mixture of UC and US. In addition, an actual contaminant, metallic uranium-bearing samples recovered from the environment several decades after their accidental formation, was evaluated. The technique was also used to determine the structure of actinide templated resins and evaluate their reusability, and to look at the mechanism of uranium sorption to the metal reducing bacteria *Shewanella oneidensis*.

The results show that current methods for evaluating actinide transport/solubility in the environment do not accurately predict the empirical results. This speciation method is shown to produce equilibrium data that can be used to develop more accurate K_d determination and to validate environmental models. This combination of empirical laboratory methods and speciation modeling improves upon current environmental remediation methods, and provides an improvement over direct K_d determinations. The method can also be used with advanced remediation techniques to target the critical actinide chemical forms that require treatment.

1.2 Introduction

Current methods for evaluating the fate and transport of actinides in the environment are inadequate. The majority of environmental transport codes, including those used in the safety analysis for the Yucca Mountain Project, rely on a distribution coefficient, K_d. It is an attempt to describe the speciation of a contaminant with respect to solubility at a specific site without requiring any specific knowledge of the chemistry, geology, or biology of the local environment. The soluble fraction is usually considered to have the most impact on remediation of a site, since this is typically both the most mobile and the most toxic form of a contaminant. The distribution coefficient is determined by taking the ratio of the contaminant present in the solution phase of a sample over the contaminant present in the solid phase.

Typical methods for determining K_d consist of removing samples of sediment and local waters from the vicinity of the contaminated site. The number of samples is usually quite low and represents a small fraction of the actual contaminated area. The solid and solution phases of the samples are separated, and then individually exposed to the contaminant for a limited amount of time. The amount of contaminant present in each phase is then measured. Frequently the experimental contaminant source term is not related to the actual source term except for the presence of the element of interest. There is also usually no attempt to verify that equilibrium has been achieved.

Measurements of the K_d parameter are highly variable and unpredictable due to differences in soil composition from the various phases present and changes in aqueous conditions through a site. These variations can be large over affected areas, as pH, ionic strength, and the available concentrations of the polluting actinide and other solids present in the aqueous phase can change, as well as the phase composition of the local soil and sedimentation. Subsequent measurements of a

system therefore can differ greatly from initial results. In addition, K_d measurements cannot take into account evolution of the contaminated site over time. Distribution coefficients will change as the seasons change, and will also be affected by longer term changes in climate patterns such as droughts. There will also be changes on shorter time scales as, for example, the K_d measured from samples taken after a few days of rain can vary greatly from that taken during drier weather.

Complementing solution chemistry knowledge with the actual chemical speciation of the source term provides unique information for each system and therefore a much more accurate assessment of the environmental impact and provides cues as to the most expedient methods to reduce the risk to the environment and the local population. X-ray absorption fine structure spectroscopy (XAFS) provides an extremely useful tool for determining the speciation of an element in a diverse array of materials at low concentrations.

1.2.1 Research goals and objectives

In order to show that combining knowledge of the actinide speciation in the source material with knowledge of the environmental and geochemistry of the affected site using x-ray absorption spectroscopy is a useful technique that can be universally applied, a wide range of actinide-bearing solids was analyzed. The first objective was to apply the methodology to a simulated nuclear fuel and use it to assess its suitability for repository disposal. A thoria-based fuel was used for this analysis. In addition, the uranium carbide-sulfide system was also analyzed.

The second objective was to show that this methodology could be widely applied. Two diverse actinide-bearing materials were used to show this – actinide templated resins designed to increase selectivity for individual actinide ions during separations, and uranium reducing bacteria. The final objective was to apply the methodology to a real world environmental remediation project.

1.2.2 *Research tasks*

In order to achieve the goals described in the previous section, a series of tasks were undertaken. A description of each task is listed below. Tasks 1 and 2 consider speciation of actinides in nuclear reactor fuels. The fuel in Task 1 is fully analyzed using the methodology developed in this thesis from structure of the fuel to subsequent effects of the radiation environment in the repository on fuel dissolution. Task 3 analyzes the speciation of actinides in materials that affect their environmental impact. Task 4 is a culmination of the work that assesses the speciation and impact of an actual actinide source term that existed in the environment for some time before analysis.

1.3 Background

Since the advent of the Manhattan project, significant amounts of actinides and other radionuclides have been released into the environment unchecked through a combination of carelessness and ignorance of their long term impact. Sources of this extensive contamination throughout the geosphere are typically attributed to nuclear weapons tests and the nuclear weapons manufacturing infrastructure, though commercial nuclear accidents and manufacture and use of radioactive sources are also a major contributor. In addition, as the world moves toward deep geologic disposal of nuclear reactor waste, a large new potential source of radioactive contamination will be introduced in the form of spent nuclear fuel and other products of the nuclear fuel cycle. The actinides are of special concern because of their long half-lives, high toxicity, and complex physical and chemical properties [1]. Knowledge of the speciation of the actinides in the source term as well as interactions in the local environment is key to understanding and effectively remediation of

actinide contaminated sites. X-ray absorption spectroscopy is a nondestructive technique capable of determining actinide speciation in a complex matrix.

1.3.1 *Actinide speciation in the environment*

The main transport mechanism for actinides in the environment is water, therefore fate and transport depends largely on solution chemistry. Although actinide solubility tends to be lowest at the neutral pH of natural waters, a number of possible interactions can affect this. All of these processes are heavily influenced by the oxidation state of the actinide. The oxidation state will, in turn, be dictated by the environmental conditions, including pH and Eh of the natural waters and in some cases the ligands available for complexation. Because the stability of oxidation states in natural waters varies from actinide to actinide, the fate and transport of each actinide in a system will in turn differ.

The unique chemistry of the actinides leads to a large array of possible oxidation states for many in the series, ranging from +2 to +7. Actinides do not exist as free ions in the +5 or +6 states, instead they form unique stable "actinyl" species AnO_2^+ and AnO_2^{2+} which act as a unit in chemical reactions.

The most important interactions of actinides in the environment are precipitation, complexation, sorption, and colloid formation [2]. Precipitation, which occurs when actinide concentrations exceed their solubility limit, limits migration by removing actinides from solution. The tetravalent state is generally orders of magnitude less soluble than the other states. Actinides can also interact with naturally occurring inorganic and organic ligands found in ground waters creating complexes.

Complexation effectively enhances the solubility of the actinide by increasing the amount of actinide in solution, and therefore tends to increase release and migration rates. Common inorganic ligands available in natural waters include in

decreasing order of complexation are OH^-, CO_3^{2-}, SO_4^{2-}, PO_4^{3-}, and Cl^-. Complexation with the carbonate and hydroxyl ligands is the most important chemical reactions in environmental systems due to their ubiquitous presence in ground waters and strong complexation with actinide cations. The trend in strength of complexation of actinides to the various ligands with respect to oxidation state in decreasing order is +4 , +3 , +6 , and +5.

Migration of free actinides in solution and actinide complexed ions can be retarded by sorption to minerals and solids available in the local environment. Sorption can be both reversible and irreversible. Actinide colloids, small agglomerates of molecules that can range in size from less than 20 nm to over 200 nm, can also form in the environment. Depending on the nature of the colloid and the local environment, colloids can both enhance and retard actinide migration. Trivalent and tetravalent actinides have the greatest tendency to form colloids, followed by hexavalent and pentavalent ions [3].

1.3.2 X-ray absorption spectroscopy

X-ray absorption spectroscopy (XAS) is a technique that uses x-ray interactions to probe molecular structure of materials. XAS does not require long range order, so samples can be crystalline or amorphous, and can be in solid form, solution, or even gaseous. It is a highly specific technique that can individually probe the local structure surrounding each element in a sample. As such, it sees the global, average structure of the sample exposed to the x-ray beam with respect to a specific element.

1.3.2.1 Principles of X-Ray Absorption Spectroscopy

X-Ray Absorption Spectroscopy utilizes a tunable x-ray source to probe local structure of molecules, such as the identity, coordination number, and distance of atoms bonded to a core element of interest. Synchrotrons are typically chosen for the x-ray source due to their high energies and broad spectral ranges. Spectra obtained through XAS can be divided into two basic regions, X-ray Absorption Near Edge Structure (XANES) and Extended X-ray absorption Fine Structure (EXAFS).

The XANES portion of the spectra extends from the threshold to about 40 eV beyond the absorption edge. In this region, the photon is completely absorbed, creating an excited photoelectron and leaving a core hole in the atom. The absolute position of the edge can be used to determine the oxidation state of the core atom. For example, higher energies will be required to expel an inner shell electron from a more positively charged ion. The XANES region also contains information on vacant orbitals, electronic configuration, and site symmetry, as the photoelectron transitions to unfilled bound states, nearly-bound states, or continuum states of the appropriate energy [4].

Beyond the XANES region, sufficient energy is supplied that transitions are always to continuum states. In this region, the resulting photoelectron backscatters off of the nearest neighbors, affecting the x-ray absorption and creating oscillations in the spectra above the absorption edge. These oscillations can be used to determine atomic number, distance, and coordination number of nearest neighbors. These oscillations appear as a superposition of the sine waves created by the interaction between the core atom and each shell. EXAFS does not occur for isolated atoms but only appears when atoms are in a condensed state [5].

1.3.2.2 XAS data analysis

XAS data analysis software utilizes the EXAFS equation to fit experimental data by varying the parameters N_i (coordination number), R_i (bond length), and σ_i^2 (disorder). The identity of the ith shell atom is accounted for along with the absorber identity and the absorption edge in the phase and amplitude functions. The program FEFF [6] is utilized by most fitting programs, including EXAFSPAK [7] and GIFeffit [8], to calculate the phase and amplitude function for each possible path, including multiple scattering paths. FEFF paths are typically calculated using the closest possible structure in order to get the most accurate results. Structure inputs for FEFF can be created using ATOMS [9].

1.4 Synthesis and characterization of zirconia-thoria-urania fuels

Thoria-urania ceramics were produced with varying amounts of zirconia added to stabilize the fuel. The structure of the ceramics was analyzed using XAFS and compared to results obtained from complementary x-ray based techniques including XRD, EELS, and EDX [10]. The effect of the zirconia stabilization was then assessed by dissolving the ceramics in low ionic strength solutions over a range of pH under both argon and a mixture of argon and 10% CO_2. The best candidates for use as fuels were then dissolved under air in a high gamma radiation field to evaluate the effects of radiation on solubility of the actinides that are the backbone of the fuel matrix.

The analysis of the binary systems reveals mutual affinities between the various species. As expected from previous studies, U and Th show perfect solubility. When UO_2 and ZrO_2 are sintered together, a metastable Zr-based tetragonal phase is formed, revealing solubility of U in Zr, contrary to the case of Th and Zr where two thermodynamically stable phases form. The phase structure of the ternary ZrO_2-ThO_2-UO_2 systems is clearly established. Regardless of the Zr content, a ThO_2-UO_2

solid solution with a fluorite structure separate from a ZrO_2 based phase forms. The ZrO_2 phase contains UO_2 and MgO.

Thorium XANES showed very similar structure to the pure ThO_2 standard. The Zr K edge revealed some fine structure in the pre-edge. The U L_3 edge peaks appear to shift to the right with higher zirconia content. The spectra lack the characteristic oxide shoulder seen in the UO_2 standard as well as the sharp peak of the uranyl standard, indicating that the structure is mixed in oxidation state (Figure 1.1). In addition, while the spectra more closely resemble the UO_2 standard, the main absorption peaks are shifted 1-2 eV higher, and the shift increases with Zr content.

The Fourier transforms of the Th EXAFS data confirm the structural similarities to ThO_2. Uranium and Th are completely interchangeable in the Th oxide lattice. Analysis of the U Fourier transforms showed that all samples exhibited contracted U-O bond lengths when compared to the UO_2 reference (Figure 1.2). Contraction increased with increasing Zr content, verifying the increasing oxidation of U with Zr content observed by EELS and XANES. Analysis of the Zr spectra for each sample showed that the average Zr-M bond length decreased with increasing Zr content. The addition of 0.5 wt% MgO decreased the average Zr-M bond length for the $ZrTh_3U$ sample, but had no noticeable effect on the higher Zr content samples. This shortened average bond length appeared to effect the amount of U in the zirconia lattice.

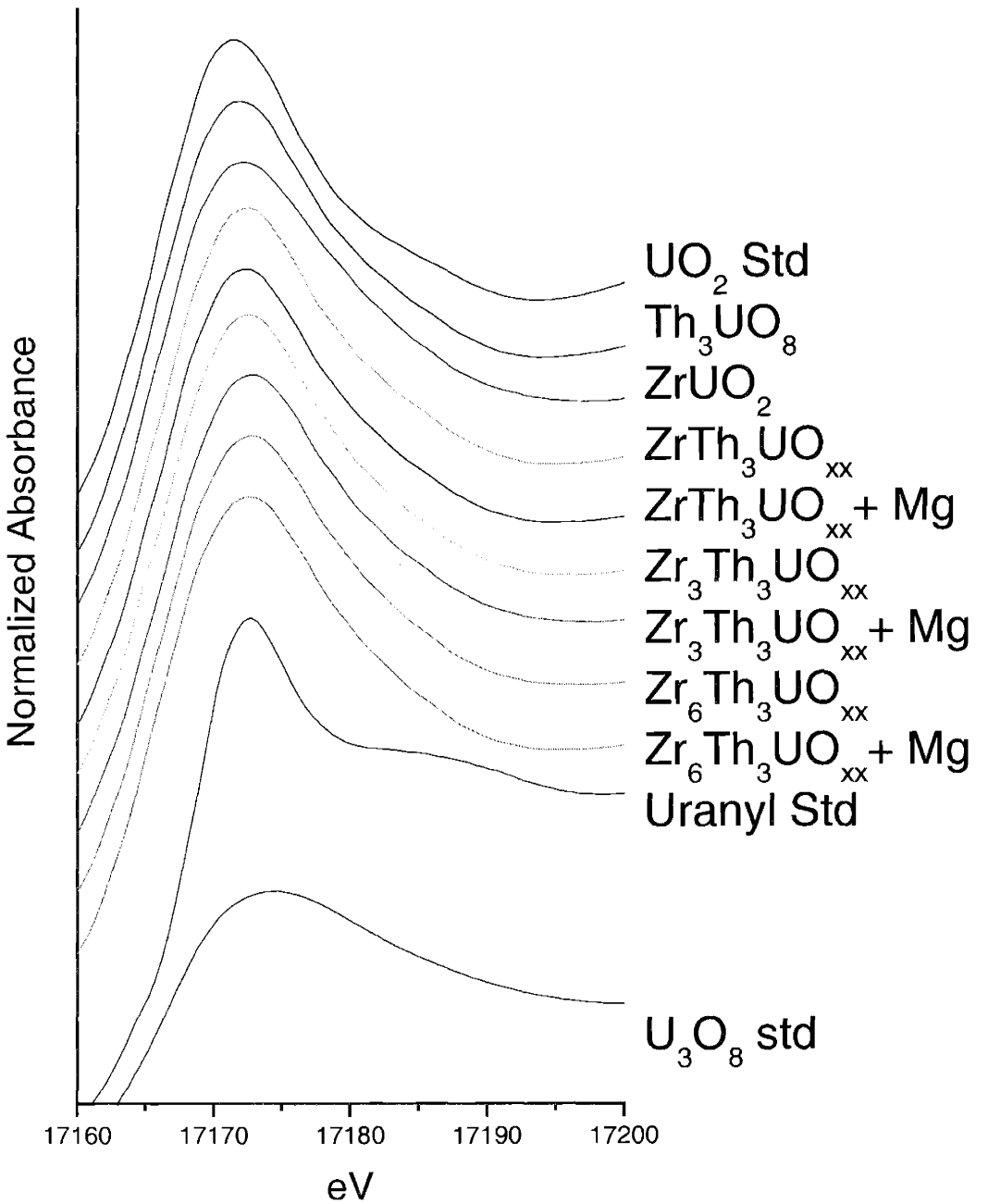

Figure 1.1. Uranium L_3 XANES spectra for the uranium standards and samples.

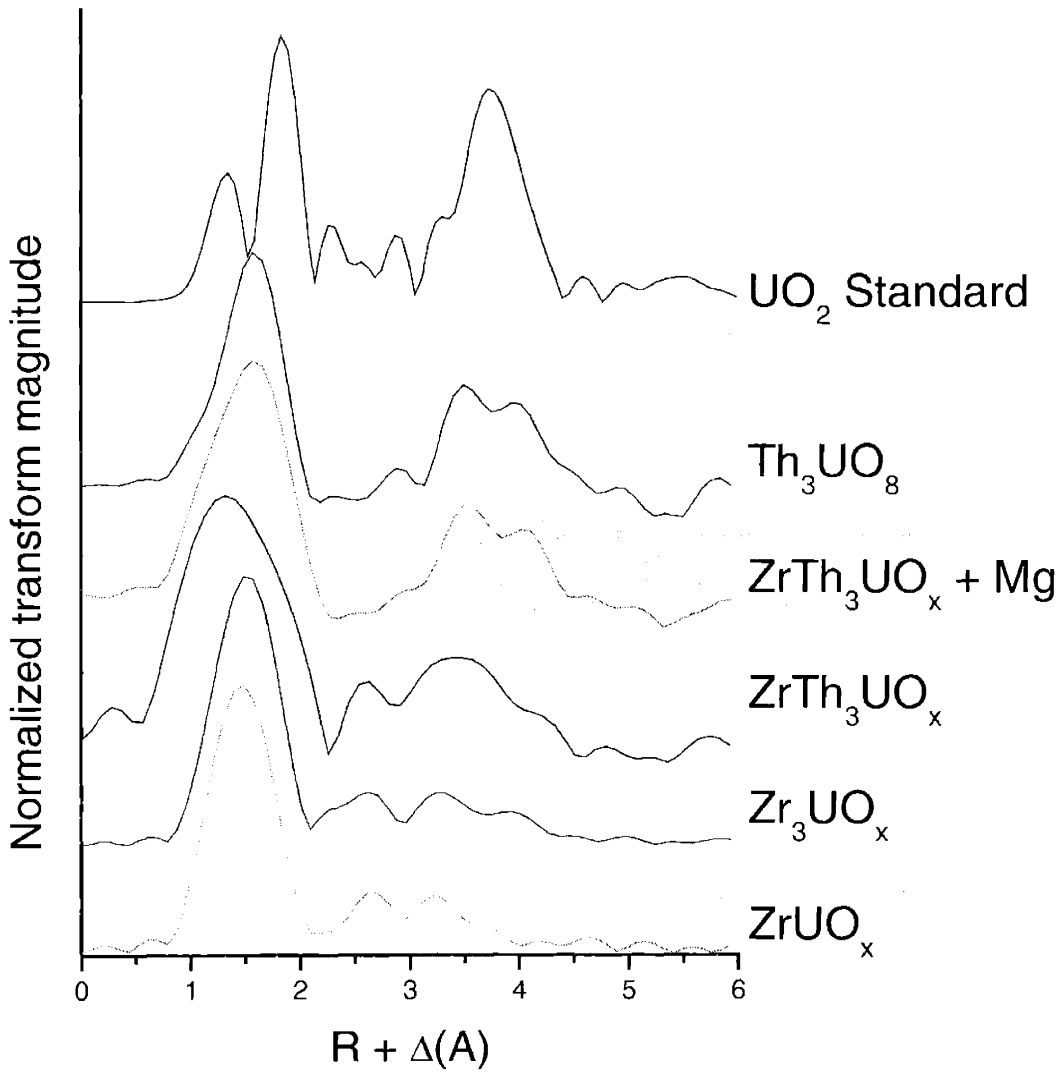

Figure 1.2. Uranium EXAFS Fourier transforms

Dissolution experiments were conducted on the ceramics in 0.1 M $NaClO_4$ under 100% argon or 90% argon/10% CO_2 at 25 °C. Kinetics analyses were performed in order to determine dissolution rate constants, surface area mass normalized dissolution, and solution equilibrium conditions. The influence of carbonate is minimal under the conditions examined. Not surprisingly, pH is the largest influence on the dissolution of Th. In the experimental range examined there is little recognizable difference between Ar and 10% CO_2 atmosphere. This data indicates the ceramics will be more stable at lower pH. . The solubility product

constants calculated from the equilibrium concentrations for the two ceramics were equivalent, with $K_{spTh3UO8}$= -48.3±0.4 and $K_{spZrTh3UO8}$= -47.9±0.9. The data was used to calculate the Th solution phase concentration. This indicates the Th in the ceramic is well behaved and existing literature data can be useful in describing the behavior of Th in the system.

The result was compared to the dissolution of UO_2 from pH 5-9 in 0.1 M $NaClO_4$ under a 1% CO_2 atmosphere at 25 °C. It was found that the U from the UO_2 had a higher solution phase concentration than Th at high pH and was highly dependent upon the solution Eh of the evaluated conditions (Figure 1.3).

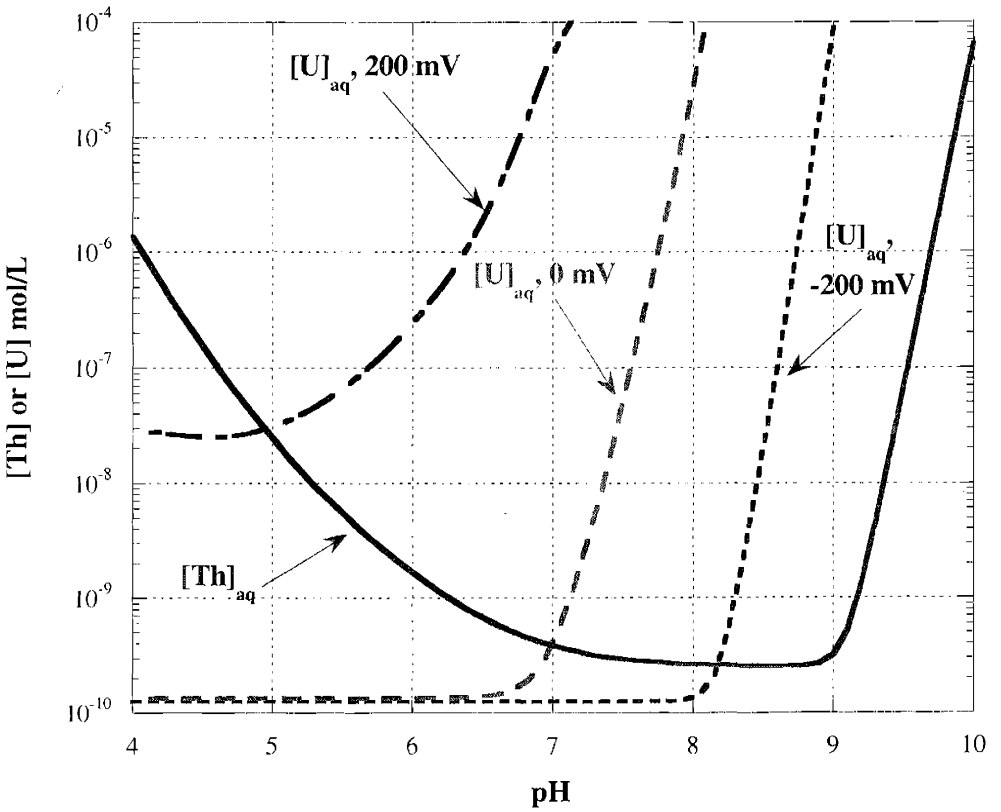

Figure 1.3. Calculated Th and U equilibrium solution concentration from $ZrTh_3UO_{10}$ and UO_2

The effect of gamma radiation on the dissolution of Th_3UO_8 was studied using the MIT research reactor spent fuel pool gamma source to simulate the radiation environment in a repository. Th_3UO_8 powders and pellets fabricated via a

precipitation process were immersed in purified water solutions adjusted to pH 4, 7, and 10 and exposed to a dose rate of 300 Gy/hr. Results showed strong pH dependence for the thorium samples, with a maximum concentration of 10^{-6} M at pH 10, two orders of magnitude higher than the controls (Figure 1.4). Irradiated uranium concentrations were consistent at 10^{-6} M, indicating no pH dependence. This can be attributed to oxidation from U(IV) to U(VI) by radiolysis products produced in the γ-field [10,11]. The largest increase over the control was a factor of 10 at pH 7. As total dose accumulated in all samples, the actinide concentration reached a peak and then began to decrease, indicating a possible precipitation reaction. It is hypothesized that the increased thorium solubility is caused by the formation of hydroxide or carbonate colloids, explaining the pH dependence of the reaction.

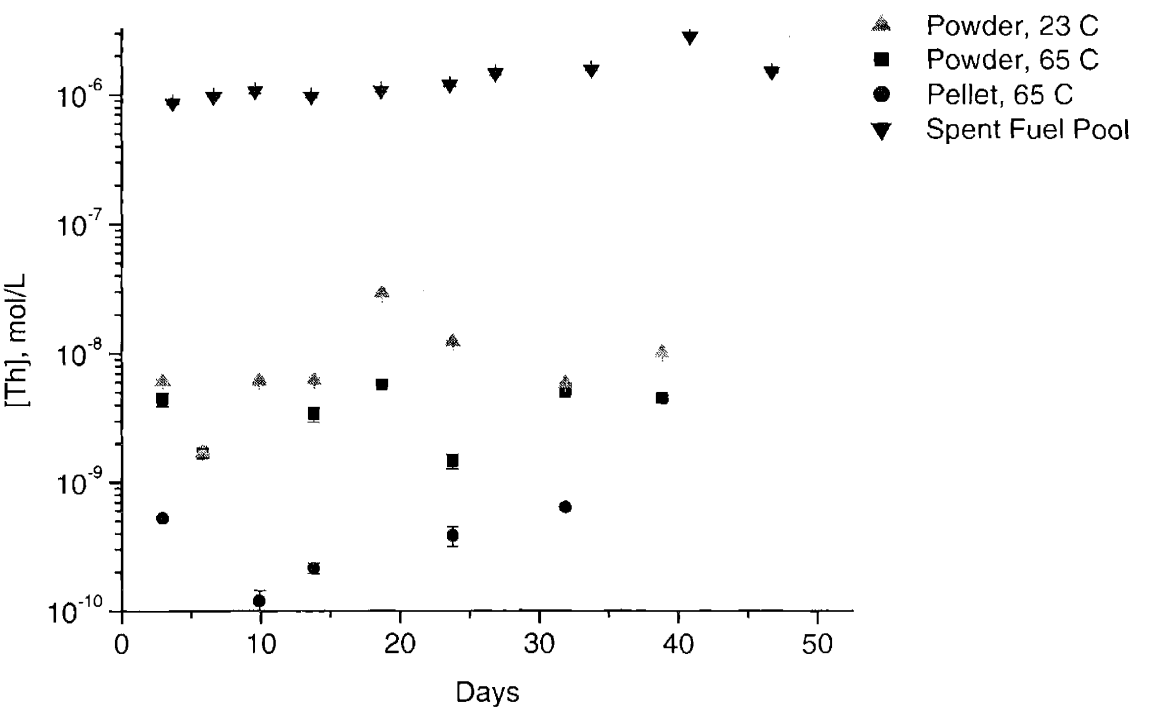

Figure 1.4. Solubility of thorium at pH 10

1.5 Characterization of UC and UC/US fuels

Uranium carbide (UC) and uranium sulfide (US) are of interest as potential replacements for UO_2 fuels in Generation IV nuclear reactors, specifically the Gas Cooled Fast Reactor (GCFR) project. Oxidation of UC under CO_2 is of concern at temperatures above 500 °C [12], and current GCFR design calls for 300 MW_e gas turbines that operate at 45% thermal efficiency at 550 °C [13]. Mixed UC-US fuels have been shown to decrease oxidation effects under air [14]. The structure of uranium in UC and mixed UC/US solid solutions fabricated for study of oxidation effects under CO_2 were analyzed using X-ray absorption spectroscopy (XAS). UC samples were fabricated by carbothermic reduction of UO_2. UC/US samples of varying ratios were fabricated with a two-step process utilizing zinc sulfide.

Sample	Phase	Bond	N	R(Å)	σ^2
UC-7	UC	U-U	7.5	3.50	0.00368
		U-C	19	4.26	0.00977
		U-U	5.8	6.06	0.00238
	UO_2	U-O	7.8	2.47	0.01202
		U-U	4.0	4.79	0.00355
UC-8	UC	U-U	8.1	3.51	0.00427
		U-C	29.8	4.24	0.01659
		U-U	5.6	6.06	0.00303
	UO_2	U-O	5.4	2.37	0.01679
		U-U	2.9	4.80	0.00297
UC-9	UC	U-U	6.4	3.51	0.00523
		U-C	22.6	4.26	0.00451
		U-U	3.6	6.07	0.00200
	UO_2	U-O	11	2.47	0.02418
		U-U	3.5	4.78	0.00664

Table 1.1 Structure of UC samples from XAS data fits

Results revealed imperfections in the fabrication processes as significant concentrations of UO_2 were present in all samples. Uranium was found to be in the tetravalent state in all samples. Structures of all samples are presented in Tables 1.1 and 1.2. Differences in structure between UC samples were found, indicating a need to refine the synthesis procedure. UC/US ratios followed the expected trend but were not as predicted. The amount of UO_2 contamination increased with increasing UC content, indicating the UC fabrication process as the likely source.

Sample	Phase	Bond	N	R(Å)	σ^2
25% UC	US	U-S	5.3	2.73	0.00789
		U-U	1.4	3.88	0.00196
	UO_2	U-O	0.6	2.29	0.00193
		U-U	1.2	4.99	0.00300
50% UC	US	U-S	3.0	2.71	0.00622
		U-U	3.4	3.83	0.01096
		U-S	4.8	4.59	0.01401
	UC	U-U	2.8	3.52	0.01463
	UO_2	U-O	2.1	2.32	0.01096
75% UC	US	U-S	1.7	2.73	0.00712
		U-U	3.0	3.88	0.01031
	UC	U-U	3.8	3.50	0.0035
	UO_2	U-O	3.8	2.38	0.01996
		U-U	1.3	4.80	0.00188

Table 1.2 Structure of UC/US samples from XAS data fits

1.6 Application of XAS to Nuclear Chemical Engineering

The speciation of actinides in two distinct materials that can affect the impact of radionuclides in the environment was determined using x-ray absorption spectroscopy. The first set of materials evaluated were actinide-imprinted resins synthesized by a polymerization technique. The resins are designed to selectivity for separation of specific actinides. The structure of thorium, uranyl, and samarium imprinted resins was examined. Samarium was used as a homolog for americium and curium. Resins were evaluated for both structure and reusability. Results showed the resin structures were as expected (Figure 1.5). In addition, structures did not change following actinide removal and resorption, indicating that the resins are reusable to some extent.

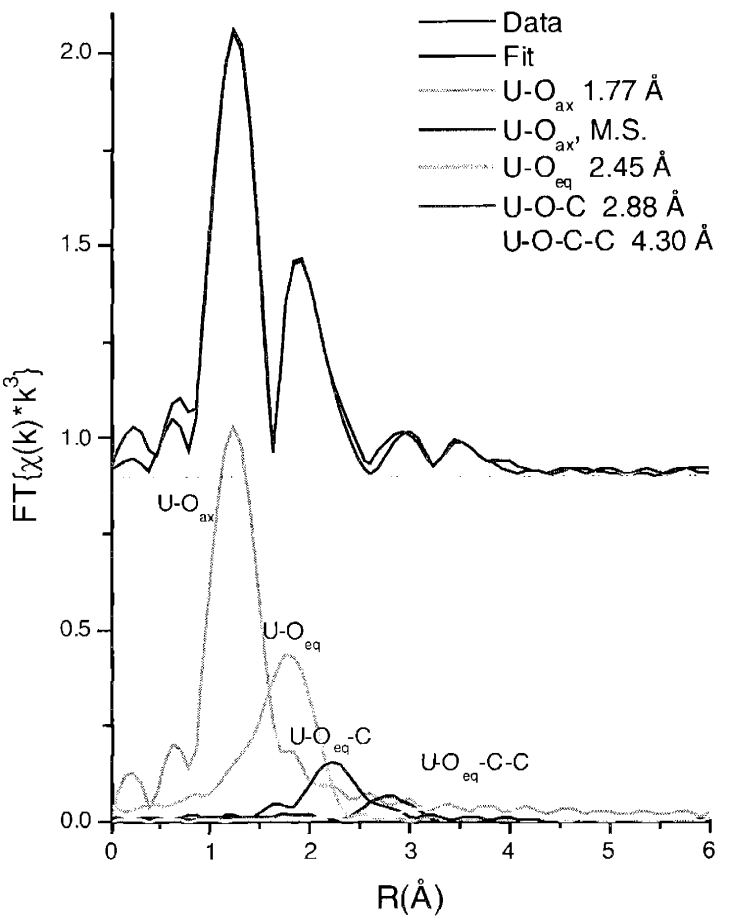

Figure 1.5. Deconvolution of the Uranium-templated non-released sample fit.

The method of uranium sorption to the metal reducing bacteria *Shewanella oneidensis* was also examined. By reducing uranium in the environment from the highly soluble species U(VI) to the rather insoluble U(IV), *S. oneidensis* and similar bacteria could significantly hinder the migration of uranium in the biosphere. Results showed that the uranium was attached to a phosphate group (Figure 1.6). Further studies are needed to determine if the interaction is external to the cell or via phosphate groups attached through the cell wall.

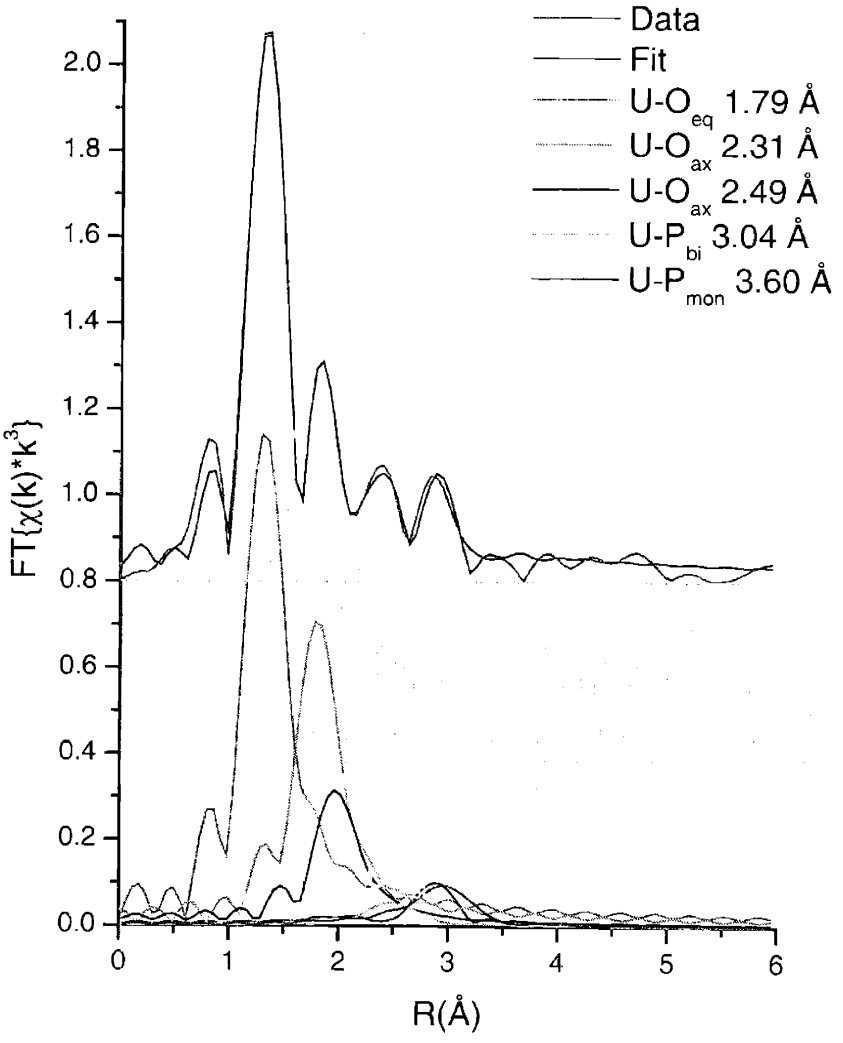

Figure 1.6. Deconvolution of 4 mM fit.

1.7 Characterization of Uranium Speciation in a Heterogeneous Metallic Matrix

Three metallic slag samples recovered from the site of their inadvertent creation several decades after the fact were sectioned and analyzed to determine uranium speciation to evaluate environmental behavior as well as assess proliferation resistance of the waste form. Uranium concentration in the highly inhomogeneous samples was up to 5% by weight as determined by gamma spectroscopy. Sample sections were milled in a hardened steel ball mill for x-ray absorption spectroscopy analysis (XAS). Powders were digested in a mixture of heated concentrated nitric acid and peroxide and analyzed for elemental content using ICP-AES and ICP-MS.

Though elemental content of the samples varied widely, high concentrations of Al were consistently found. Other metals of significance were Ti, Fe, Ni, Cu, Zn, and Sn. High Pb concentrations were occasionally found. XAS analysis revealed the two main phases present. Surface samples were a mixture of uranyl and a metallic uranium compound (Figure 1.7). The interior samples contained primarily the metallic uranium compounds, though in some cases small amounts of uranyl were also present. The metallic uranium compounds were identified as U-Al and U-Ti. The uranyl present on the surface is highly mobile, indicating low stability of the slags in the environment. In addition, the samples showed little proliferation resistance and could be dissolved with relative ease using commonly available chemicals.

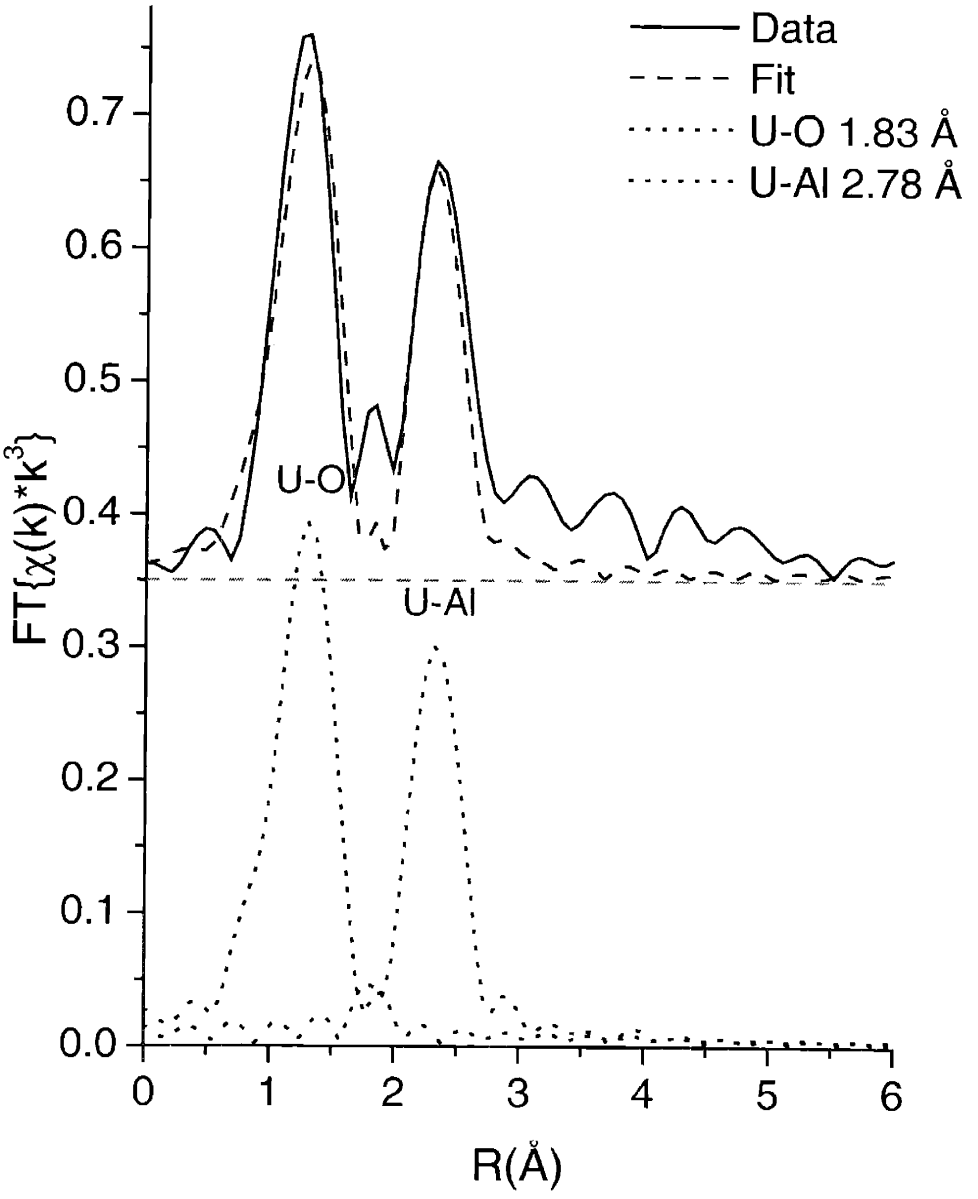

Figure 1.7. Deconvolution of the EXAFS fit for Sample 1. The U-O bond length of 1.8 Å is characteristic for the uranyl structure. The relatively short U-Al bond distance indicates a metallic structure.

1.8 Conclusions

Actinide speciation can be integrated into remediation efforts through analysis of speciation in the source term and determination of solubility and solution phase concentration. Incorporating speciation can mitigate the well-known limitations inherent to K_ds in describing environmental behavior and provide a direct determination of the chemical forms of the mobile actinides.

Inclusion of speciation will prove critical with the use of advance remediation techniques such as bioremediation or active barriers. These techniques rely heavily on interaction with a distinct chemical form of the actinide or operate only on a specific oxidation state. The kinetics and final chemical forms will be dominated by the actinide speciation. The described speciation method will enhance the efficacy of these techniques through the enhanced understanding of the important chemical forms and their dynamics under given conditions.

There is obviously a pressing need to formally incorporate speciation into actinide remediation. The use of modeling and laboratory studies provide a strong basis for a reliable analysis of actinide chemical forms present in a contaminated site. When applicable, inclusion of advanced techniques, such XAFS, should be applied to actinide remediation projects. This would provide support of the inclusion of species and help confirm the initial modeling and experimental results. Combining and utilizing all existing efforts would provide the greatest benefit to actinide remediation.

1.9 References

1. Runde, Wolfgang et al. Geochemical speciation of actinides in soil and solution, *Geochemistry of Soil Radionuclides,* Soil Science Society of America Special Publication no. 59. 2002 (45-59)
2. Silva, R.J. and Nitsche, H. Actinide environmental chemistry, *Radiochimica Acta* 1995 70/71 (377-396)
3. Kim, J.I. Transuranic elements in natural aquatic systems, **Handbook on the Physics and Chemistry of the Actinides**, 1986 Elsevier Science (413-455) 2.
4. Bunker, Grant, **Elements of XAFS**, Physics Department, Illinois Institute of Technology, Chicago, IL
5. Konningsberger, D.C. and R. Prins, **X-Ray Absorption: Principles, Applications, Techniques of EXAFS, SEXAFS, and XANES**, John Wiley & Sons, USA 1988
6. Rehr, J.J. et al, FEFF. University of Washington Department of Physics http://leonardo.phys.washington.edu/feff/
7. George, G.N. EXAFSPAK. http://www-ssrl.slac.stanford.edu/exafspak.html
8. Newville, Matt. IFEFFITT. http://cars9.uchicago.edu/ifeffit/
9. http://feff.phys.washington.edu/~ravel/software/atoms/Welcome.html
10. Ermatov, S.E. et al, Phase changes of uranium oxides under irradiation, *Prokhozhdenie Elem. Chastits Veshchestvo,* 1983 (78-83)
11. Gromov, V. Dissolution of uranium oxides in the γ-irradiation field, *Radiation Physics and Chemistry,* 1981. 18(1-2) (135-46)
12. Murbach, E.W., Turner, W.D., Oxidation of Uranium Carbide by Carbon Dioxide, *NASA Doc.* N63-11826, 1962.
13. Dostal, Vaclav; Driscoll, Michael J.; Hejzlar, Pavel; Todreas, Neil E., Supercritical CO2 gas turbine power cycle for next-generation nuclear reactors. *ICONE 10, Proceedings of the International Conference on Nuclear Engineering, 10th,* Arlington, VA, United States, Apr. 14-18, 2002, 2 (567-574)
14. Lovell, G.H.B., Van Tets, A., Britz, E.J., Preparation of some US-rich solid solutions in the UC-US system, *Journal of Nuclear Materials,* 1974, 51 (337-342)

2 Introduction

Current methods for evaluating the fate and transport of actinides in the environment are inadequate. The majority of environmental transport codes, including those used in the site suitability assessment for the Yucca Mountain Project, rely on a distribution coefficient, K_d. It is an attempt to describe the speciation of a contaminant with respect to solubility at a specific site without requiring any specific knowledge of the chemistry, geology, or biology of the local environment. The soluble fraction is usually considered to have the most impact on remediation of a site, since this is typically both the most mobile and the most toxic form of a contaminant. The distribution coefficient is determined by taking the ratio of the contaminant present in the solid phase of a sample to the contaminant present in the solution phase.

Typical methods for determining K_d consist of removing samples of sediment and local waters from the vicinity of the contaminated site. The number of samples is usually quite low and represents a small fraction of the actual contaminated area. The solid and solution phases of the samples are separated, and then individually exposed to the contaminant for a limited amount of time. The amount of contaminant present in each phase is then measured. Frequently the experimental contaminant source term is not related to the actual source term except for the presence of the element of interest. There is also usually no attempt to verify that equilibrium has been achieved.

Measurements of the K_d parameter are highly variable and unpredictable due to differences in soil composition from the various phases present and changes in aqueous conditions through a site. These variations can be large over affected areas, as pH, ionic strength, and the available concentrations of the polluting actinide and other solids present in the aqueous phase can change, as well as the phase composition of the local soil and sedimentation. Subsequent measurements of a

system therefore can differ greatly from initial results. In addition, K_d measurements cannot take into account evolution of the contaminated site over time. Distribution coefficients will change as the seasons change, and will also be affected by longer term changes in climate patterns such as droughts. There will also be changes on shorter time scales as, for example, the K_d measured from samples taken after a few days of rain can vary greatly from that taken during drier weather.

Complementing solution chemistry knowledge with the actual chemical speciation of the source term provides unique information for each system and therefore a much more accurate assessment of the environmental impact and provides cues as to the most expedient methods to reduce the risk to the environment and the local population. X-ray absorption fine structure spectroscopy (XAFS) provides an extremely useful tool for determining the speciation of an element in a diverse array of materials at low compositions.

2.1 Project overview

2.1.1 Problem description

It is widely recognized that the behavior of actinides in the environment is dictated by their speciation, or chemical form [1-5]. It is therefore imperative to have a clear understanding of a waste form or environmental contaminant in order to effectively assess and treat the affected area. Current methodology utilizes the distribution coefficient (K_d), a rough measure of contaminant mobility in environmental systems, however neither the empirical nor theoretical determination of K_d is well defined. Although we understand the limitation of the K_d parameter, the reality is that the K_d is often the only parameter used in environmental fate and transport models to account for the mobile fraction of contaminate in predicting total risk. A fresh approach to the problem incorporating speciation that can be applied to

a wide range of conditions is required. This can be achieved by combining analysis by X-ray absorption spectroscopy (XAS), a non-destructive technique that utilizes the interaction of x-rays to determine the structure of a material with respect to an element to determine the speciation of the actinide in the source term with, experimental and computational analysis of the environmental and geochemistry of the affected site to greatly enhance the ability to accurately assess actinide fate and transport.

2.1.2 Research goals and objectives

In order to show that combining knowledge of the actinide speciation in the source material with knowledge of the environmental and geochemistry of the affected site using x-ray absorption spectroscopy is a useful technique that can be universally applied, a wide range of actinide-bearing solids was analyzed. The first objective was to apply the methodology to a simulated nuclear fuel and use it to assess its suitability for repository disposal. Because it has not received much attention in this respect, a thoria based fuel was used for this analysis. In addition, the uranium carbide-sulfide system was also analyzed.

The second objective was to show that this methodology could be widely applied. Two diverse actinide bearing materials were used to show this – actinide templated resins designed to increase selectivity for individual actinide ions during separations, and uranium reducing bacteria. The final objective was to apply the methodology to a real world environmental remediation project.

2.1.3 *Research task list*

In order to achieve the goals described in the previous section, a series of tasks were undertaken. A description of each task is listed below. Tasks 1 and 2 consider speciation of actinides in nuclear reactor fuels. The fuel in Task 1 is fully analyzed using the methodology developed in this thesis from structure of the fuel to subsequent effects of the radiation environment in the repository on fuel dissolution. Task 3 analyzes the speciation of actinides in materials that affect their environmental impact. Task 4 is a culmination of the work that assesses the speciation and impact of an actual actinide source term that existed in the environment for some time before analysis.

Task 1- Characterization and solubility studies of the mixed zirconia-urania-thoria ceramic system to compare the stability of the ThO_2 matrix as a waste form with the standard UO_2 matrix found in most modern spent nuclear fuel. This task includes several subtasks:

1a. Characterize the material properties of mixed thoria-urania ceramic fuels stabilized for long-term repository disposal by incorporating varying amounts of zirconia using XAFS. Compare this data to previous results using complementary x-ray techniques including x-ray diffraction (XRD), electron energy loss spectroscopy (EELS) and energy dispersive x-ray analysis (EDX).

1b. Determine the actual effect of zirconia stabilization on the solubility of the ceramics. Compare these data with kinetics and

solubility product constants from both zirconia-free thoria urania ceramics and the pure thoria and urania species.

1c. Assess the impact of the high radiation field expected in the repository environment on the most promising ceramics from Task 1b by performing dissolution experiments in a high β-radiation environment.

Task 2 - Determine the structure of UC and mixed UC/US fuels using XAFS. In addition, examine oxidation effects on these fuels also utilizing XAFS.

Task 3 - Evaluate the speciation of two distinct materials that can affect the impact of actinides in the environment. This is divided into two subtasks, one for each material.

3a. Determine the structure of actinide imprinted resins created to separate specific actinides from waste materials. Assess the reusability of the resins through any changes in structure after release and resorption.

3b. Determine the method of uranium sorption to the metal reducing bacteria *Shewanella oneidensis*. By reducing uranium in the environment from the highly soluble species U(VI) to the rather insoluble U(IV), *S. oneidensis* and similar bacteria could significantly hinder the migration of uranium in the biosphere.

Task 4 - Determine the speciation of uranium in metallic slag samples that had been exposed in the environment for several decades following their accidental formation. Assess the environmental impact and the proliferation resistance of the slag.

2.2 Thesis overview

This thesis is presented in ten sections. The first chapter is a summary of the important points of the thesis. The second chapter introduces the thesis, while the background is split into chapters on actinide speciation and x-ray absorption spectroscopy, the main technique utilized in the thesis. The body of the thesis is divided into chapters based on the specific application of the technique, as follows:

Chapter 6 – Synthesis and characterization of zirconia-thoria-urania fuels

Chapter 7 – Characterization of UC and UC/US fuels

Chapter 8 – Application to Nuclear Chemical Engineering

Chapter 9 – Characterization of Uranium Speciation in a Heterogeneous Metallic Matrix

The conclusion, Chapter 10, discusses application of this methodology to improving understanding of speciation in environmental remediation, and the use of speciation modeling to complement experimental results.

2.3 References

1. Runde, Wolfgang et al. Geochemical speciation of actinides in soil and solution, *Geochemistry of Soil Radionuclides*, Soil Science Society of America Special Publication no. 59. 2002 (45-59)
2. Caceci, Marco S. Environmental chemistry of the actinide elements, *Metal Speciation in the Environment*, 1990 Springer-Verlag Berlin Heidelberg (571-591)
3. Silva, R.J. and Nitsche, H. Actinide environmental chemistry, *Radiochimica Acta* 1995 **70/71** (377-396)
4. Kim, J.I. Transuranic elements in natural aquatic systems, **Handbook on the Physics and Chemistry of the Actinides**, 1986 Elsevier Science (413-455)
5. Choppin, G. Solution chemistry of the actinides, *Radiochimica Acta*, 1983 **32** (43-53)

3 Environmental Chemistry of the Actinides

Since the advent of the Manhattan project, significant amounts of actinides and other radionuclides have been released into the environment unchecked through a combination of carelessness and ignorance of their long term impact. Sources of this extensive contamination throughout the geosphere are typically attributed to nuclear weapons tests and the nuclear weapons manufacturing infrastructure, though commercial nuclear accidents and manufacture and use of radioactive sources are also a major contributor. In addition, as the world moves toward deep geologic disposal of nuclear reactor waste, a large new potential source of radioactive contamination will be introduced in the form of spent nuclear fuel and other products of the nuclear fuel cycle. The actinides are of special concern because of their long half-lives, high toxicity, and complex physical and chemical properties [1]. Knowledge of the speciation of the actinides in the source term as well as interactions in the local environment is key to understanding and effectively remediation of actinide contaminated sites.

3.1 Actinide sources in the environment

The source, or original form of the actinide as it was introduced to the environment, will have a significant effect on the environmental behavior of the actinide. The rate of actinide release and environmental speciation are dictated initially by the source term.

The source term can be extremely complex, as in the mixed wastes in the tanks at the Hanford site [2] which contain an assortment of actinides and fission products in a variety of physical forms. Simpler source terms consisting of single species also exist, though these are not the norm. Typical source terms such as nuclear waste

glass and spent nuclear fuel seem simple in that the initial matrix is relatively constant, yet can become very complicated due to the sheer number of actinides present and the complexity of their individual chemistry.

Two main sources of potential and actual actinide contamination dominate due to their prevalence in total actinide inventory. The first is spent nuclear fuel, which though currently spread over 100 sites in the US alone, will be concentrated in the near future in geologic repositories. The US site currently located at Yucca Mountain, NV is alone expected to hold 70,000 metric tons of heavy metal [3]. The other important source of current and potential future actinide contamination in the US is the nuclear weapons complex, currently operated by the Department of Energy. Widespread radioactive contamination of soil and groundwater from past waste disposal, accidental releases and nuclear weapons testing, and aging interim storage facilities have resulted in potentially serious problems for the environment and human health [4].

3.1.1 Spent nuclear fuel

Typical commercial spent nuclear fuel consists of a variety of actinides and fission products in a UO_2 matrix. The important actinides present and their half lives are given in Table 3.1. Many fission products, including several with half-lives on the order of the actinides, are also present. In general, the actinides are considered to be more important for the long term storage of nuclear waste due to their long half-lives, their radiological toxicity due to the damaging effects of alpha radiation, and their affinity for bone tissue and long residence time in living organisms [5].

Isotope	Half life (y)
^{234}U	246000
^{235}U	$7.04x10^{8}$
^{238}U	$4.47x10^{9}$
^{237}Np	**$2.14x10^{6}$**
^{239}Pu	24100
^{240}Pu	6560
^{242}Pu	375000
^{244}Pu	$8.0x10^{7}$
^{241}Am	**432.7**

Table 3.1 Isotopes and half lives of long-lived actinides in spent nuclear fuel. Isotopes of special interest for geologic disposal are in bold.

3.1.2 Nuclear weapons complex

Through a combination of weapons testing, accidental release, insufficient containment, and poor disposal methods, a significant quantity of actinides was released into the environment by the nuclear weapons complex over the past six decades. Source terms can be extremely dispersed in low level, such as the fallout from atmospheric nuclear tests, localized low levels, such as plumes escaping from deteriorating tanks and containers, or even highly localized high activity accidental releases.

3.2 Solution chemistry

The main transport mechanism for actinides in the environment is water, therefore fate and transport depends largely on solution chemistry. Although actinide solubility tends to be lowest at the neutral pH of natural waters, a number of possible interactions can affect this. The most important interactions of actinides in the environment are complexation, precipitation, sorption, and colloid formation [6]. All of these processes are heavily influenced by the oxidation state of the actinide. The oxidation state will, in turn, be dictated by the environmental conditions, including pH and Eh of the natural waters and in some cases the ligands available for complexation. Because the stability of oxidation states in natural waters varies from actinide to actinide, the fate and transport of each actinide in a system will in turn differ.

3.2.1 Oxidation state

The unique chemistry of the actinides leads to a large array of possible oxidation states for many in the series, ranging from +2 to +7. Table 3.3 gives the common oxidation states of actinides that can be found in significant quantities in the environment. Actinides do not exist as free ions in the +5 or +6 states, instead they form unique stable actinyl species AnO_2^+ and AnO_2^{2+} which act as a unit in chemical reactions. The actinyl species have a symmetric and nearly linear structure, resulting in higher effective charges [6]. For PuO_2^+ and PuO_2^{2+} charges of approximately +2.3 and +3.3, respectively, have been reported [7].

Actinide	Oxidation state(s)
Th	**+4**
U	+3, **+4, +5, +6**
Np	**+3, +4, +5, +6**
Pu	**+3, +4, +5, +6**
Am	**+3**, +4, +5, +6

Table 3.2 Actinide oxidation states. Expected stable oxidation states in the environment are in bold.

3.2.2 Precipitation

Precipitation occurs when actinide concentrations exceed their solubility limit. Precipitation is limits migration by removing actinides from solution. The trend for actinide solubility in the environment by oxidation state is

$$+5 > +6 > +3 >> +4$$

The tetravalent state is generally orders of magnitude less soluble than the other states.

3.2.3 Complexation

Naturally occurring inorganic and organic ligands found in ground waters can interact with actinides creating complexes. Complexation effectively enhances the solubility of the actinide by increasing the amount of actinide in solution, and therefore tends to increase release and migration rates. Common inorganic ligands

available in natural waters include in decreasing order of complexation are OH^-, CO_3^{2-}, SO_4^{2-}, PO_4^{3-}, and Cl^-. Complexation with the carbonate and hydroxyl ligands are the most important chemical reactions in environmental systems due to their ubiquitous presence in ground waters and strong complexation with actinide cations. Organic ligands including humic and fulvic acids are also found in natural systems. A result of the decay of natural organic matter, humic and fulvic acids can vary greatly in size and complexation ability, causing interactions to be much more difficult to describe than inorganic complexation.

The trend in strength of complexation of actinides to the various ligands with respect to oxidation sate is

$$+4 > +3 \approx +6 > +5$$

Since actinide cations in the +3 and +6 oxidation states have similar effective charges, complexation characteristics are also similar [7]. A range of potential coordination numbers have been shown for actinides complexes. Simple cations (i.e. Th(IV)) have been observed with coordination numbers from 6 to 12. For the oxygenated cations (UO_2^{2+} for example), coordination of 2 to 8 is seen [8].

Total solubility of an actinide in a system can be described as the sum of the concentration of the free species and the concentrations of species created by complexing with available ligands. The following example demonstrates this using Th(IV) in a system containing free carbonate and hydroxyl ligands. The thorium aqueous phase will therefore consist of three parts: the free thorium (Th^{4+}), thorium hydroxide species, and thorium carbonate species, as expressed by

$$[\mathrm{Th}]_{aq} = [\mathrm{Th}^{4+}] + \sum_{x=1}^{4} [\mathrm{Th(OH)}_x^{4-x}] + \sum_{y=1}^{4} [\mathrm{Th(CO}_3)_y^{4-2y}] \qquad \text{Equation 3.1}$$

In order to determine the concentration of species in a particular environment, solubility and stability constants are needed. The formation of the free species can be described by

$$ThO_2 + 2H_2O \Leftrightarrow Th^{4+} + 4OH^- \qquad \text{Equation 3.2}$$

and the solubility product constant, K_{sp}, is given by

$$K_{sp} = [Th^{4+}][OH^-]^4 \qquad \text{Equation 3.3}$$

For the hydroxide and carbonate species, the formation is described by

$$Th^{4+} + aL^{-z} \Leftrightarrow ThL_a^{4-az} \qquad \text{Equation 3.4}$$

Where L is either OH^- or CO_3^{2-} (depending on the species), and the equation for the stability constant is

$$\beta_{ThL_a} = \frac{[ThL_a^{4-az}]}{[Th^{4+}][L^{-z}]^a} \qquad \text{Equation 3.5}$$

At any given pH, the concentration of the free species is determined by the solubility product constant, that of the hydroxide species is determined from the pH, and the

carbonate species concentration is determined from both the pH and the CO_2 partial pressure.

With this information, the stability constants can be calculated and the total thorium concentration under those conditions can be determined from Equation 3.6

$$[Th]_{aq} = [Th^{4+}] + \sum_{x=1}^{4} \beta_{Th(OH)_x} [Th^{4+}][OH^-]^x + \sum_{y=1}^{4} \beta_{Th(CO_3)_y} [Th^{4+}][CO_3^{2-}]^y$$

Figure 3.1 shows a calculation of the solubility of thorium over a range of pH (3 through 10) using $\log(k_{sp}) = 51$ [ref] in air. Higher solubility at low and high pH is expected, with a minimum in between. The pH range of Yucca Mountain (6.7 to 9.3) is expected to lie in the minima.

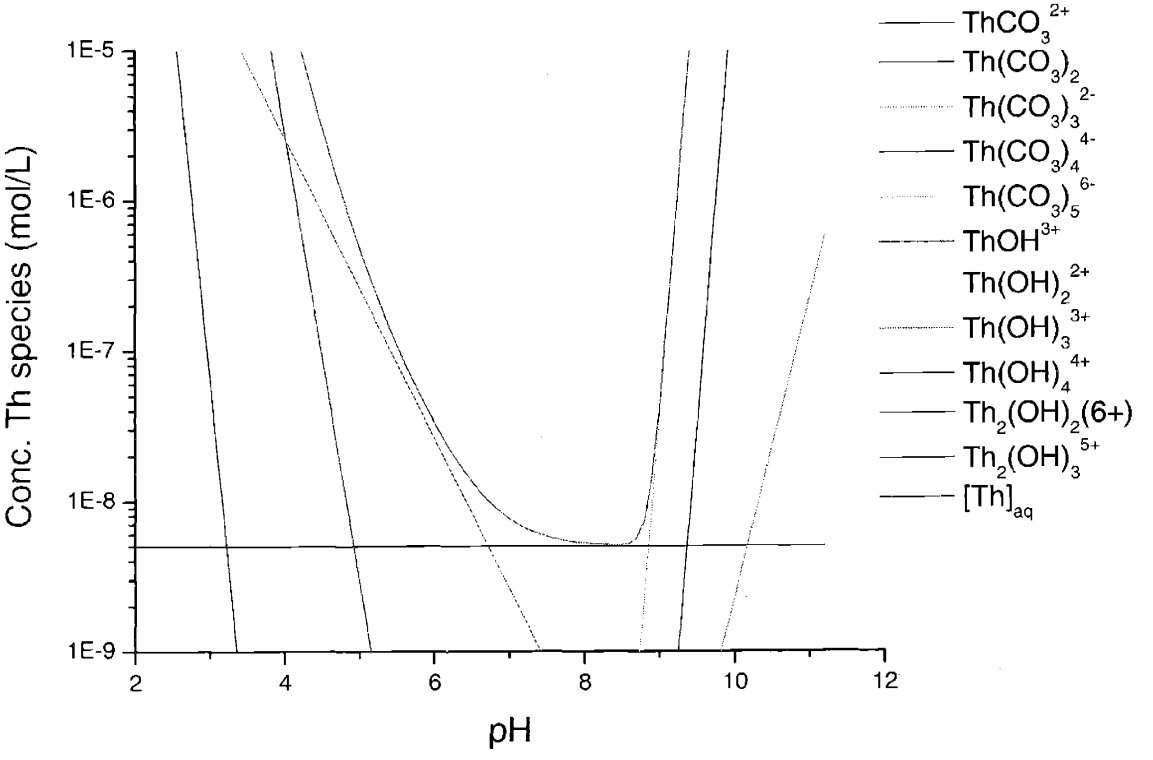

Figure 3.1: Thorium solubility

3.2.4 *Sorption*

Migration of free actinides in solution and actinide complexed ions can be retarded by sorption to minerals and solids available in the local environment. Sorption can be both reversible and irreversible. It can result from short range chemical forces (covalent bonding, etc.) which are frequently irreversible, or long-range forces (electrostatic, van der Waals) which are typically reversible [9].

3.2.5 *Colloid formation*

A complicating factor when assessing actinide migration in the environment is colloid formation. Colloids are small agglomerates of molecules that can range in size from less than 2 nm to over 200 nm. Depending on the nature of the colloid and the local environment, colloids can both enhance and retard actinide migration. Trivalent and tetravalent actinides have the greatest tendency to form colloids, followed by hexavalent and pentavalent ions [7].

3.2.6 *Biological interactions*

Actinide migration can be significantly impacted by interaction with microorganisms present throughout the environment. Interactions are both direct, such as oxidation and reduction reactions, biosorption, and bioaccumulation, or can be indirect, through changing the pH and redox potential of the system.

3.3 The distribution coefficient

Current analysis of actinide for remediation relies upon distribution coefficients (K_d) in evaluating mobility. The K_d is defined as the concentration of a contaminant in the solid S divided by the solution phase concentration C ($S=K_dC$) and is usually expressed in mL/g. This relationship is used in analysis models for estimating the actinide concentration in soil and solutions. The values for K_ds can vary greatly and are strongly dependent upon soil and solution chemistry even if consistent methods are used [10,11].

3.4 References

1. Runde, Wolfgang et al. Geochemical speciation of actinides in soil and solution, *Geochemistry of Soil Radionuclides*, Soil Science Society of America Special Publication no. 59. 2002 (45-59)
2. Babad, H. and Deichman, J.L. Hanford high-activity waste tank safety issues, Waste Management, Tucson, Arizona, Vol 1, 1991 (847-54)
3. Nuclear Waste Policy Act http://www.ocrwm.doe.gov/documents/nwpa/css/nwpa.
4. U.S. Department of Energy. *Accelerating cleanup: Paths to closure.* 1998 US-DOE Office of Environmental Management DOE-EM-0362
5. Caceci, Marco S. Environmental chemistry of the actinide elements, *Metal Speciation in the Environment*, 1990 Springer-Verlag Berlin Heidelberg (571-591)
6. Silva, R.J. and Nitsche, H. Actinide environmental chemistry, *Radiochimica Acta* 1995 **70/71** (377-396)
7. Kim, J.I. Transuranic elements in natural aquatic systems, **Handbook on the Physics and Chemistry of the Actinides**, 1986 Elsevier Science (413-455)
8. Choppin, G. Solution chemistry of the actinides, *Radiochimica Acta*, 1983 **32** (43-53)
9. Stumm, W and Morgan, J.J. **Aquatic Chemistry**, 2nd Edition. 1981 John Wiley and Sons, NY. (599-647)
10. Porro, I., Newman, M. E., Dunnivant, F. M.: Comparison of Batch and Column Methods for Determining Strontium Distribution Coefficients for Unsaturated Transport in Basalt. *Environmental Science and Technology*, 2000 **34(9)** (1679-1686)
11. Bethke, C. M. and Brady, P.V.: How the K_d approach undermines ground water cleanup. *Ground Water*, 2000 **38(3)** (435-443)

4 X-Ray Absorption Spectroscopy

X-ray absorption spectroscopy (XAS) is a technique that uses x-ray interactions to probe molecular structure of materials. XAS does not require long range order, so samples can be crystalline or amorphous, and can be in solid form, solution, or even gaseous. It is a highly specific technique that can individually probe the local structure surrounding each element in a sample. As such, it sees the global, average structure of the sample exposed to the x-ray beam with respect to a specific element.

4.1 Principles of X-Ray Absorption Spectroscopy

X-Ray Absorption Spectroscopy utilizes a tunable x-ray source to probe local structure of molecules, such as the identity, coordination number, and distance of atoms bonded to a core element of interest. Synchrotrons are typically chosen for the x-ray source due to their high energies and broad spectral ranges. A typical synchrotron setup is shown in Figure 4.1. Spectra obtained through XAS can be divided into two basic regions, X-ray Absorption Near Edge Structure (XANES) and Extended X-ray absorption Fine Structure (EXAFS).

To collect spectra, the appropriate energies are selected by diffraction from a double crystal monochromator. The incident beam (I_0) passes through an ion chamber which monitors the energy and then interacts with the sample. For samples of higher concentrations, the interaction of the beam with the sample is monitored via a second ion chamber in line with the first (Figure 4.2). Spectra from lower concentration samples are usually collected on a multi-element fluorescent detector array located perpendicular to the beam. In this case, the samples are placed 45 degrees off normal to facilitate data collection.

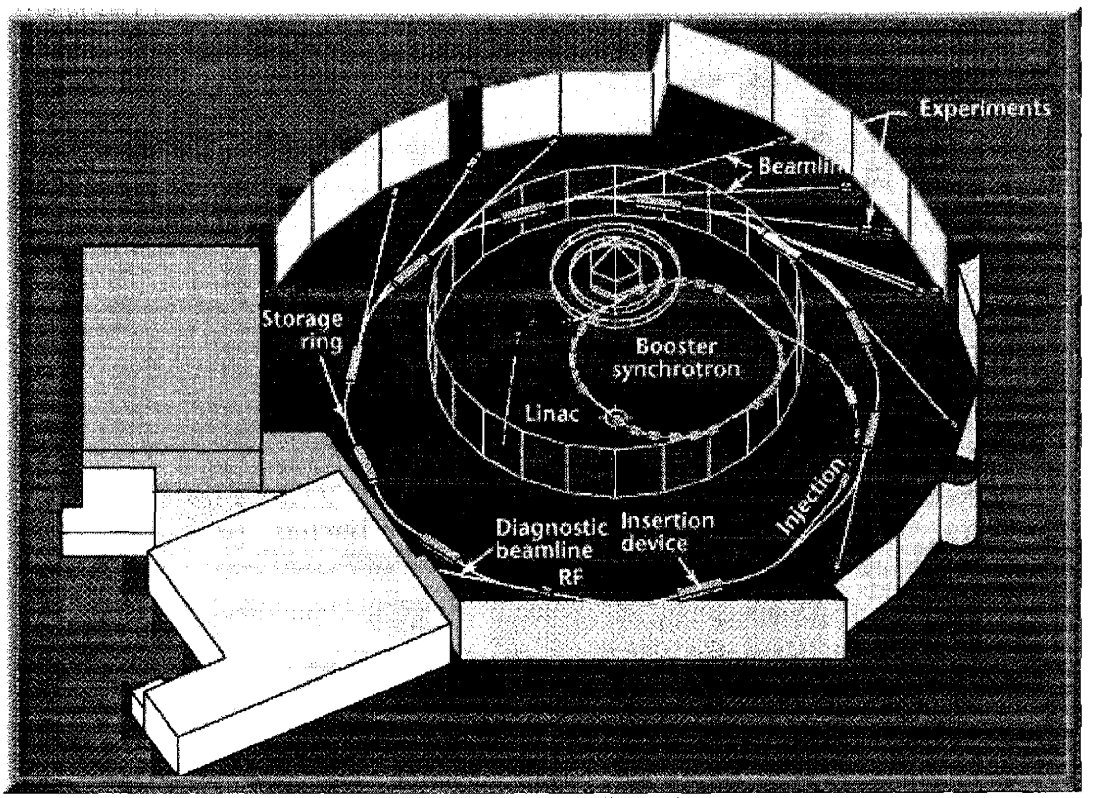

Figure 4.1 Synchrotron setup at the Advanced Light Source [1]

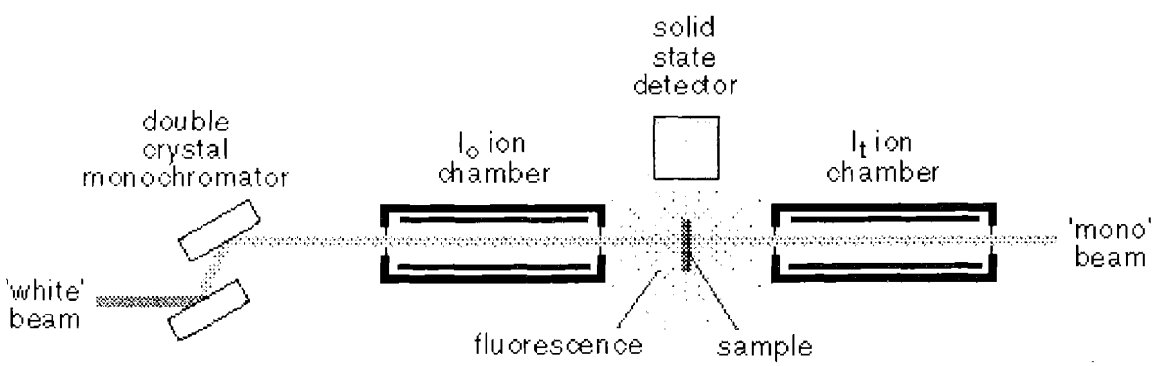

Figure 4.2 XAS detector setup

A typical XAS spectra is shown in Figure 4.3. The absorption edge (peak) corresponds to the energy where an incident x-ray photon can free an inner shell electron from the atom. Normally the first, most tightly bound shell, corresponding to the K-edge, or the second shell (L-edge) is used, though softer spectra such as at the Advanced Light Source at Lawrence Berkeley National Laboratory can be used to probe outer shells at lower energies. For actinide applications, the L_2 or L_3 edges are usually utilized.

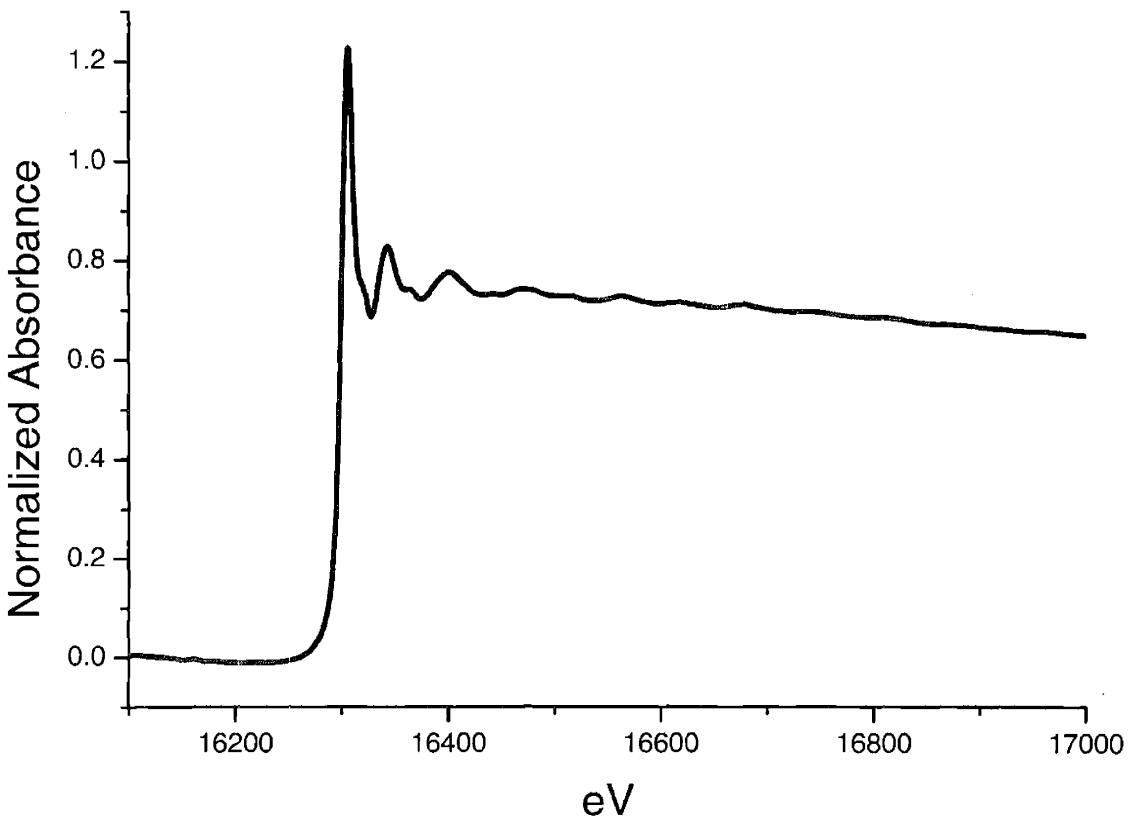

Figure 4.3 Typical XAS spectra. This is the Th L_3 edge of a ThO_2 sample.

The XANES portion of the spectra extends from the threshold to about 40 eV beyond the absorption edge. In this region, the photon is completely absorbed, creating an excited photoelectron and leaving a core hole in the atom. The absolute position of the edge can be used to determine the oxidation state of the core atom. For example, higher energies will be required to expel an inner shell electron from a more positively charged ion. The XANES region also contains information on vacant orbitals, electronic configuration, and site symmetry, as the photoelectron transitions to unfilled bound states, nearly-bound states, or continuum states of the appropriate energy [2].

Beyond the XANES region, sufficient energy is supplied that transitions are always to continuum states. In this region, the resulting photoelectron backscatters off of the nearest neighbors, affecting the x-ray absorption (Figure 4.4) and creating oscillations in the spectra above the absorption edge. These oscillations can be used to determine atomic number, distance, and coordination number of nearest neighbors. These oscillations appear as a superposition of the sine waves created by the interaction between the core atom and each shell. EXAFS does not occur for isolated atoms but only appears when atoms are in a condensed state [3].

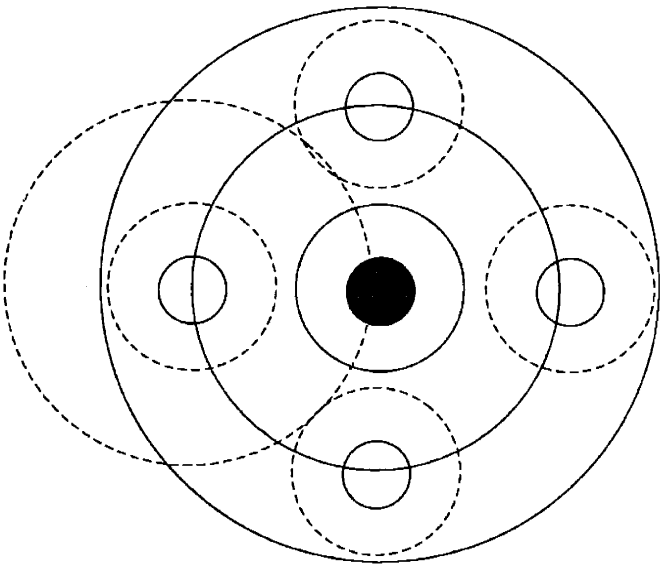

Figure 4.4 Propogation of the radial portion of the photoelectron wave. The solid line is the outgoing wave, the dashed lines depict the backscattering of the photoelectron in the EXAFS region.

In the EXAFS region, it can be the electron energy is sufficient that atomic interactions can be ignored, allowing the electron states to be approximated as plane waves weakly scattered by the atoms. This major assumption leads to the EXAFS equation, $\chi(k)$, derived by Sayers, Stern, and Lytle [4]:

$$\chi(k) = \sum_{i=1}^{n} \frac{N_i Amp(k)}{kR^2} \exp\left(-2\sigma_i^2 k_i^2\right) \sin\left[2kR_i + Phase(k)\right] \quad \text{Equation 4.1}$$

where N is the coordination number, R is the bond length between the core atom and coordination shell *i*, and σ^2 describes the disorder of the system as the mean square variation in the average R_i of shell *I* and has been expressed using a simple Einstein model of lattice variation [5] and as a function of temperature using the Debye approximation for lattice vibrations [6]. Amp(k) and Phase(k) are the backscattering

amplitude and phase shift. The phase and amplitude functions are specific to atomic interactions in a sample.

4.2 Data Analysis

XAS data analysis is typically performed by fitting collected spectra using computer models based on the EXAFS equation (Eq.1). Before a spectrum can be analyzed, however, it must first be processed to remove external effects such as background effects, x-ray absorption factors produced when the beam passes through sample windows, and uncertainties in sample composition. Appropriately processed spectra are then fit to model the interactions that create the EXAFS oscillations.

4.2.1 Data Reduction

Background removal is required to separate the EXAFS oscillations from the atomic part of the absorption. This is typically performed using least squares fitting, frequently using a cubic spline function. Exact sample concentrations and thicknesses are usually unknown. Normalization of data by the size of the edge step compensates for these uncertainties. Standards are used to account for effects of energy dependent absorption factors, which can be caused, for example, by the presence of the sample holder and the thickness of the sample. In addition, taking the log of transmission spectra reduces the effect of absorption factors from multiplicative to additive.

To compensate for the decay of waves as k increases, spectra are usually multiplied by some power of k. This is referred to as k weighting. Multiplying spectra by k^3 (k^3 weighting) makes the sine waves appear as a constant amplitude over k (Figure 4.5). Typical data ranges up to k=12, though in highly ordered samples

higher k ranges are achievable, while in low concentration samples the reverse is true. Averaging multiple spectra to decrease noise is typically used to increase the useful k range of a sample.

The signals from different shells are separated by performing a Fourier transform (Figure 4.6). This reduces the number of fitting parameters and thereby simplifies the process.

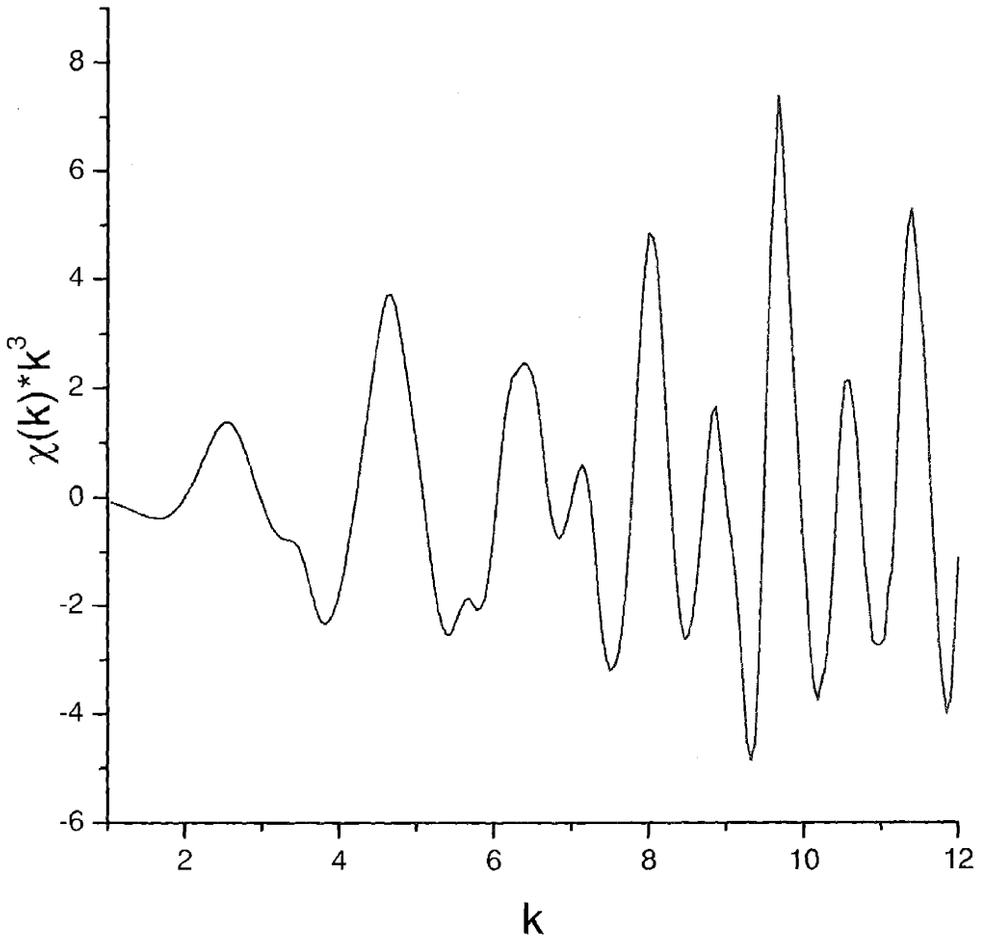

Figure 4.5 k^3 weighted EXAFS of ThO_2 spectra on L_3 edge.

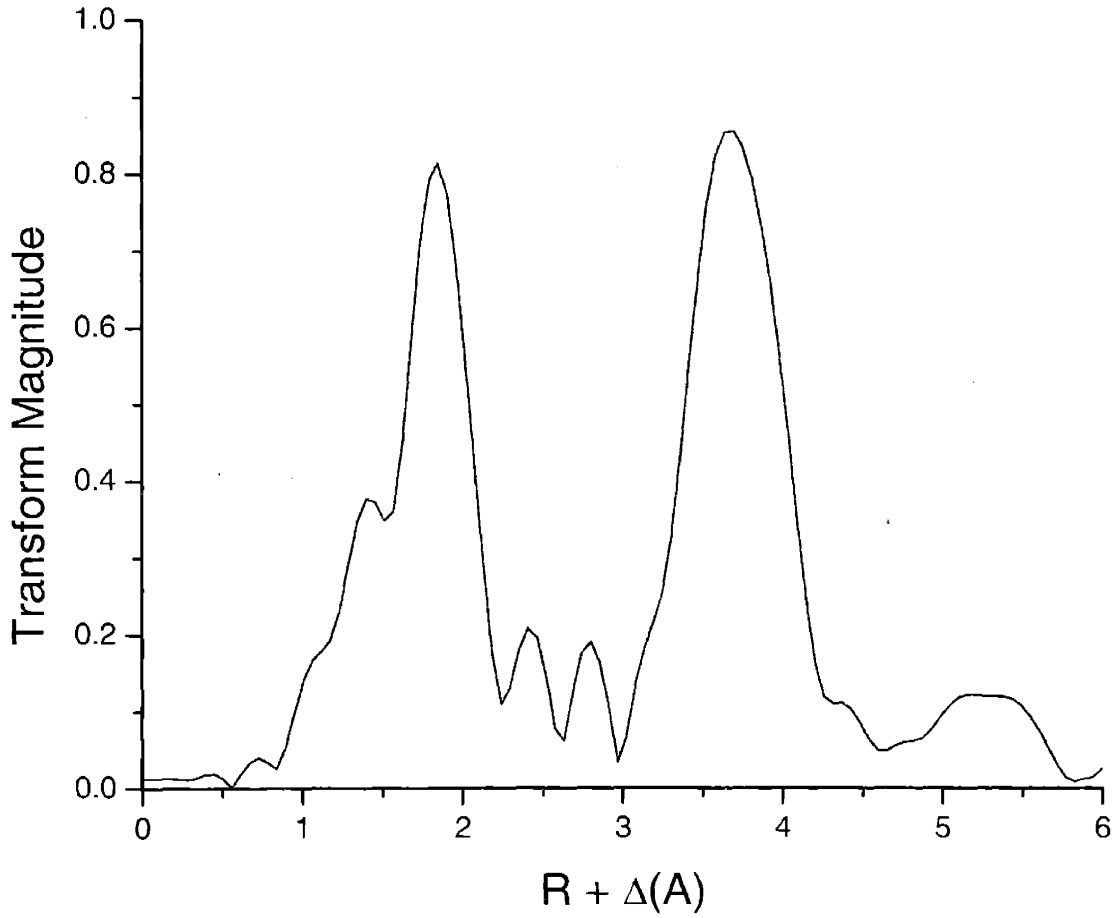

Figure 4.6 Fourier transform of the ThO_2 EXAFS spectra

4.2.2 *Fitting XAS spectra*

XAS data analysis software utilizes the EXAFS equation to fit experimental data by varying the parameters N_i (coordination number), R_i (bond length), and σ_i^2 (disorder). The identity of the ith shell atom is accounted for along with the absorber identity and the absorption edge in the phase and amplitude functions. The program FEFF [7] is utilized by most fitting programs, including EXAFSPAK [8] and GIFeffit [9], to calculate the phase and amplitude function for each possible path, including multiple scattering paths. FEFF paths are typically calculated using the closest possible structure in order to get the most accurate results. Structure inputs for FEFF can be created using ATOMS [10].

While the fitting software EXAFSPAK can utilize externally produced FEFF paths, a set of internal pre-calculated paths are also included for modeling individual molecular bonds. While the directly calculated paths tend to be more reliable and accurate for a particular system, the internal paths available in EXAFSPAK are useful for narrowing down possible structures in a complex system. These paths were used extensively in the data analysis for the heterogeneous metallic slag samples (Chapter 9), which had many possible structures.

Fitting is usually accomplished by varying N, R, and σ^2 or some combination of the three. When fitting spectra, care must be taken to ensure realistic results. In addition to unrealistic bond lengths and coordination numbers, the disorder term also serves as a reality check. For example, σ^2 cannot be less than zero, and large disorder terms indicate fitting errors or difficulties. Fits can be improved by a variety of methods, including shortening the k range and adjusting the FEFF input model. While shortening the k range can limit the number of shells that can be fit reliably, it can greatly increase the usefulness of the fit by eliminating excessively noisy data. Adjusting the FEFF input file is not always possible, as the exact structure may be a combination of phases or otherwise difficult to identify.

4.3 Conclusion

X-ray absorption spectroscopy is a useful technique for examining the local structure of molecules, and therefore for determining the speciation of an element in a matrix. Measurements are relatively quick with little required sample preparation. A variety of materials can be analyzed, including solid and solution forms. Because it is non-destructive, there is no interference with the elemental speciation, even in solution. It is a relatively sensitive technique, and spectra of dilute elements in complicated matrixes can be analyzed. It is therefore an ideal technique for examining speciation of actinides in complex environmental samples that would be too complicated to separate out without adversely affecting or changing the composition of the species of interest by other means.

References

1. Advanced Light Source, http://www-als.lbl.gov/als/quickguide/viewstouse.pdf
2. Bunker, Grant, **Elements of XAFS**, Physics Department, Illinois Institute of Technology, Chicago, IL
3. Konningsberger, D.C. and R. Prins, **X-Ray Absorption: Principles, Applications, Techniques of EXAFS, SEXAFS, and XANES**, John Wiley & Sons, USA 1988
4. Sayers, D.E., Stern, E.A. and Lytle, F.W. *Physics Review Letters*, **27** (1971) 1204
5. Stern, E.A., Bunker, B. and Heals, S.M. *Physics Review B*, **21** (1980) 5521
6. Beni, G. and Platzman, P.M. *Physics Review B*, **14** (1976) 1514
7. Rehr, J.J. et al, FEFF. University of Washington Department of Physics http://leonardo.phys.washington.edu/feff/
8. George, G.N. EXAFSPAK. http://www-ssrl.slac.stanford.edu/exafspak.html
9. Newville, Matt. IFEFFITT. http://cars9.uchicago.edu/ifeffit/
10. http://feff.phys.washington.edu/~ravel/software/atoms/Welcome.html

5 Analytical Techniques

A variety of techniques were used to analyze sample composition and actinide speciation for this thesis. Techniques utilized include inductively coupled plasma atomic emission spectroscopy (ICP-AES), inductively coupled plasma mass spectroscopy (ICP-MS), Brunauer-Emmett-Teller surface area analysis (BET), x-ray diffraction (XRD), and x-ray absorption spectroscopy (XAS).

5.1 ICP-AES Procedure

Samples with dissolved thorium and uranium concentrations around 0.1 through 10 μmol/L were analyzed using inductively coupled plasma atomic emission spectroscopy, ICP-AES. For the ICP-AES method, the liquid samples were fed directly as prepared into the instrument for analysis.

5.1.1 Principle of ICP-AES

The principle behind ICP-AES is that a plasma is generated by an igniting device consisting of an oscillating electromagnetic field established by a high frequency coil wrapped around a quartz torch. The oscillating field causes argon atoms to collide, transferring energy to other argon atoms, which become ionized and cause further collisions. This process continues until the plasma reaches a steady state. Aqueous samples are introduced into the system via a peristaltic pump, which pumps the sample through a nebulizer. The nebulizer creates a fine aerosol mist. Particles that are small enough to be excited by the plasma are carried away by argon gas into the plasma. Once in the plasma, sample atoms collide with the rapidly moving plasma atoms and become excited. These excited atoms eventually relax to a lower energy state and emit characteristic photons. A spectrometer, set to measure a

specific characteristic energy, measures the intensity of the emitted photons [1]. Figure 5.1 shows the basic arrangement of an ICP-AES. The operation of the plasma torch is depicted in Figure 5.2.

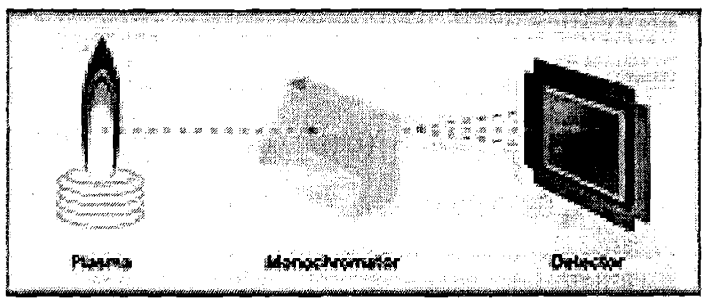

Figure 5.1 ICP-AES basic arrangement

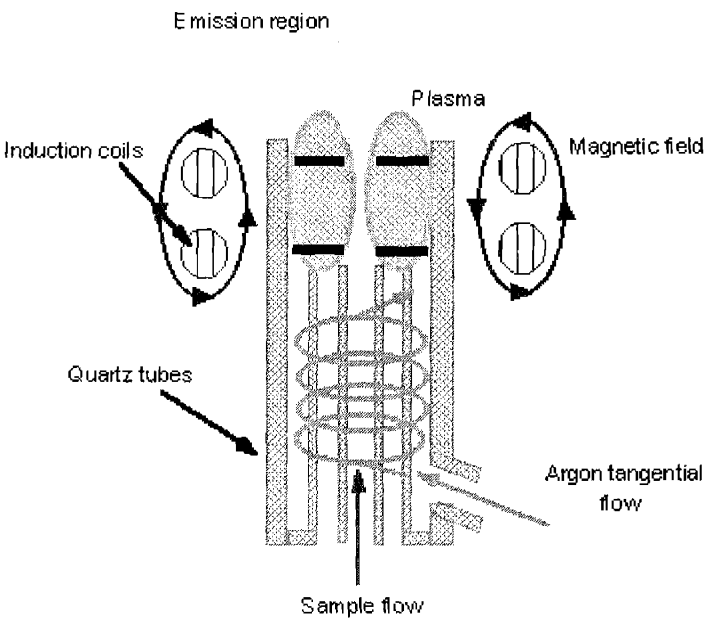

Figure 5.2 ICP-AES plasma torch operation

This sample analysis technique cannot tell an absolute concentration due to uncertainties in the nebulizer efficiency, optical efficiency, and other aspects of the system. A relative concentration can be determined by calibrating the system each time with known standards in order to determine the concentration in the samples.

Standard concentrations can range from the lower detection limit to just below the saturation point of the machine. A linear regression fit of the data from the standards is then used to determine the concentration of each unknown sample.

The best way to lower the detection limit of the system is to increase the efficiency of the nebulizer. A standard pneumatic nebulizer has an efficiency of around 1%-3%, while an ultrasonic nebulizer can have an efficiency as much as 15 times as high. In addition, samples should be slightly acidified in order to minimize sorption to the surface of tubes and glassware in the instrument, which can increase the background and therefore the detection limit of the machine.

5.1.2 Standard Preparation

The method of standard preparation and type of standard used for ICP-AES calibration can affect the quality of the data and is therefore very important. The most important aspect of standard preparation is to match the standard matrix to the sample matrix. This is to account for any interferences the matrix may cause with the optical line of interest. In order to account for any optical interference that the bright orange flame created by sodium in the torch may cause, all standards were prepared in a 0.1 M HNO_3 solution matching that of the samples. It is also important to create a large enough range of standards to cover the expected range of sample concentrations, so that a good calibration curve can be created in the correct region. This is especially important when determining concentrations near the detection limit of the instrument, since most curve fitting programs will preferentially weight the curve to the higher concentration data.

Initial analysis showed that sample concentrations ranged from below the detection limit of the instrument to approximately 10 µmol/L. Standards were prepared ranging from 0.1 µmol/L to 100 µmol/L by diluting Aldrich 970 µg/L (4.18 mmol/L) thorium atomic absorption standard solution with 0.1 M HNO_3 to match

the sample matrix. In addition, a 10 nmol/L standard was prepared in the same manner and used as a matrix blank in order to determine the background count rate of the instrument. This standard was chosen because it was well below the detection limit of the machine and consisted of the same matrix as the samples and the standards.

5.1.3 Procedure

The standard startup procedure for the Spectro Analytical Instruments Spectroflame ICP-AES was followed each time the instrument was used. A minimum warm-up time of 15 minutes was allowed while flushing the instrument with purified water at each startup. The sequential optics were then reprofiled in order to accommodate any changes in instrument operation parameters since the last use. Two thorium emission lines were available for use. The sample analysis method was set up to look at both lines simultaneously, but the 401.913 nm line was always preferentially used for data analysis due to its larger intensity and lower detection limit. The 283.730 nm line was mainly used to check that the ICP-AES was working properly. Uranium samples were analyzed on the 385.958 nm line. After reprofiling the optics, the location of the actual peak was checked against the machine determined location using the strongest standard in order to assure that the optics were properly calibrated. The location of the peaks did not move at any time.

The instrument was flushed with 5 vol% nitric acid after the peak location check in order to remove any lingering metals from the system. The background was then checked against the initial background to ensure that the system was clean. All poly tubes were replaced periodically to ensure the data was not affected by thorium plating on the tubing. In addition, the spray chamber and torch were cleaned by soaking in a 5 vol% hydrochloric acid bath for several hours followed by a thorough rinsing in purified water every month.

Once the lines were sufficiently clean, elemental standards were run in order of increasing concentration to create a calibration curve. A matrix background was taken before the first (lowest concentration) standard. After the final (highest concentration) standard was analyzed, the system was again flushed with 5 vol% nitric acid until the background returned to the initial level. This was double checked by running another matrix background for comparison to the previous one. Samples were then run in order of lowest estimated concentration to highest. A two minute 5 vol% nitric flush was performed between each sample in order to limit plating. Nitric backgrounds were taken periodically for comparison. During thorium analysis, very ten samples a blank matrix background was taken to further ensure that sorption of thorium to the instrument surfaces was not interfering with the data.

Following each ICP use, the instrument was shut down using the Spectro procedure. The instrument was flushed with purified water for a minimum of ten minutes before the torch was turned off. The system was then allowed to cool for another five to ten minutes and then turned off.

5.2 ICP-MS Procedure

Samples with concentrations below the detection limits of the ICP-AES were analyzed using a Fisons VG Plasmaquad II ICP-MS.

5.2.1 Principles of ICP-MS

In plasma mass spectroscopy, the inductively-coupled argon plasma (ICP) is once again used as an excitation source for the elements of interest. However, in contrast to plasma emission spectroscopy, the plasma in ICP-MS is used to generate ions which are then introduced to the mass spectrometer and focused by a cone. These ions are then separated by the a lens (ion separator). The ions change trajectory

when they enter the quadropole magnetic field (mass filter), and are collected according to their mass to charge ratios in electron multiplier cup detectors. The constituents of the unknown sample can then be identified and measured by the detectors. ICP-MS offers extremely high sensitivity for many elements and can also be successfully applied to a wide range of elements. Figure 5.3 shows the basic components of an ICP-MS system. Detection limits of ICP-MS systems can be from one to four orders of magnitude lower or more than their ICP-AES counterparts.

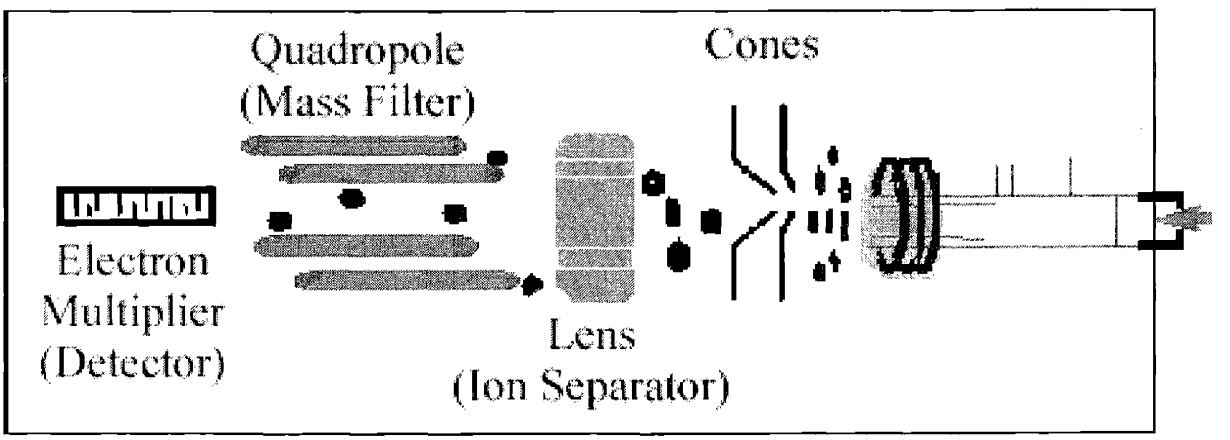

Figure 5.3 Major Components of an ICP-MS

Like ICP-AES, the ICP-MS technique is used to determine relative concentrations. Known standards must be use to calibrate the ICP data and determine actual concentrations.

5.2.2 Standard preparation

Standards were created using stock solutions purchased from SCP Science. 1000 µg/mL Th and U standards diluted in 5 vol% HNO_3 to cover a range of concentrations from 1 nM/L to 0.5 mM/L. For ICP-MS analysis, standards were spiked to 10 ppb ^{209}Bi for mass calibration.

5.2.3 *Procedure*

ICP-MS samples were prepared in a similar method to the ICP-AES samples. Samples were filtered with a 0.45 μm Acrodisc filter, then diluted to 0.1 M HNO_3 for analysis. Samples were then spiked to 10 ppb ^{209}Bi for mass calibration.

An initial calibration curve was created using the standards prior to running any samples. In addition, one standard was introduced every 3 or 4 samples in order to check and correct for any potential fluctuations. Samples were analyzed at the 232, 235, 238, and 209 mass lines. A minimum of three readings was taken for each sample. Between samples, the machine was flushed for 5 minutes with 5 vol% HNO_3. Sample uptake time was at least 60 seconds before any readings were taken.

5.3 BET Surface Area Analysis

Surface area measurements were taken of the thorium oxide powders after immersion in the flasks at various pH levels in order to look at how the surface of the powder was affected. Surface area was analyzed using a Quantachrome Nova 1000 instrument using grade 5.0 nitrogen gas.

5.3.1 *BET Method*

Experimental surface areas are most commonly obtained through the analysis of adsorption isotherms of nitrogen or some other gas. In the case of explicit-model analyses such as the Brunauer-Emmett-Teller (BET) method the experimental isotherm is fit to a theoretically-obtained adsorption model, from which is extracted a monolayer capacity of the material. This capacity is a well-defined quantity and can be used compare experimental and simulated systems. In order to convert to a surface area, a value for the monolayer density is needed, which is obtained

experimentally using a reference system of known surface area. The accuracy of this method requires that the monolayer density be transferable; that it is not dependent on the surface curvature or pore structure, and not strongly dependent on the chemistry of the underlying surface. The Nova 1000 surface area is shown in Figure 5.4.

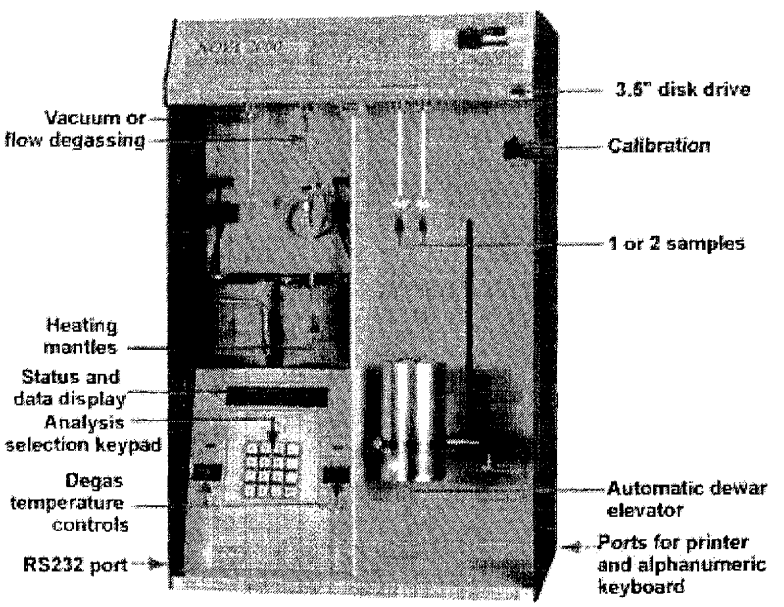

Figure 5.4 Quantachrome Nova 1000 BET surface area analyzer [2]

The tendency of all solid surfaces to attract surrounding gas molecules gives rise to a process called gas sorption. Monitoring the gas sorption process provides a wealth of useful information about the characteristics of solids. Before performing gas sorption experiments, solid surfaces must be freed from contaminants such as water and oils. Surface cleaning (degassing) is most often carried out by placing a sample of the solid in a glass cell and heating it under a vacuum. Once clean, the sample is brought to a constant temperature by means of an external bath. Then, small amounts of a gas (the absorbate) are admitted in steps into the evacuated sample chamber. Absorbate molecules quickly find their way to the surface of every

pore in the solid (the adsorbent). These molecules can either bounce off or stick to the surface. Gas molecules that stick to the surface are said to be adsorbed. Figure 5.5 shows this process. The strength with which adsorbed molecules interact with the surface determines if the adsorption process is to be considered physical (weak) or chemical (strong) in nature.

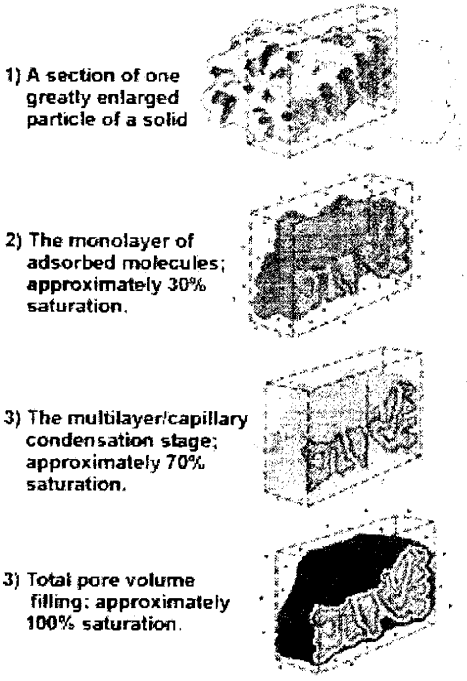

Figure 5.5 Surface adsorption of a gas

5.3.2 Sample Preparation

The thorium-uranium oxide pellets remaining in the flask at the end of each experiment were removed and placed in a 50 mL polypropylene centrifuge tube. Each sample was centrifuged for two to five minutes, and any excess liquid was removed with a plastic bulb pipette. The samples were then placed in a freeze drier overnight until completely dry.

5.3.3 *Procedure*

For each measurement, a thorium-uranium oxide pellet was placed into a preweighed sample tube. The sample was placed in a heating mantle and degassed at 300 °C for a minimum of three hours. After degassing, the sample and tube were removed and weighed in order to determine the degassed sample weight. The sample was then placed in a dewar of liquid nitrogen for analysis. Each sample was analyzed using a six point BET method a minimum of three times.

5.4 X-Ray Diffraction

X-ray diffraction (XRD) was used to look at the thorium oxide remnants after immersion in the various pH solutions and determine if any major changes of lattice parameter could be found. Both lattice parameter changes and surface area changes can affect the kinetics of thorium oxide dissolution.

5.4.1 *Principles of XRD*

X-ray diffraction is a versatile, nondestructive technique for quantitative analysis and qualitative identification of the various crystalline phases found in solid minerals and powders [3]. Identification is achieved by matching the pattern with a known pattern in a crystallography database. Databases can contain over 70,000 phases [4]. XRD is based on Bragg's law:

$$n\lambda = 2d \sin\theta \qquad \text{Equation 5.1}$$

Crystalline structures are composed of three-dimensional rectangular lattices arranged so that they form a series of parallel planes separated from each other by a

distance d. The distance varies according to the characteristics of the material. In a crystal, the planes exist in a number of different orientations, each with its own d-spacing. To create a diffraction pattern, monochromatic x-ray beam of wavelength λ is projected into a crystalline material. As the beam moves over the sample, the angle of incidence θ changes. Diffraction occurs only when the distance traveled by the x-rays differs by a complete number n of wavelengths. This occurs when Bragg's law criteria are met. This is shown in Figure 5.6. A plot of the angular positions and intensities of the resulting peaks is compared to the database to determine the structure and composition of a crystalline material.

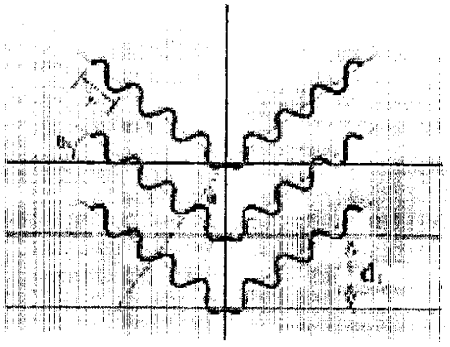

Figure 5.6 Bragg's Law

5.4.2 Sample Preparation

Samples of the dried thorium oxide remnants from the flask solutions were used for XRD. X-ray diffraction slides were prepared by combining approximately 100 mg of thorium oxide powder with 20 to 50 mg of standard material. Silicon carbide was used for the initial slides from the argon atmosphere experiments, and NIST traceable silicon 640c standards were used for the remaining samples. Standard materials were added in order to adjust for any shift in lattice parameter. The thorium powder/standard mixture was added to a three to one mixture of amyl

acetate and collodium, stirred, and painted on a small piece of glass microscope slide cut to fit into the sample holder.

5.4.3 *Procedure*

Sample analysis was performed on a Rigaku RU300 x-ray generator with a 185 mm diffractometer operating at 60 kV and 300 mA (18 kW). Scans were performed for theta ranging from 20 to 80 degrees in steps of 0.05 degrees. 1.0 mm divergence and scatter slits were used, and a 0.3 mm receiving slit was used. Scans were analyzed for diffraction pattern matches using Jade.

5.5 X-Ray Absorption Spectroscopy

X-ray absorption studies were performed primarily at the Stanford Synchrotron radiation laboratory. Some additional data was collected at the National Light Source at Brookhaven National Laboratory.

5.5.1 *Principles of X-Ray Absorption Spectroscopy*

X-Ray Absorption Spectroscopy (XAS) utilizes a tunable x-ray source to probe local structure of molecules. Synchrotrons are typically used for their high energies and broad spectral ranges. A complete description of the principles of XAS is given in Chapter 4.

5.5.2 *Sample Preparation*

XAS samples were prepared by mixing 20-50 mg of finely milled actinide-bearing powder into a matrix of 150-200 mg of biobeads, an x-ray transparent resin. This mixture was placed in an aluminum window between two pieces of kapton tape. Samples were then heat sealed in two layers of polypropylene to ensure no actinides escaped during data collection.

5.5.3 *Procedure*

Actinides were scanned on their L_3 edges, other elements present were scanned on their K edges if the data was of interest. Samples were typically scanned to k=14, though shorter ranges were sometimes used due to time constraints or limited usefulness of the extended k range. The majority of samples were concentrated enough to be scanned in transmission mode. Usually only one, but sometimes two or three scans were taken of each sample. Lower concentration samples were scanned in fluorescence mode using either a multielement solid state detector or a Lytle detector. Data was collected on Beam Line 4-1 or 11-2 at Stanford Synchrotron Radiation Laboratory. When possible, standards were used for calibration of the data. The procedure for data analysis is explained fully in Chapter 4.

5.6 References

1. Gill, Robin, **Modern Analytical Geochemistry**, Longman Singapore Publishers, LTD, Singapore, Indonesia 1997 pp. 41-60
2. Quantachrome Incorporated, http://www.quantachrome.com/
3. Phillips Analytical, Introduction to X-ray Diffraction, http://www-us.analytical.phillips.com/technologies/xrd/
4. International Crystal Diffraction Database, http://www.icdd.com/

6 Synthesis and Characterization of Zirconia-Thoria-Urania fuels

6.1 Introduction

Thorium based fuels have regained favor in the nuclear engineering community as a potential future fuel source. The potential for higher achievable burn-up and reduced proliferation concerns (significantly less fissile material, such as ^{239}Pu, is produced in thorium based fuels) put these fuels in a favorable light. Unfortunately, thorium compounds (specifically ThO_2) have not been studied very extensively in a method to obtain sufficient and accurate data for modeling. In addition, because the spent fuel will be subjected to high doses of radiation in the repository environment for many years, it is important to understand how the radiation will affect dissolution of the fuel matrix and its potential impact on the speciation of the actinides in the fuel.

An important assumption for the ceramics aspect of the project is that the spent fuel will be placed directly into the repository as the waste form, with no intermediate processing steps. Because of this, the ceramics must fulfill the dual role of fuel form and waste form. For the fuel form, the densest possible ceramic with an appropriate thorium to uranium ratio is desired in order to minimize the size of the core. For the waste form, it is important that the ceramic is a stable long term storage material. Therefore, the ideal ceramic form will be the one that balances density with stability.

For this portion of the project, thoria-urania ceramics were produced with varying amounts of zirconia added to stabilize the fuel. The structure of the ceramics was analyzed using XAFS and compared to results obtained from complementary x-ray based techniques including XRD, EELS, and EDX. The effect of the zirconia

stabilization was then assessed by dissolving the ceramics in low ionic strength solutions over a range of pH under both argon and a mixture of argon and 10% CO_2. The best candidates for use as fuels were then dissolved under air in a high gamma radiation field to evaluate the effects of radiation on solubility of the actinides that are the backbone of the fuel matrix.

Characterization by X-ray and Electron Interactions

6.2 Abstract

X-ray and electron interactions with matter were used as probes to characterize the structure and chemistry of zirconia-thoria-urania ceramics. The ceramics were prepared by coprecipitation of the Zr, Th, and U salts. In this study, electron microscopy techniques such as energy dispersive x-ray (EDX) analysis and electron energy loss spectroscopy (EELS) complement x-ray diffraction, extended x-ray absorption fine structure (EXAFS) and x-ray absorption near edge spectroscopy (XANES) techniques to reveal of the phase structure and chemistry. The results from XRD and EDX show that these ceramics separate into a Zr-based phase and an actinide-based phase with low mutual affinity of Th and Zr, as well as partial solubility of U in Zr. The comparison of EELS spectra collected for the ceramics with spectra collected for UO_2 and U_3O_8 reference materials also allow us to assess U oxidation state independently in the two separate phases.

6.3 Introduction

There has been a recent resurgence of interest in Th as a potential fuel for generation IV nuclear energy. It is thought that ThO_2-UO_2 will be less expensive to fabricate than standard UO_2 fuel, result in a more stable and insoluble waste form, and be resistant to weapons-material proliferation [1]. The intent of this work is to synthesize and characterize a series of ThO_2-UO_2 ceramics with varied amounts of ZrO_2. The ratio of Th to U is held at 3 based on reactor physics considerations. The overall metal stoichiometry is Zr_xTh_3U with x = 0, 1, 3, and 6. While this work examines a range of relative Zr concentration, in the case of a realistic fuel only the lowest Zr concentrations can be considered. The characterization will reveal the

speciation of the actinides in the ceramics and the information will be used in the further analysis of actinide solubility.

The addition of ZrO_2 in the ceramic material is based on the expected enhancement in chemically stable and radiation resistance [2]. The natural analogue of zirconia, baddeleyite ($(Zr,M)O_2$), where M is a tetravalent ion such as hafnium), contains up to 3,000 ppm U or Th [3]. Negligible or no lead loss (a stable decay product of U and Th) in natural baddeleyites indicates high, long term, chemical durability of the material in the environment [3]. Studies have shown that zirconia is more radiation resistant than both pyrochlore ($Gd_2Ti_2O_7$) and zirconalite ($CaZrTi_2O_7$) ceramics [2,4].

There has been previous work on the fabrication and characterization of UO_2-ThO_2 ceramics [5,6]. Various zirconia containing ceramics have been fabricated and studied, including ZrO_2-PuO_2, ZrO_2-UO_2, ZrO_2-Gd_2O_3-PuO_2, ZrO_2-Y_2O_3-NpO_2, ZrO_2-ThO_2, and ZrO_2-CeO_2 [2,7-12]. Ceramics that have been fabricated frequently contain Y_2O_3 (up to 15 mol% [2]) binder in order to stabilize the ceramic. Though there have been problems with urania-thoria phase separation, the inclusion of Zr in the lattice tends to strengthen the bonding [5], and all of these ceramic compositions have shown superior durability to their zirconia free counterparts [2,4,6].

Uranium and thorium dioxide have the same fluorite structure with similar lattice constants, 5.468 and 5.59 Å respectively. They form perfect solid solutions with a fluorite structure and a cell parameter characteristic of the phase composition. The unit-cell parameter of the solid solutions follows almost exactly a straight-line relation with composition [13]. For the UO_2-ZrO_2 and ThO_2-ZrO_2 systems, two solid solutions are formed: $(ZrO_2)_{SS}$ and $(MO_2)_{SS}$, where M=U or Th. There is little mutual solubility of the actinides in ZrO_2 under the conditions examined [13,14]. While there is a fairly diverse array of data on the behavior of thoria, urania, and zirconia, no studies of a combined ZrO_2-ThO_2-UO_2 system have been published.

This study focuses mainly on establishing the phase structure and composition of selected zirconia-thoria-urania ceramic systems. In addition, U oxidation state is known to be one of the key factors controlling U solubility. Therefore, the U oxidation state in the ceramics is characterized. The ceramics are used in solubility experiments to thermodynamically and kinetically evaluate the component material dissolution and acquired data for modeling the repository behavior of the ceramics [15].

6.4 Experimental

6.4.1 Ceramic preparation

Computer simulations showed that a 3:1 Th:U ratio offered the best compromise for fuel applications. This ratio will therefore remain constant for this study and only the Zr content will be varied to determine the ideal matrix in terms of waste form. The ceramics under investigation have a constant Th:U ratio of 3:1 and an overall metal ratio of Zr_xTh_3U with x = 0, 1, 3, and 6. Simple compositions of Zr:Th and Zr:U binary systems were also synthesized for this study.

The ceramics were fabricated from a solution of uranyl nitrate ($UO_2(NO_3)_2.6H_2O$), thorium nitrate ($Th(NO_3)_4.4H_2O$), and zirconyl chloride ($ZrOCl_2.8H_2O$) dissolved in 100 mL of water. The Zr, Th, and U were slowly coprecipitated out of solution in a mixture of oxalic acid and an excess of NH_4OH. Once the precipitate settled, the excess liquid was drained and the precipitate was washed, twice with purified water and twice with acetone. This yielded a mixture of oxalates and hydroxides. The final washed precipitate was then placed in an oven at 90°C to dry overnight. After the first drying period, the precipitate is removed from the oven and ground in a porcelain mortar to a homogenous powder. The powder was then further dried at 150°C for several hours, calcined at 700°C for one hour and

then cold pressed in a 13mm or 7 mm cylindrical die at 55 MPa for 2 minutes. The resulting pellets were sintered at 1500°C under a 3 % H_2/1%O_2/96 % Ar atmosphere for 4 hours in order to reduce the U from U(VI) to U(IV). For some samples, 0.5 wt % magnesium oxide was added to the powder after the calcination step as a binder in order to increase the ceramics density and strength.

6.4.2 Sample Characterization

TEM, EDX, EELS, and some of the XRD work were performed by Yoann Sevestre at MIT.

6.4.2.1 TEM

The synthesized ceramic materials were prepared for TEM analysis by mechanical polishing and ion milling with an incident angle of 15°. The analysis was carried out on a Jeol 200 TEM and was mainly focused on the grain structure of the ceramics, the average grain size being measured on negative films.

6.4.2.2 EDX and EELS

The ceramic samples prepared for TEM were also evaluated by EDX and EELS. The samples were coated with a 200Å conductive carbon layer in order to avoid electromagnetic charging of the material. The UO_2 and U_3O_8 reference samples for EELS were prepared by embedding standard powdered materials, from Alfa Aesar and NBL respectively, in epoxy resin and thin sectioning the resin blocks. The sections produced by this technique were laid on 200 mesh copper grids and carbon coated. A ThO_2 sample was also prepared the same way, using precipitated and calcined powder. The EDX and EELS analyses were carried out on a VG HB603

scanning transmission electron microscope operated at 250 kV with a filed emission gun, and equipped with a large angle x-ray detector and a parallel EELS spectrometer. The integration time for EELS analysis was 8 s, and 10 to 25 readouts were accumulated for each spectrum depending on the sample thickness. Data was collected using ELP software and acquisition was carried out at 0.5 eV/Channel. The peaks on EELS spectra for the ceramic samples were identified by comparison with the spectra collected for the reference materials. Slight energy shifts were observed due to gun voltage fluctuations throughout the experiment but they were considered to have no influence on the edge shapes. ORIGIN software was used to correct the baseline of EELS spectra and to calculate the peak area for U M_4 and M_5 edges.

The EELS technique has close similarities with the corresponding XAFS techniques and can be used to evaluate the oxidation state of elements. More specifically, the two intense features on the M_4 and M_5 edges of the actinides correspond to the two electronic transitions $3d_{3/2} \rightarrow 5f_{5/2}$ and $3d_{5/2} \rightarrow 5f_{7/2}$, respectively, that arise from the spin-orbit splitting [16]. In the case of rare earths, the M_4/M_5 ratio is observed to decrease with increasing 4f orbital occupancy [17] and the M_4/M_5 ratio obtained with EELS has been used to determine the oxidation state for rare-earth elements [18]. Although it is tempting to extrapolate from the 4f chemistry to deduce the behavior for the 5f elements, no data has been published so far in this area and caution must be used as the itinerant nature of the 5f orbitals leads to strong hybridization with the 6d and 7s orbitals [19]. In this study, the spectra collected for the various ZrO_2-ThO_2-UO_2 systems will be compared versus UO_2 and U_3O_8 reference sample spectra, focusing on the M_4/M_5 ratio to assess the oxidation state of uranium in the ceramics. The data will be compared with the other technique to validate the oxidation state analysis.

6.4.2.3 XRD

For x-ray powder diffraction the ceramic pellets were ground into a powder, mixed with 1/3 collodion/amyl acetate solution and 2-3 mg of 640c silicon standard from NIST used as an internal reference for peak calibration. The analysis was performed using a Rigaku 300 diffractometer and Cu Kα radiation. Phase characterization was completed using Jade software and lattice parameters were determined by performing a least square regression on the 2θ-values for the 10 most intense peaks on the calibrated patterns.

6.4.2.4 XAS

Preparation for XAS analysis consisted of grinding each sintered pellet into a fine powder. Approximately 50 mg of powder from each pellet was mixed with 200 mg BioBeads and sealed in an aluminum window with Kapton tape. Several transmission spectra were taken for each sample. Samples were scanned over the Th and U L_3-edges and the Zr K-edge. Simultaneously measured UO_2 standard, Zr metal standard, and Th_3UO_8 sample were used for calibration of the absorption edge. EXAFS and XANES data was collected at the Stanford Synchrotron Radiation Laboratory (SSRL). Raw data treatment and analysis was performed using standard methods reviewed elsewhere [20,21] using EXAFSPAK, developed by George of SSRL. Autobk [22] was used to fit $\mu_o(E)$ using a piecewise spline for the U and Zr data. Phase and amplitude functions were calculated using FEFF8.1 developed by Rehr et al [23, 24].

6.5 Results and Discussion

6.5.1 Density

After sintering, the diameter and thickness of the pellets were measured and the samples were weighed to determine the ceramic density. Inclusion of Zr in the ceramics decreases density while the addition of magnesium oxide increases ceramic density from 5 % to 20 %, the effect of magnesium oxide increasing with increased Zr content. The ceramics average grain size varies from 0.4 to 0.8 μm.

6.5.2 Spectroscopic Analysis

6.5.2.1 XRD Results

The results of XRD analysis are presented in Table 6.1. The analysis of the binary systems reveals mutual affinities between the various species. As expected from previous studies, U and Th show perfect solubility. When UO_2 and ZrO_2 are sintered together, a metastable Zr-based tetragonal phase is formed, revealing solubility of U in Zr, contrary to the case of Th and Zr where two thermodynamically stable phases form. The phase structure of the ternary ZrO_2-ThO_2-UO_2 systems is clearly established. Regardless of the Zr content, a ThO_2-UO_2 solid solution with a fluorite structure separate from a ZrO_2 based phase forms. The ZrO_2 phase contains UO_2 and MgO. In the case of UO_2-ThO_2 solid solutions, the U/Th ratio is determined by assuming a straight-line relation between the cell parameter and the phase composition using Jade reference data (Table 6.2). The variation in the specific Th:U ratio for the solid solutions is due to the formation of a separate Zr-U phase.

Standards	Major Phases	XRD Matching Structures	Reference Jade PDF #
ZrO_2	1	ZrO_2 (baddeleyite)	37-1484
$ZrThO_4$	2	ThO_2	42-1462
		ZrO_2 (baddeleyite)	37-1484
$ZrUO_4$	1	ZrO_2 (tetragonal)	42-1164
$ZrUO_4$	2	U_3O_8	31-1424
		ZrO_2 (tetragonal)	17-0923
Samples			
(Metal Ratio)	**Major Phases**	**XRD Matching Structures**	**Reference Jade PDF #**
Th_3UO_8	1	$(ThO_2)0.75$-$(UO_2)0.25$	30-1360
$ZrTh_3U$	2	$(ThO_2)0.5$-$(UO_2)0.5$	33-1368
		ZrO_2 (cubic)	20-0684
$ZrTh_3U$ +Mg	2	$(ThO_2)0.5$-$(UO_2)0.5$	33-1368
		ZrO_2 (tetragonal)	42-1164
Zr_3Th_3U	2	$(ThO_2)0.75$-$(UO_2)0.25$	30-1360
		ZrO_2 (cubic)	27-0997
Zr_3Th_3U+Mg	2	$(ThO_2)0.75$-$(UO_2)0.25$	30-1360
		ZrO_2 (baddeleyite)	37-1484
Zr_6Th_3U	2	$(ThO_2)0.5$-$(UO_2)0.5$	33-1368
		ZrO_2 (baddeleyite)	37-1484
Zr_6Th_3U+Mg	2	$(ThO_2)0.5$-$(UO_2)0.5$	33-1368
		ZrO_2 (baddeleyite)	37-1484

Table 6.1. Phase Characterization of Standards and Samples by XRD

Sample Metal Ratio	Cell parameter (Å)	Th-U Composition
PDF database Ref 33-1368	5.530	$Th_{0.5}U_{0.5}O_2$
PDF database Ref 30-1360	5.559	$Th_{0.75}U_{0.25}O_2$
Zr_6Th_3U	5.552±0.010	$Th_{0.69}U_{0.31}O_2$
Zr_6Th_3U	5.551±0.007	$Th_{0.68}U_{0.32}O_2$
Zr_6Th_3U +Mg	5.551±0.006	$Th_{0.68}U_{0.32}O_2$
Zr_3Th_3U	5.554±0.006	$Th_{0.71}U_{0.29}O_2$
Zr_3Th_3U +Mg	5.565±0.007	$Th_{0.8}U_{0.2}O_2$
$ZrTh_3U$	5.521±0.005	$Th_{0.42}U_{0.58}O_2$
$ZrTh_3U$ +Mg	5.524±0.006	$Th_{0.45}U_{0.55}O_2$
Th_3U	5.559±0.003	$Th_{0.75}U_{0.25}O_2$

Table 6.2. ThO_2-UO_2 Solid Solution Compositions and Cell Parameter from XRD Analysis

6.5.2.2 EDX Results

On the EDX elemental mappings (Figures 6.1 and 6.2), two separate phases clearly appear for all the ternary systems. One phase shows a high Th concentration and the other a high Zr concentration. This confirms the previous XRD results and the mutual solubility of Zr and Th are low. Uranium is present in both Zr and Th phases in significant levels. Magnesium is homogenously distributed throughout the ceramics. The key result of this analysis is that the synthesis method provides good

homogenous composition of the starting material and the phase separation occurs during the sintering phase.

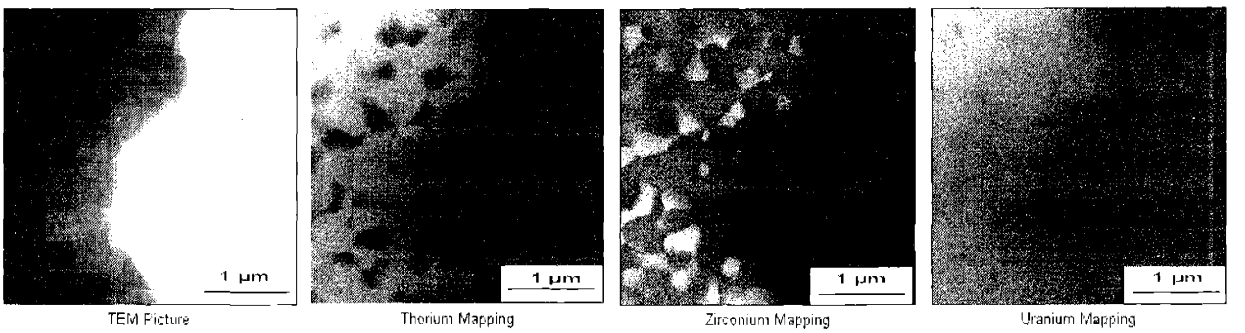

Figure 6.1. EDX Elemental mapping of ceramic with $ZrTh_3U$ metal ratio. The elements under consideration appear in bright shades. Thorium and zirconium mappings appear as negatives of each other, showing low mutual solubility of these two elements. Uranium is homogenously distributed throughout the ceramic.

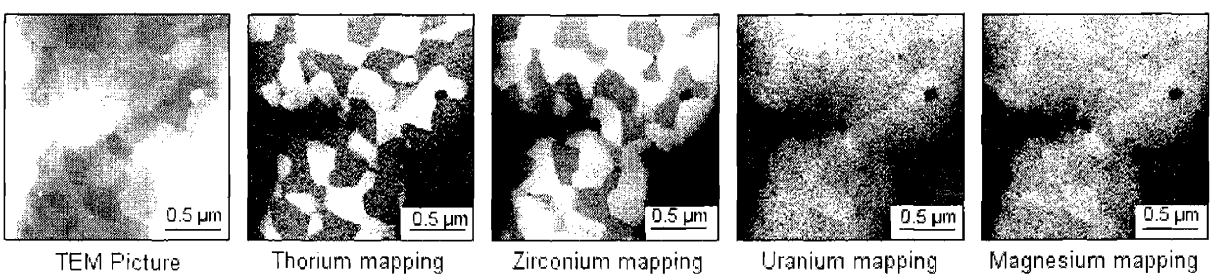

Figure 6.2. EDX Elemental mapping of Zr_6Th_3U metal ratio + 0.5wt% MgO. Thorium and zirconium separate in two different phases. Uranium and magnesium are homogenously distributed throughout the sample.

6.5.2.3 EELS Results

The EELS spectra were collected for each UO_2 and U_3O_8 reference samples on the thin areas of different grains (Figure 6.3). For the ceramic samples, the Th rich phase spectra are easily recognizable from the low Th phase spectra as the Th edges are less intense than the U edges. This result confirms the EDX observations. The average M_4/M_5 ratios were calculated for the standards and the samples (Table 6.3). Differences between the UO_2 and U_3O_8 ratio values are observed and the oxidation state of U samples can be determined with this method. The results show oxidation of U is found in the Zr phase.

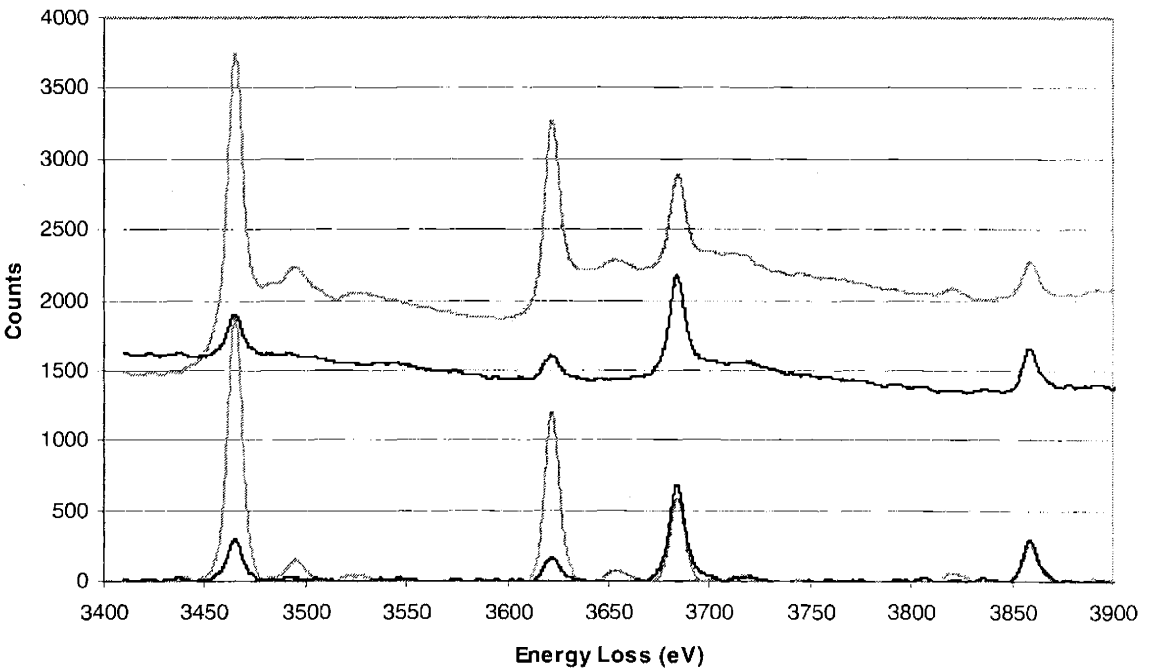

Figure 6.3. EELS Spectra of ceramic samples. (a) Th_3UO_8 raw data, (b) $ZrTh_3UO_{10}$ low thorium phase, (c) baseline correction of spectrum (a), (d) baseline correction of spectrum (b). In low thorium phases (spectra b,d) thorium edges are less intense than the corresponding uranium edges.

Standards	M_4/M_5
UO_2	0.41±0.03
U_3O_8	0.48±0.03
Samples (Metal Ratio and Phase)	**M_4/M_5**
Th_3U	0.40±0.04
$ZrTh_3U$ (Th phase)	0.41±0.04
$ZrTh_3U$ (Zr phase)	0.46±0.07
Zr_3Th_3U (Th phase)	0.43±0.06
Zr_3Th_3U (Zr phase)	0.45±0.06
Zr_6Th_3U (Th phase)	0.45±0.08
Zr_6Th_3U (Zr phase)	0.51±0.12

Table 6.3. M_4/M_5 Ratio for U in Standards and Samples

6.5.2.4 XANES Spectra

Thorium spectra were scanned on the Th L_3-edge to k=13 in order to avoid the U pre-edge. Thorium XANES spectra were consistent with ThO_2, as expected for the Th(IV) environment. The Zr K edge was scanned to k=14 revealing some fine structure in the pre-edge. The U L_3 edge was scanned to k=14 and the peaks appear to shift to the right with higher zirconia content. The U XANES spectra lack the characteristic shoulder indicative of uranyl, and appear shifted to higher energies than the UO_2 standard, indicating an intermediate oxidation state (Table 6.4). The spectra shift to higher energies as the zirconium content increases.

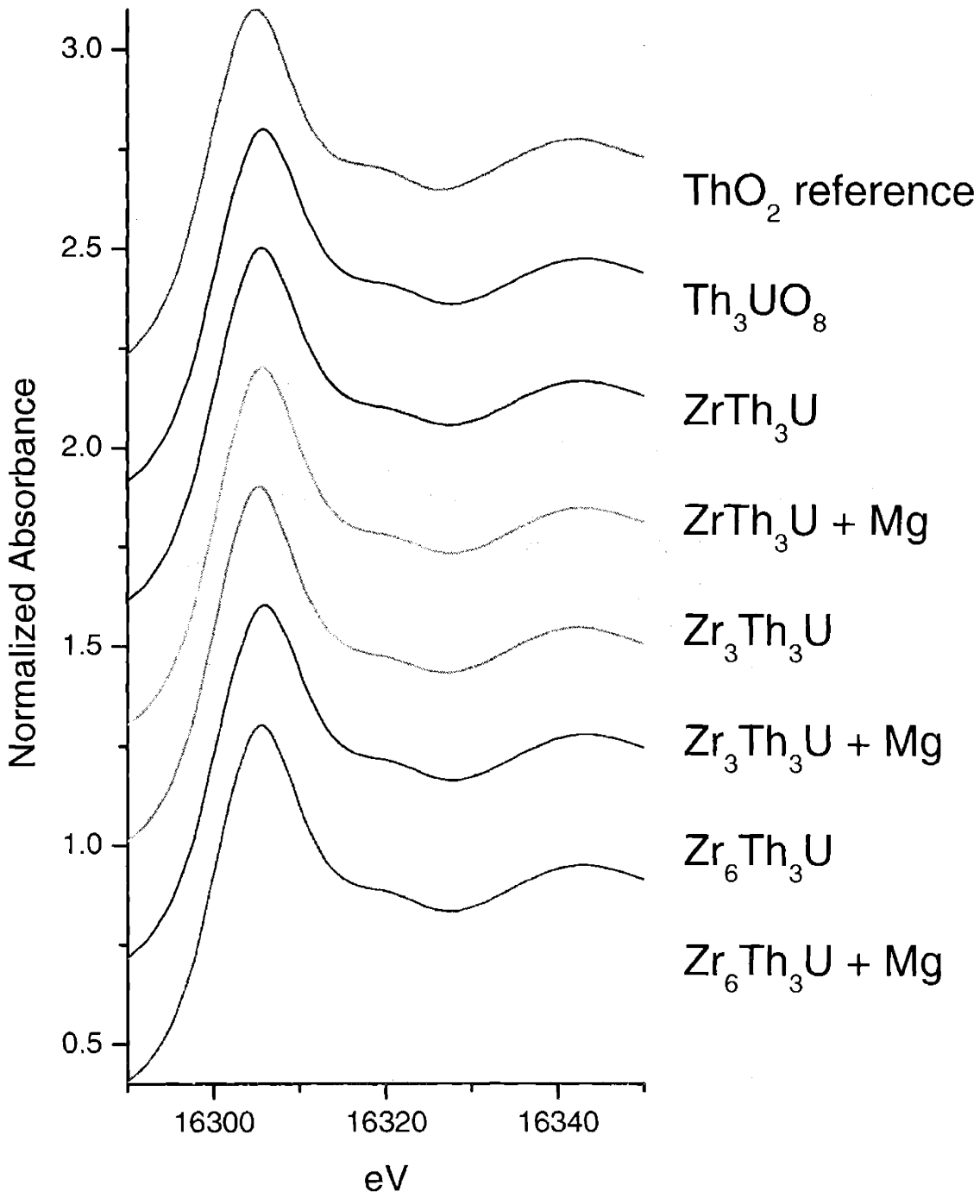

Figure 6.4 Thorium L_3-edge XANES spectra for the samples and standard.

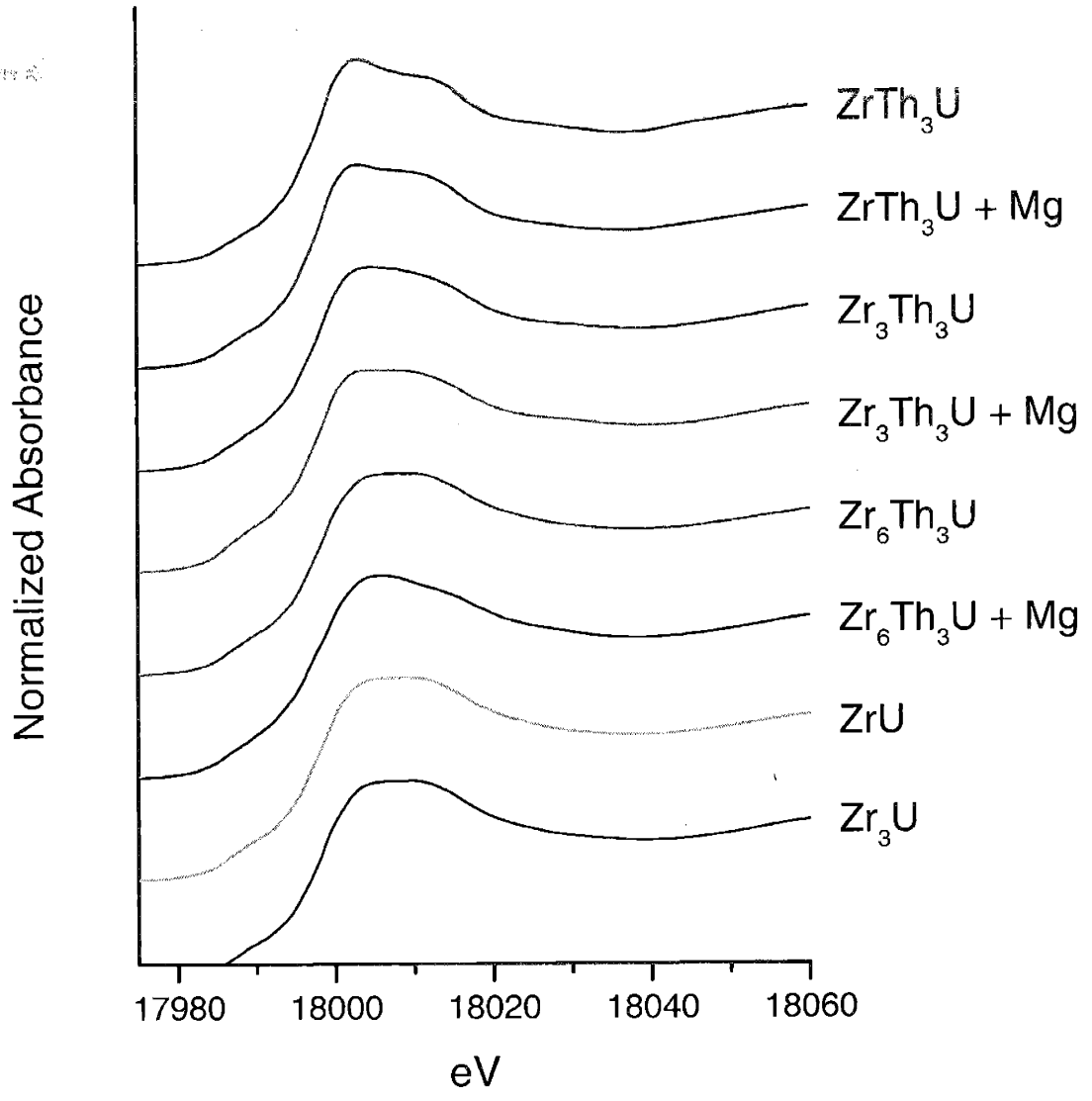

Figure 6.5. Zirconium K-edge XANES spectra

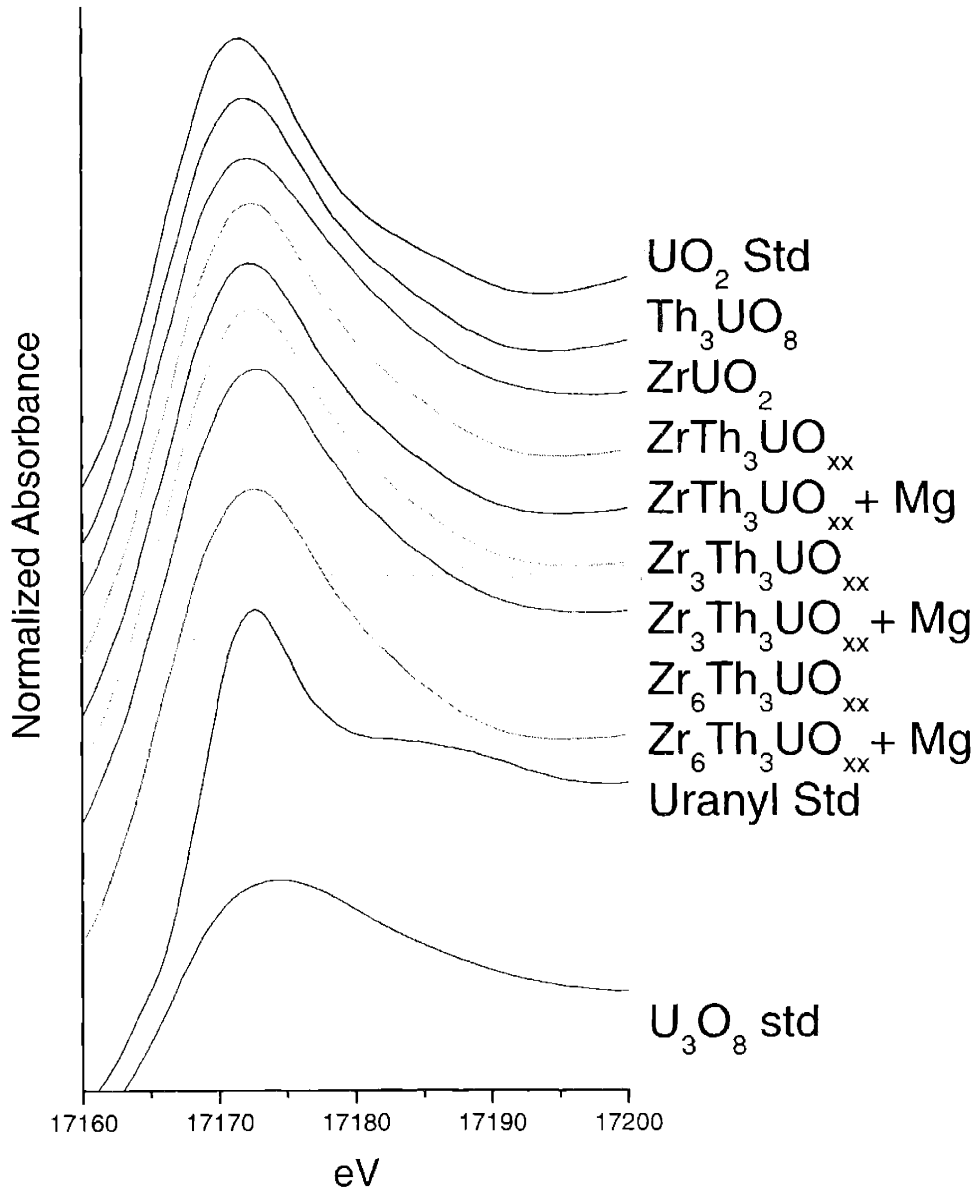

Figure 6.6. Uranium L_3 XANES spectra for the uranium standards and samples.

6.5.2.5 EXAFS Results

Average bond lengths and coordination numbers from the EXAFS analysis are given in Table 6.4. The Fourier transforms of the Th data confirm the structural similarities to ThO_2 (Figure 6.7). Uranium and Th are completely interchangeable in the Th oxide lattice. Analysis of the U Fourier transforms (Figure 6.8) showed that all samples exhibited contracted U-O bond lengths when compared to the UO_2 reference. Contraction increased with increasing Zr content, verifying the increasing oxidation of U with Zr content observed by EELS and XANES. Analysis of the Zr spectra for each sample showed that the average Zr-M bond length decreased with increasing Zr content (Table 6.5). The addition of 0.5 wt% MgO decreased the average Zr-M bond length for the $ZrTh_3U$ sample, but had no noticeable effect on the higher Zr content samples. This shortened average bond length appeared to effect the amount of U in the zirconia lattice. Curve fitting of the $ZrTh_3U$ samples with and without MgO showed that the samples with no MgO fit best with a U placed at the second position, while those with Mg fit best with a Zr at that position (Figure 6.9 and 6.10).

Bond	N	R(Å)
Th-O	8	2.40 ± 0.01
Th-U	12	3.94 ± 0.01
Th-Th	12	3.94 ± 0.01
U-O	8	2.28 ± 0.03
U-M	12	3.91 ± 0.02

Table 6.4 An-M and An-O bond lengths

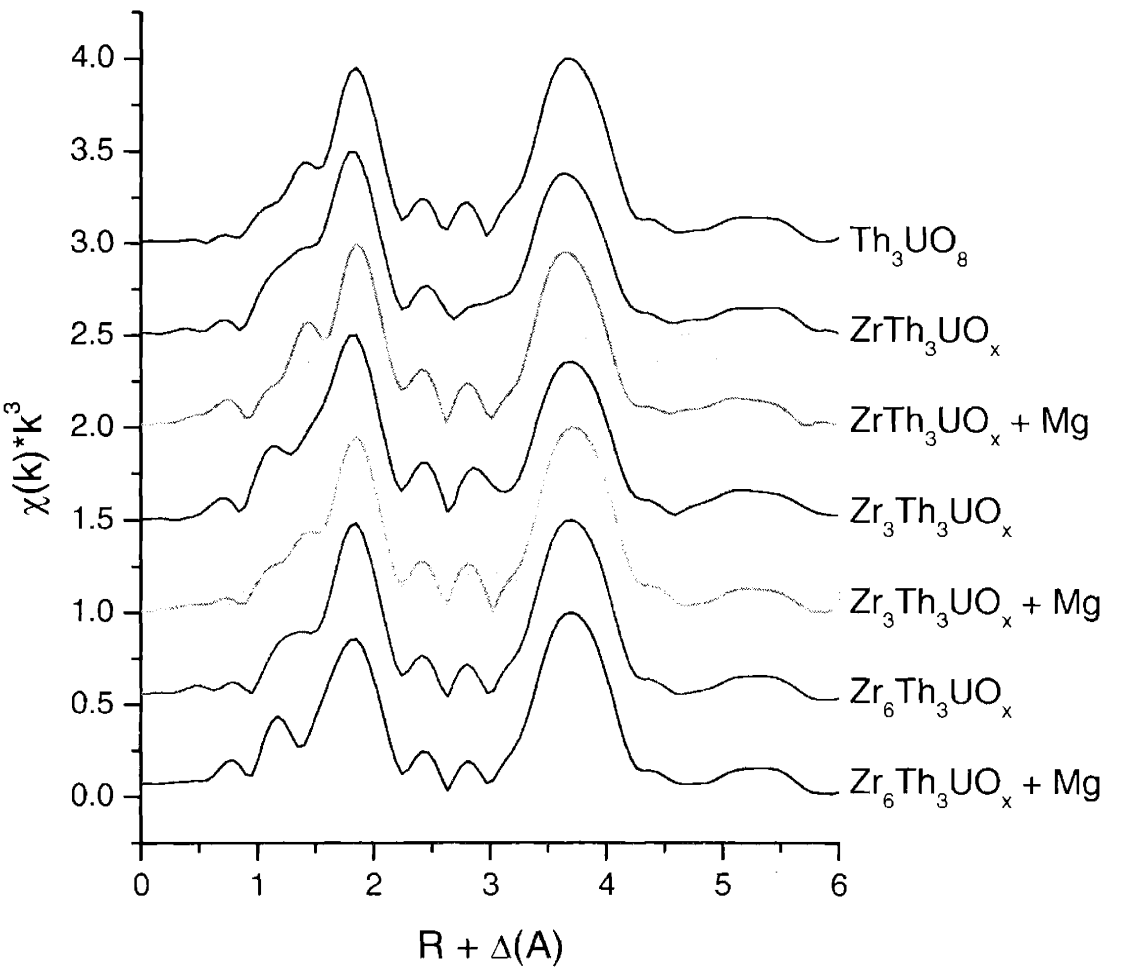

Figure 6.7. Thorium EXAFS fourier transforms

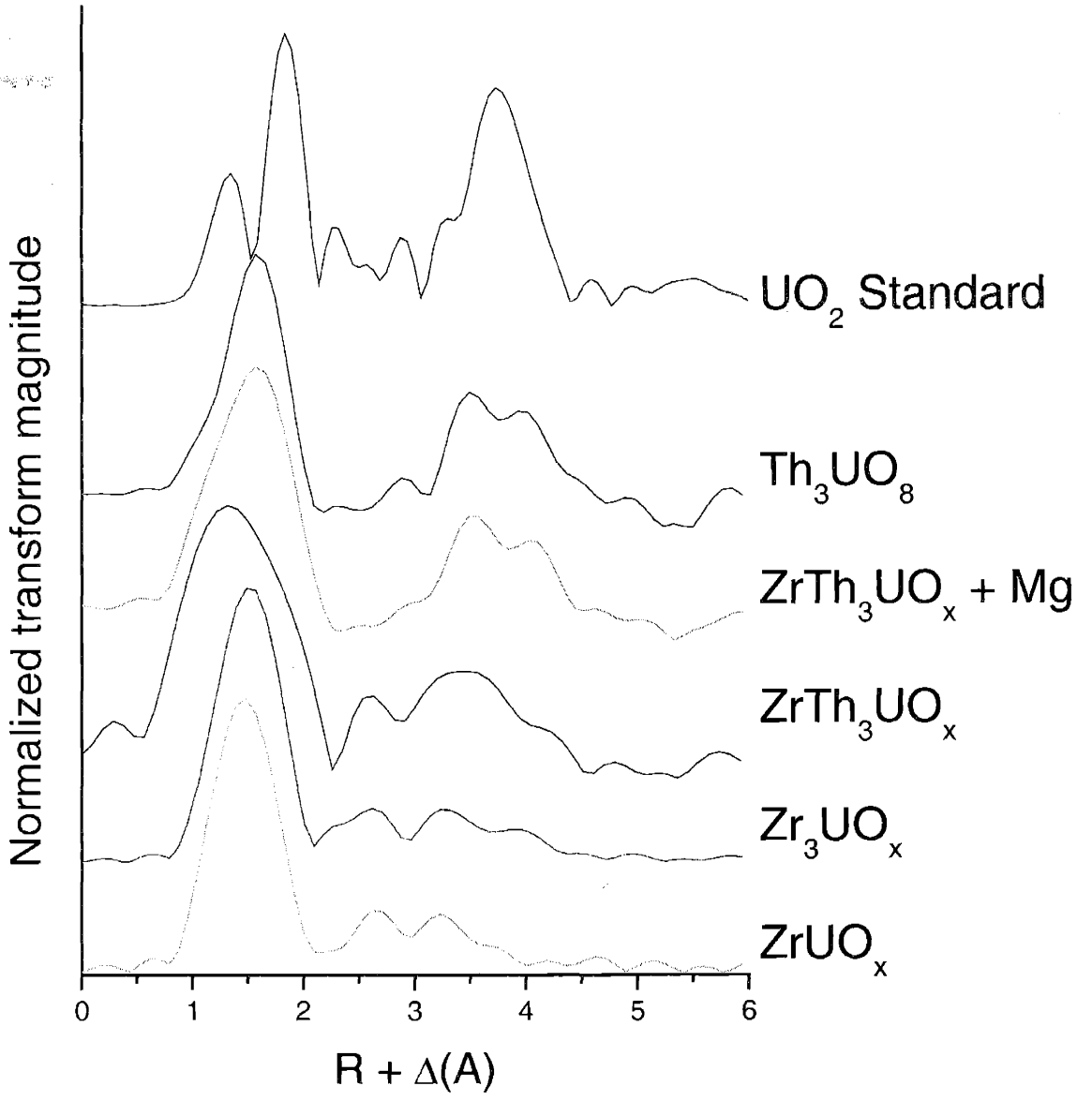

Figure 6.8. Uranium EXAFS Fourier transforms

Sample	Bond	N	R(Å)
Zr	Zr-M	12	3.71
Zr + Mg	Zr-M	12	3.61
Zr_3	Zr-M	12	3.56
Zr_3 + Mg	Zr-M	12	3.57
Zr_6	Zr-M	12	3.51
Zr_6 + Mg	Zr-M	12	3.48
ZrU	Zr-M	12	3.50
Zr_3U	Zr-M	12	3.50

Table 6.5 Zr-M bond lengths. The contraction in the bond lengths shows the decreasing amounts of U incorporated.

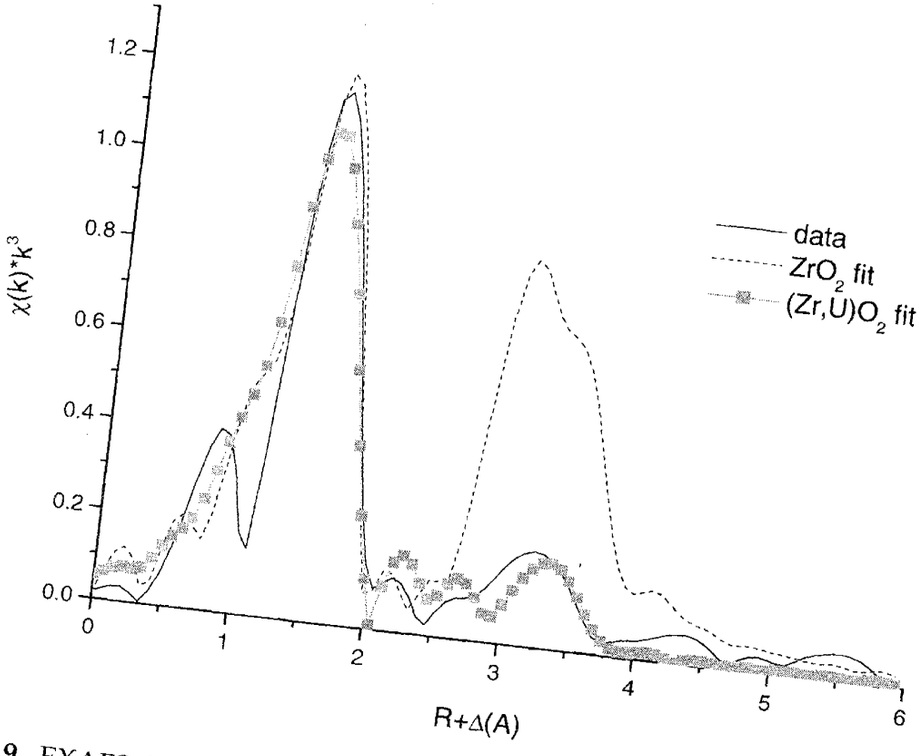

Figure 6.9. EXAFS data fit for ceramics with a metal ratio of $ZrTh_3U$

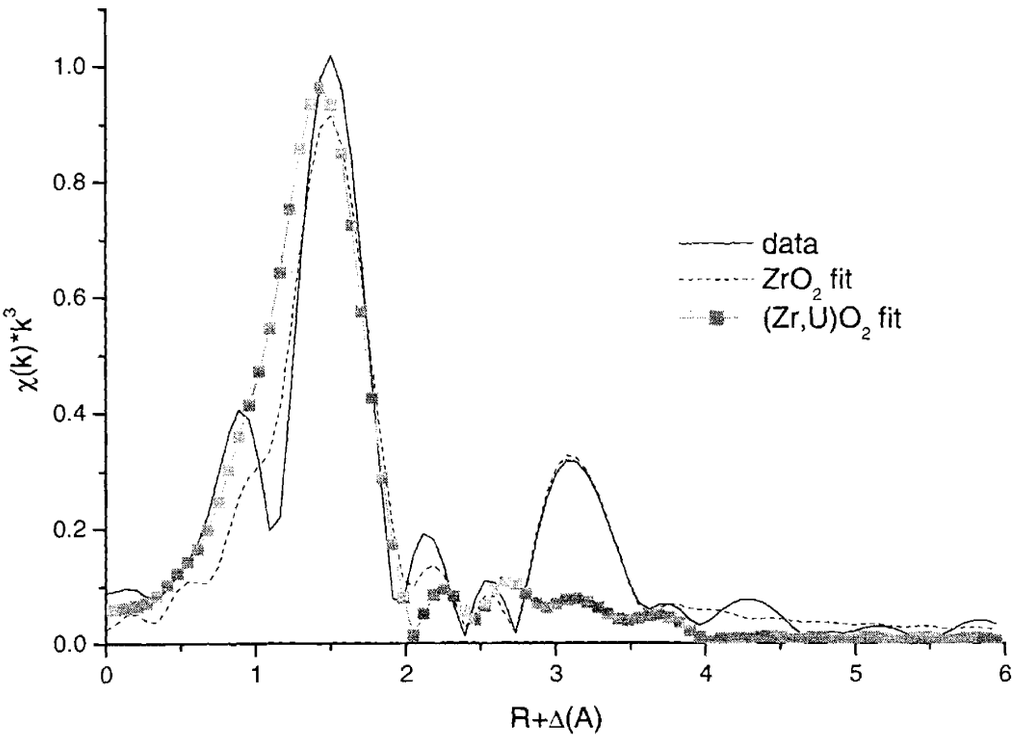

Figure 6.10. EXAFS data fit for ceramics with a metal ratio of $ZrTh_3U$ + 5 wt% MgO

6.6 Conclusions

The mutual affinities in ZrO_2-ThO_2-UO_2 systems are very similar to the ones observed in binary systems. Uranium, which has a good affinity with both Th and Zr is homogenously distributed throughout the ceramics, whereas Th and Zr form separate phases. Magnesium oxide, which is also soluble in both phases, increases the density of the material. The presence of Zr lead to an oxidation of the U in the Zr rich phase while the Th helped stabilize the tetravalent form of U under the atmospheric conditions used in the sintering. This can be attributed to the strong chemical and physical similarity of tetravalent U with Th when compared to Zr. The actinides have similar electronic structures and ionic radii.

The EELS results show the method can be applied to the actinides, similar to previous investigations with the lanthanides. Extrapolating from the rare-earth chemistry and the previous results [17], we can assume that the M_4/M_5 ratio for 5f elements decreases with increasing 5f orbital occupancy, which is to say with decreasing oxidation state. For the actinides a large relative error in the M_4/M_5 ratio is expected. Since the energy of the 5f, 6d, 7s and 7p orbitals are comparable, there is considerable flexibility in electron configurations for a given oxidation state. However, a trend is confirmed by the M_4/M_5 analysis of U_3O_8 (U oxidation state = 5.3) and UO_2 (U oxidation state = 4) reference samples and is used to qualitatively assess the oxidation state of U in the different phases of the ceramic samples with results confirmed by other spectroscopic techniques.

6.7 Acknowledgements

The XRD and electron microscopy work was carried out at the Center for Materials Science and Engineering at M.I.T. We thank Gordon Kohse, Prof. Linn Hobbs and Michael Frongillo for advice and help with sample preparation and Dr. Garratt-Reed for help with EDX analysis and EELS data collection. Part of this work was performed under the auspices of the U.S. Department of Energy (DOE) by the University of California Lawrence Livermore National Laboratory under Contract No. W-7405-Eng-48. This work was done (partially) at SSRL, which is operated by the Department of Energy, Division of Chemical Sciences.

6.8 References

1. Kazimi, Mujid et al. Advanced Proliferation Resistant, Lower cost, Uranium-Thorium Dioxide Fuels for Light Water Reactors, Nuclear Energy Research Initiative Project 99-0153 Quarterly Report, May 2000
2. Gong, W.L.; Lutze, W.; Ewing, R.C. Zirconia ceramics for excess weapons plutonium waste, J. Nucl. Mat. 277, (2000), 239-249
3. Benedict, Manson; Pigford, T.H.; Levi, H.V. Nuclear Chemical Engineering 2nd Edition. 1981 McGraw-Hill 318-321
4. Crawford, C.L.; Biddle, C.R.; Bibler, N.E. Durability testing of heavy-ion irradiated crystalline ceramics. Report, WSRC-MS-2000-00309

   http://www.srs.gov/general/sci-tech/fulltext/ms2000309/ms2000309.html
5. De Lima, N.B. and Imakuma, K.: X-Ray Diffraction Study Of The Formation Of Solid Solutions In Urania-Thoria Prepared By Aqueous Chemical Processes. J. Nucl. Mat., **135**, 215-221 (1985).
6. Balek, V.: Application of Emanation Thermal Analysis for Characterization of Intermediate Products of Urania and Thoria Ceramics. J. Nucl. Mat., **153**, 41-49 (1988).
7. Anderson,E.B, Burakov,E.B, Vasiliev,V.G. (1993) A Creation of Crystalline Matrix for Actinide Waste in Khlopin Radium Institute. *Proceedings of International Conference SAFE WASTE-93, 13-18/06/1993, Avignon, France,* Vol.2, 29-33.
8. Kuramoto,K-I, Makino,Y, Yanagi,T, Muraoka,S, Ito,Y. (1995) Development of Zirconia- and Alumina-Based Ceramic Waste Forms for High Concentrated TRU Elements. *Proceedings of the International Conference Global-95, Versailles, France, 11-14/09/1995,* Vol.2, 1838-1845.
9. Kinoshita,H., Kuramoto,K., Uno,M., Yamanaka,S. Mitamura,H., Banba,T. (1998) Phase Stability and Mechanical Property of Yttria-Stabilized Zirconia Form for Partitioned TRU Wastes. *Proceedings of the 2nd NUCEF International Symposium NUCEF'98, 16-17/11/98, Hitachinaka, Ibaraki, Japan, JAERI-Conf.99-004 (Part I), 307-326.*
10. Burakov,B.E, Anderson,E.B. (1998) Development of Crystalline Ceramic for Immobilization of TRU Wastes in V.G.Khlopin Radium Institute. *Proceedings of the 2nd NUCEF International Symposium NUCEF'98, 16-17/11/98, Hitachinaka, Ibaraki, Japan, JAERI-Conf.99-004 (Part I), 295-306.*
11. Burakov, B.E, Anderson, E.B. (2000) in Excess Weapons Plutonium Immobilization in Russia eds. L.J. Jardine, G.B. Borisov, UCRL-ID-138361,

Proceedings of the Meeting for Coordination and Review of Work, Held in St. Petersburg, Russia, November 1-4/1999, 167-179.

12. B. Burakov, E. Anderson, in Immobilization of Excess Weapons Plutonium in Russia: A Review of LLNL Contract Work, ed. L.J. Jardine, G.B. Borisov, *Proc. Meet. for Coordination and Review of Work*, St. Petersburg, Russia, 13-16/11/2000, UCRL-ID-143846, 229-234 (2001).

13. F.A. Mumpton, R. Rustum, J. Am. Ceram. Soc. 43 (1960) 237.

14. J.Cohen, B.E. Schaner, J. Nucl. Mater. 9 (1963) 18.

15. G. Curran, W. Rattray, and K.R. Czerwinski: Solubility of Thorium from Th_3UO_8 and $ZrTh_3UO_{10}$ Ceramics. Radiochimica Acta, 91 (2003) 201.

16. E.C. Buck, J.A. Fortner, Ultramicroscopy 67 (1997) 69.

17. B.T. Hole, G. Van der Laan, J.C. Fuggle, G.A. Swatzky, R.C. Karnatak and J-M. Esteva, Phys. Rev. B 32 (1985) 5107.

18. J.A. Fortner and E.C. Buck, Appl. Phys. Lett. 68 (1996) 3817.

19. P.W. Atkins, Eur. J. Sol. State Inorg. Chem. 28 (1991)

20. T.M. Hayes, J.B. Boyce, Solid State Physics 37 (1982) 173.

21. G.G. Li, F. Bridges, C.H. Booth, Phys. Rev. B 52 (1995) 6332.

22. M. Newville, P. Livins, Y. yacoby, J.J. Rehr, E.A. Stern, Phys. Rev. B 47 (1993) 4126

23. J.J. Rehr, J. Mustre de Leon, SI. Zabinsky, R.C. Abers, J. Amer. Chem. Soc. 113 (1991) 5135

24. J.J. Rehr, J. Mustre de Leon, SI. Zabinsky, R.C. Abers, Phys. Rev. B 44 (1991) 4146

Solubility of Thorium from Th_3UO_8 and $ZrTh_3UO_{10}$ Ceramics

6.9 Abstract

The solubility of thorium from Th_3UO_8 and $ZrTh_3UO_{10}$ ceramics was studied to evaluate the solubility constants for the materials. Zirconium was added in order to investigate potential additional stabilization of the thorium matrix from ZrO_2. Studies were performed from pH 4 to pH 9 under both 100% Argon and 10% CO_2/90% Ar at 25 °C in 0.1 M $NaClO_4$. Reaction kinetics and equilibrium concentrations were evaluated for each condition. Rate constants increased with pH and varied from $6x10^{-4}$ hr^{-1} to $4x10^{-2}$ hr^{-1}. The surface area normalized dissolution rate decreased with increasing pH, the highest being $5x10^{-7}$ $gm^{-2}d^{-1}$ at pH 4. The solubility product constants calculated from the equilibrium concentrations for the two ceramics were equivalent, with $K_{spTh3UO8}$= -48.3±0.4 and $K_{spZrTh3UO8}$= -47.9±0.9. The data was used to calculate the Th solution phase concentration. The result was compared to the dissolution of UO_2 from pH 5-9 in 0.1 M $NaClO_4$ under a 1% CO_2 atmosphere at 25 °C. It was found that the U from the UO_2 had a higher solution phase concentration than Th at high pH and was highly dependent upon the solution Eh of the evaluated conditions.

6.10 Introduction

There has been a recent resurgence of interest in thorium fueled reactors as a potential advanced fuel for Generation IV nuclear energy systems that can be operated to relatively high burnups. In addition, it is thought that ThO_2-UO_2 fuels will be less expensive to fabricate than UO_2 fuel, allow higher sustainable plant capacity factors, result in a more stable and insoluble waste, and produce less plutonium [1].

Few dissolution studies of the actual thorium uranium oxide ceramic that would be the basis of such fuel have been performed. The data can be used to evaluate the expected waste form behavior of Th fuels and compare the results to standard UO_2 fuel. The redox conditions of ThO_2 are expected to yield favorable waste form behavior when compared to UO_2 under oxidizing conditions. The inclusion of Zr in the ceramic is chosen since ZrO_2 chemically stable, radiation resistant [2], and has a very low thermal neutron capture cross section. The natural analogue of zirconia, baddeleyite ($(Zr,M)O_2$), where M is a tetravalent ion such as hafnium), contains up to 3 000 ppm uranium or thorium [3]. Negligible or no lead loss (a stable decay product of uranium and thorium) in natural baddeleyites indicates high, long term, chemical durability of the material in the environment [2]. This work will determine if the enhanced chemical stability from ZrO_2 is included in the ceramics containing Zr.

There has been previous work on the fabrication and characterization of UO_2-ThO_2 ceramics [4,5]. Various zirconia containing ceramics have been fabricated and studied, including ZrO_2-PuO_2, ZrO_2-UO_2, ZrO_2-ThO_2, and ZrO_2-CeO_2 [2]. The solubility of the thorium ceramics, which would be the waste form for directly disposed spent fuel, have not yet been studied in a manner to provide thermodynamic data necessary for geochemical modeling.

This study measures the Th solubility of the synthesized Th_3UO_8 and $ZrTh_3UO_{10}$ ceramics to provide data for incorporation into thermodynamic models. This is motivated by the large variation of solubility constants for ThO_2 in the literature [6-10] and defining which, if any, would be suitable for evaluation any future fuel based on Th-U solid solution. The experiments are performed from pH 4 to pH 9 under 100% Ar and 10% CO_2/90% Ar atmospheres at 25 °C in 0.1 M $NaClO_4$ solution. The conditions are chosen to produce thermodynamic data for comparison with existing data and provide data for inclusion into models for assessing speciation under a variety of conditions. Perchlorate is used as a non-competition cation and as a means to fix the ionic strength [10]. A correlation of the resulting constant with ionic strength can be made using the specific ion interaction theory (SIT) [11]. The SIT model describes the activity coefficient with a long range Debye-Hückel term and a short range specific ion interaction term. Results on the characterization of the ceramics are briefly presented and are given in more detail in other work [12]. The total mass and surface area of the examined ceramics are given and used to determine surface area normalized mass loss. The dissolution rate constants under the experimental conditions are provided. The equilibrium Th solution concentrations are used to determine the solubility constant for the Th in the ceramics. The solubility data is used to calculate the solution Th concentrations resulting from the ceramics under oxidizing, slightly carbonate conditions.

6.11 Experimental methods

6.11.1 Materials and Supplies

The metal salts $UO_2(NO_3)_2{\cdot}6H_2O$, $Th(NO_3)_4{\cdot}4H_2O$, and $ZrOCl_2{\cdot}8H_2O$ were supplied by Alfa Aesar. All other chemicals, buffers, and ICP-MS standards were supplied by Aldrich.

6.11.2 Ceramic Fabrication

All of the ceramic forms fabricated in this study have a Th:U ratio of 3:1 which was determined in previous work based on reactor physics. The Zr containing ceramic has a ratio of Zr:Th:U of 1:3:1. The low amount of Zr is selected to minimize the reduction of fissile and fertile elements. To prepare the ceramics, stoichiometric quantities of the metal salts were dissolved in water and then slowly mixed with a solution of oxalic acid and excess ammonium hydroxide so that a gelatinous precipitate formed. This precipitate was allowed to settle and the supernatant liquid was removed. The precipitate was washed twice with water, twice with acetone and placed in an oven at 80°C to dry overnight. The resulting precipitate is milled, dried, and calcined in air at 750°C for one hour. The powder is then cooled and cold pressed into 5 mm diameter pellets for two minutes using a hydraulic press at 55 MPa. The pellets are sintered in a Thermolyne 46100 high temperature furnace at 1500°C for four hours. An argon atmosphere with 4% hydrogen is used for sintering to avoid the oxidation of uranium. The ceramic surface area is determined by BET with a Quantachrome Nova 1000 using N_2.

6.11.3 *Dissolution Experiments*

Dissolution experiments were conducted in 0.1 M $NaClO_4$ under 100% argon or 90% argon/10% CO_2. Experiments were performed with the assistance of Wendy Rattray, SM '01. Gases are industrial grade, 99.96% purity supplied by BOC gases. For each experiment, 100 mL of 0.1M $NaClO_4$ is added to a round bottomed, three-necked flask. Under argon, solubility was studied at pH 4, 7, and 10 while under 10% CO_2 experiments were performed at pH 4, 5.25, and 6.25. The pH of the flask was adjusted by adding of $HClO_4$ or NaOH while the flask is purged with the appropriate atmosphere. Once the pH stabilized, a ceramic pellet with a 0.5 cm diameter and a mass near 0.2 g was added to the flask. A 4.5 mL sample was collected and passed through a 0.2 μm filters every 3-7 days. Unfiltered samples were also analyzed to evaluate colloid formation. Samples were acidified to 0.3 M HNO_3 prior to analysis. Inductively Coupled Plasma–Mass Spectroscopy (ICP-MS) performed with a Fisons ICP20P was used to determine the solution Th concentration in the collected samples. The Th detection limit on the instrument was measured to be 1×10^{-11} M. Calibration standards were prepared in a 0.3 M HNO_3 matrix identical to that of the samples. Errors in the Th solution phase concentration values were from the standard deviation of triplicate measurements. All values for the correlation coefficient from the data analysis were greater than 0.90 and were performed with the program KaleidaGraph 3.5. The standard error from the data analysis using KaleidaGraph 3.5 is the standard deviation divided by the square root of the number of data points.

6.11.4 *Modeling*

The dissolution of the Th_3UZrO_{10} ceramic material and UO_2 was calculated from pH 4-9 with a 1% CO_2 atmosphere in 0.1 M $NaClO_4$ at 25 °C. Since the dissolution of UO_2 is highly sensitive to redox conditions, Eh values of –200 mV, 0 mV, and 200 mV were examined. The equilibrium solution phase concentrations of Th and U are evaluated. The determined K_{sp} for this work and literature data was used to evaluate the Th_3UZrO_{10} material. The geochemical code CHESS (CHemical Equilibrium and Speciation with Surfaces) was used to evaluate UO_2 dissolution using the CHEMVAL database. CHESS is a robust model for examining speciation of actinides and auxiliary species in complex, multi-phase solutions. The main database for CHESS is from the literature [13,14].

6.12 Results and Discussion

6.12.1 *Ceramic Data*

The masses and surface areas of the ceramic samples used in the dissolution experiments are given below (Table 6.6). The surface area data was used to normalize Th dissolution. These results showed that the inclusion of Zr formed two distinct phases, a Th rich phase and a Zr rich phase. Uranium was equally distributed between the two phases. The ceramic without Zr formed a solid solution of Th and U.

Ceramic	pH	CO_2 Partial Pressure	mass (g)	Surface Area (m^2g^{-1})
Th_3UO_8	4.1	0	0.2478	1.18±0.02
Th_3UO_8	7.0	0	0.2400	1.32±0.06
Th_3UO_8	9.4	0	0.2254	1.30±0.03
Th_3UO_8	4.2	0.1	0.2017	1.19±0.04
Th_3UO_8	5.2	0.1	0.2559	1.18±0.05
Th_3UO_8	6.2	0.1	0.2035	1.19±0.04
$ZrTh_3UO_{10}$	4.6	0	0.2795	1.30±0.04
$ZrTh_3UO_{10}$	7.3	0	0.2139	1.24±0.04
$ZrTh_3UO_{10}$	9.1	0	0.2490	1.32±0.06
$ZrTh_3UO_{10}$	4.1	0.1	0.2743	1.23±0.05
$ZrTh_3UO_{10}$	5.3	0.1	0.2748	1.29±0.03
$ZrTh_3UO_{10}$	6.3	0.1	0.2309	1.27±0.04

Table 6.6. Mass and surface area of examined ceramics

6.12.2 Dissolution Kinetics

Kinetics analyses were performed in order to determine dissolution rate constants, surface area mass normalized dissolution, and solution equilibrium conditions. The Th solution concentration for the examined ceramics under the different experimental conditions as a function of time is presented below (Figures 6.11-6.12, Tables 6.7-6.10). The influence of carbonate is minimal under the conditions examined. Not surprisingly, pH is the largest influence on the dissolution of Th. The lower pH range examined has the largest Th solution concentration.

time (hr)	pH 4.1	pH 7.0	pH 9.4
81.2	$2.80\pm0.14\times10^{-8}$	$4.69\pm0.24\times10^{-10}$	$2.85\pm0.29\times10^{-10}$
160.2	$4.55\pm0.27\times10^{-8}$	$4.93\pm0.35\times10^{-10}$	$3.08\pm0.24\times10^{-10}$
243.1	$6.43\pm0.27\times10^{-8}$	$5.98\pm0.54\times10^{-10}$	$2.90\pm0.12\times10^{-10}$
323.2	$9.65\pm0.27\times10^{-8}$	$5.83\pm0.24\times10^{-10}$	$2.95\pm0.18\times10^{-10}$
408.8	$1.11\pm0.06\times10^{-7}$	$5.35\pm0.22\times10^{-10}$	$3.01\pm0.21\times10^{-10}$
490.4	$1.15\pm0.05\times10^{-7}$	$5.29\pm0.46\times10^{-10}$	$3.24\pm0.33\times10^{-10}$
574.7	$1.43\pm0.04\times10^{-7}$	$5.52\pm0.52\times10^{-10}$	$2.86\pm0.22\times10^{-10}$
652.8	$1.29\pm0.08\times10^{-7}$	$5.25\pm0.41\times10^{-10}$	$3.05\pm0.20\times10^{-10}$
737.8	$1.62\pm0.10\times10^{-7}$	$5.84\pm0.29\times10^{-10}$	$2.91\pm0.21\times10^{-10}$
818.2	$1.71\pm0.07\times10^{-7}$	$4.99\pm0.22\times10^{-10}$	$3.08\pm0.26\times10^{-10}$
897.1	$1.83\pm0.08\times10^{-7}$	$6.00\pm0.54\times10^{-10}$	$2.85\pm0.17\times10^{-10}$
976.6	$1.89\pm0.06\times10^{-7}$	$4.82\pm0.36\times10^{-10}$	$3.24\pm0.16\times10^{-10}$
1061.2	$2.02\pm0.09\times10^{-7}$	$5.62\pm0.43\times10^{-10}$	$3.03\pm0.29\times10^{-10}$
1143.0	$1.73\pm0.06\times10^{-7}$	$5.25\pm0.53\times10^{-10}$	$3.12\pm0.26\times10^{-10}$
1223.5	$2.10\pm0.09\times10^{-7}$	$5.60\pm0.33\times10^{-10}$	$2.86\pm0.19\times10^{-10}$
1303.2	$2.11\pm0.13\times10^{-7}$	$5.79\pm0.49\times10^{-10}$	$2.93\pm0.12\times10^{-10}$

Table 6.7. Th solution concentration (mol/L) as a function of time from the dissolution of Th_3UO_8 under Ar at pH 4.1, 7.0, and 9.4

time (hr)	pH 4.2	pH 5.2	pH 6.2
89.2	$2.27\pm0.07\times10^{-8}$	$3.20\pm0.14\times10^{-9}$	$4.30\pm0.35\times10^{-9}$
181.8	$4.41\pm0.12\times10^{-8}$	$4.71\pm0.39\times10^{-9}$	$5.40\pm0.35\times10^{-9}$
266.6	$6.83\pm0.24\times10^{-8}$	$4.97\pm0.40\times10^{-9}$	$5.94\pm0.62\times10^{-9}$
356.3	$8.62\pm0.35\times10^{-8}$	$5.08\pm0.46\times10^{-9}$	$6.85\pm0.33\times10^{-9}$
443.0	$9.53\pm0.24\times10^{-8}$	$5.70\pm0.27\times10^{-9}$	$6.84\pm0.70\times10^{-9}$
538.0	$1.11\pm0.04\times10^{-7}$	$5.41\pm0.23\times10^{-9}$	$6.62\pm0.55\times10^{-9}$
624.9	$1.30\pm0.08\times10^{-7}$	$5.19\pm0.26\times10^{-9}$	$6.79\pm0.66\times10^{-9}$
716.0	$1.52\pm0.05\times10^{-7}$	$5.40\pm0.43\times10^{-9}$	$6.58\pm0.33\times10^{-9}$
805.1	$1.58\pm0.10\times10^{-7}$	$5.26\pm0.50\times10^{-9}$	$7.05\pm0.38\times10^{-9}$
883.8	$1.76\pm0.10\times10^{-7}$	$5.20\pm0.53\times10^{-9}$	$6.87\pm0.37\times10^{-9}$
971.8	$1.83\pm0.06\times10^{-7}$	$5.83\pm0.36\times10^{-9}$	$6.34\pm0.35\times10^{-9}$
1065.6	$1.78\pm0.05\times10^{-7}$	$5.85\pm0.50\times10^{-9}$	$6.86\pm0.61\times10^{-9}$
1148.7	$1.89\pm0.10\times10^{-7}$	$5.45\pm0.32\times10^{-9}$	$7.05\pm0.60\times10^{-9}$

Table 6.8. Th solution concentration (mol/L) as a function of time from the dissolution of Th_3UO_8 under 10% CO_2 at pH 4.2, 5.2, and 6.2

time (hr)	pH 4.6	pH 7.3	pH 9.1
94.9	$2.54\pm0.10\times10^{-8}$	$8.03\pm0.50\times10^{-10}$	$2.63\pm0.16\times10^{-9}$
204.2	$5.36\pm0.25\times10^{-8}$	$1.75\pm0.12\times10^{-9}$	$3.14\pm0.25\times10^{-9}$
302.7	$7.53\pm0.43\times10^{-8}$	$2.36\pm0.16\times10^{-9}$	$3.03\pm0.28\times10^{-9}$
405.8	$9.00\pm0.33\times10^{-8}$	$2.84\pm0.26\times10^{-9}$	$3.35\pm0.29\times10^{-9}$
507.1	$1.10\pm0.05\times10^{-7}$	$3.46\pm0.35\times10^{-9}$	$3.00\pm0.20\times10^{-9}$
601.8	$1.39\pm0.04\times10^{-7}$	$4.20\pm0.32\times10^{-9}$	$2.98\pm0.13\times10^{-9}$
701.6	$1.39\pm0.05\times10^{-7}$	$4.53\pm0.43\times10^{-9}$	$2.99\pm0.20\times10^{-9}$
801.9	$1.56\pm0.05\times10^{-7}$	$4.50\pm0.22\times10^{-9}$	$3.48\pm0.28\times10^{-9}$
905.2	$1.82\pm0.11\times10^{-7}$	$5.08\pm0.37\times10^{-9}$	$3.41\pm0.20\times10^{-9}$
1005.5	$2.02\pm0.12\times10^{-7}$	$5.39\pm0.47\times10^{-9}$	$3.20\pm0.31\times10^{-9}$
1106.7	$2.08\pm0.10\times10^{-7}$	$6.08\pm0.26\times10^{-9}$	$3.24\pm0.22\times10^{-9}$
1212.9	$2.37\pm0.14\times10^{-7}$	$6.28\pm0.45\times10^{-9}$	$3.51\pm0.29\times10^{-9}$

Table 6.9. Th solution concentration (mol/L) as a function of time from the dissolution of $ZrTh_3UO_{10}$ under Ar at pH 4.6, 7.3, and 9.1

time (hrs)	pH 4.1	pH 5.3	pH 6.3
73.3	$2.72\pm0.11\times10^{-8}$	$1.36\pm0.10\times10^{-9}$	$4.12\pm0.17\times10^{-9}$
149.1	$5.51\pm0.25\times10^{-8}$	$1.54\pm0.07\times10^{-9}$	$6.57\pm0.61\times10^{-9}$
223.5	$7.79\pm0.37\times10^{-8}$	$1.71\pm0.18\times10^{-9}$	$7.69\pm0.34\times10^{-9}$
300.5	$1.08\pm0.06\times10^{-7}$	$1.58\pm0.09\times10^{-9}$	$8.47\pm0.59\times10^{-9}$
374.8	$1.23\pm0.06\times10^{-7}$	$1.61\pm0.08\times10^{-9}$	$8.34\pm0.70\times10^{-9}$
446.5	$1.45\pm0.04\times10^{-7}$	$1.85\pm0.14\times10^{-9}$	$8.06\pm0.50\times10^{-9}$
523.5	$1.60\pm0.09\times10^{-7}$	$1.55\pm0.12\times10^{-9}$	$8.01\pm0.35\times10^{-9}$
595.1	$1.93\pm0.06\times10^{-7}$	$1.78\pm0.14\times10^{-9}$	$8.64\pm0.75\times10^{-9}$
667.3	$1.94\pm0.10\times10^{-7}$	$1.76\pm0.07\times10^{-9}$	$8.46\pm0.74\times10^{-9}$
743.4	$2.22\pm0.06\times10^{-7}$	$1.77\pm0.15\times10^{-9}$	$8.24\pm0.59\times10^{-9}$
818.1	$2.37\pm0.10\times10^{-7}$	$1.55\pm0.13\times10^{-9}$	$9.07\pm0.90\times10^{-9}$
891.6	$2.50\pm0.12\times10^{-7}$	$1.69\pm0.09\times10^{-9}$	$8.03\pm0.46\times10^{-9}$
967.9	$2.61\pm0.13\times10^{-7}$	$1.73\pm0.16\times10^{-9}$	$8.80\pm0.66\times10^{-9}$

Table 6.10. Th solution concentration (mol/L) as a function of time from the dissolution of $ZrTh_3UO_{10}$ under 10% CO_2 at pH 4.1, 5.3, and 6.3

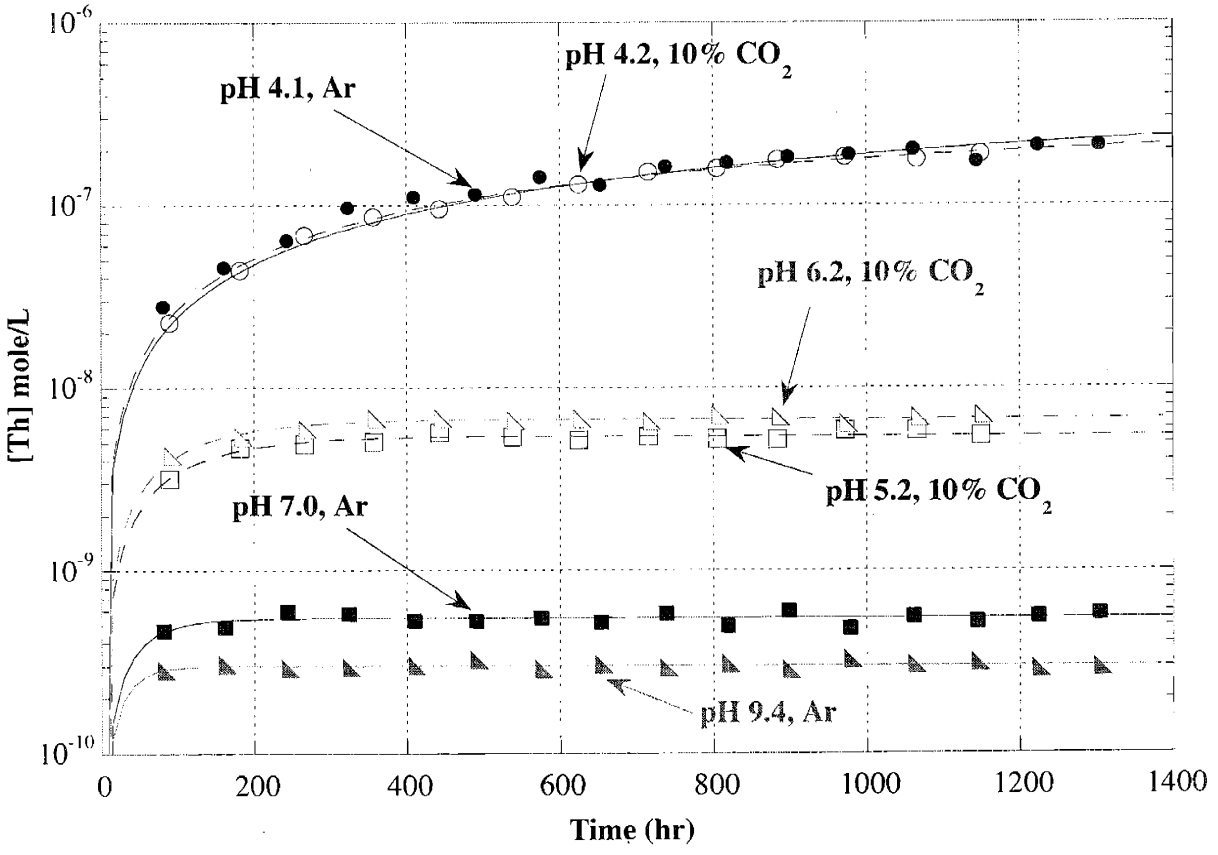

Figure 6.11. Th solution concentration (mol/L) for the dissolution of Th_3UO_8

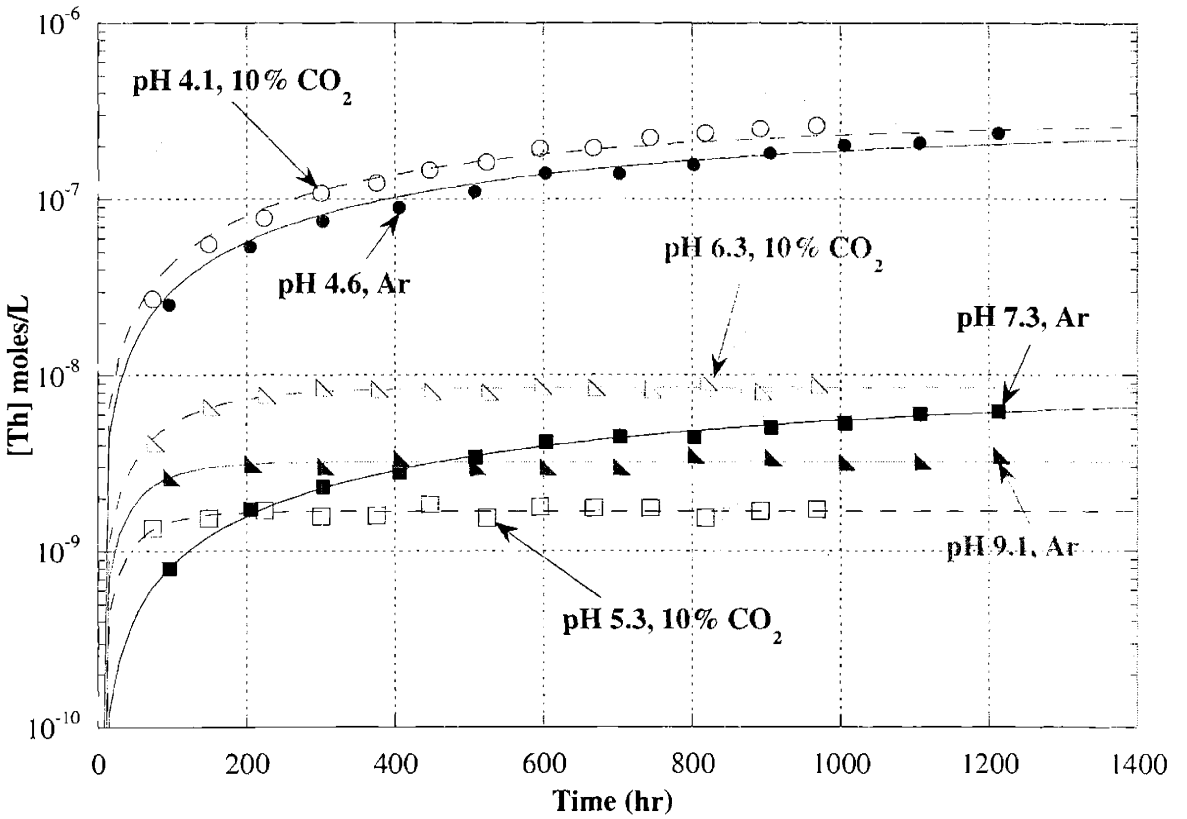

Figure 6.12. Th solution concentration (mol/L) for the dissolution of $ZrTh_3UO_{10}$

Figures 6.11 and 6.12 show equilibrium is not reached for the Th concentration at pH 4, in contrast to experiments performed at higher pH. For all data sets the change in Th concentration with time can be fit to a 1st order rate constant using the equation:

$$[Th]_t = [Th]_{eq}(1 - e^{-kt}) \qquad \textbf{Eq. 6.1}$$

where $[Th]_t$ is the Th solution concentration at time t, $[Th]_{eq}$ is the Th solution concentration at equilibrium, and k is the rate constant. This analysis permits a comparison of dissolution kinetic rates and equilibrium concentrations. The evaluated equilibrium concentrations are given below (Table 6.11) and used to evaluate the Th solubility constant for the ceramics (see section 6.11.3).

	Th_3UO_8		$ZrTh_3UO_{10}$	
pH	Ar	10% CO_2	Ar	10% CO_2
4.1	$4.24\pm1.23\times10^{-7}$			$2.85\pm0.41\times10^{-7}$
4.2		$2.86\pm0.24\times10^{-7}$		
4.6			$2.67\pm0.39\times10^{-7}$	
5.2		$5.48\pm0.26\times10^{-9}$		
5.3				$1.71\pm0.11\times10^{-9}$
6.2		$6.78\pm0.23\times10^{-9}$		
6.3				$8.41\pm0.40\times10^{-9}$
7.0	$5.44\pm0.35\times10^{-10}$			
7.3			$8.79\pm0.69\times10^{-9}$	
9.1			$3.24\pm0.21\times10^{-9}$	
9.4	$3.02\pm0.14\times10^{-10}$			

Table 6.11. Th equilibrium concentration ($[Th]_{eq}$) in mol/L from the dissolution of Th_3UO_8 and $ZrTh_3UO_{10}$

The rate constants for the Th dissolution are presented below based on data from Figures 6.11 and 6.12 (Table 6.12). The general observed trend is an increase in the rate constant with increasing pH (Figure 6.13). The results support the formation of the hydroxide species prior to dissolution [10]. The trend can also be explained from the equilibrium data. The higher Th solution equilibrium concentration found at pH 4 requires more time to be reached, hence a lower rate constants. The lower Th solution concentration found at higher pH is quickly reached under the experimental conditions.

	Th_3UO_8		$ZrTh_3UO_{10}$	
pH	Ar	10% CO_2	Ar	10% CO_2
4.1	$5.93\pm0.23\times10^{-4}$			$1.65\pm0.43\times10^{-3}$
4.2		$9.84\pm1.28\times10^{-4}$		
4.6			$1.21\pm0.31\times10^{-3}$	
5.2		$9.99\pm0.97\times10^{-3}$		
5.3				$2.11\pm0.38\times10^{-2}$
6.2		$9.93\pm0.86\times10^{-3}$		
6.3				$9.83\pm0.80\times10^{-3}$
7.0	$2.24\pm0.51\times10^{-2}$			
7.3			$9.97\pm1.23\times10^{-4}$	
9.1			$1.76\pm0.35\times10^{-2}$	
9.4	$3.66\pm1.06\times10^{-2}$			

Table 6.12. Kinetic rate constants (k in hr^{-1}) for the dissolution of Th from Th_3UO_8 and $ZrTh_3UO_{10}$ at various pH under Ar and 10% CO_2

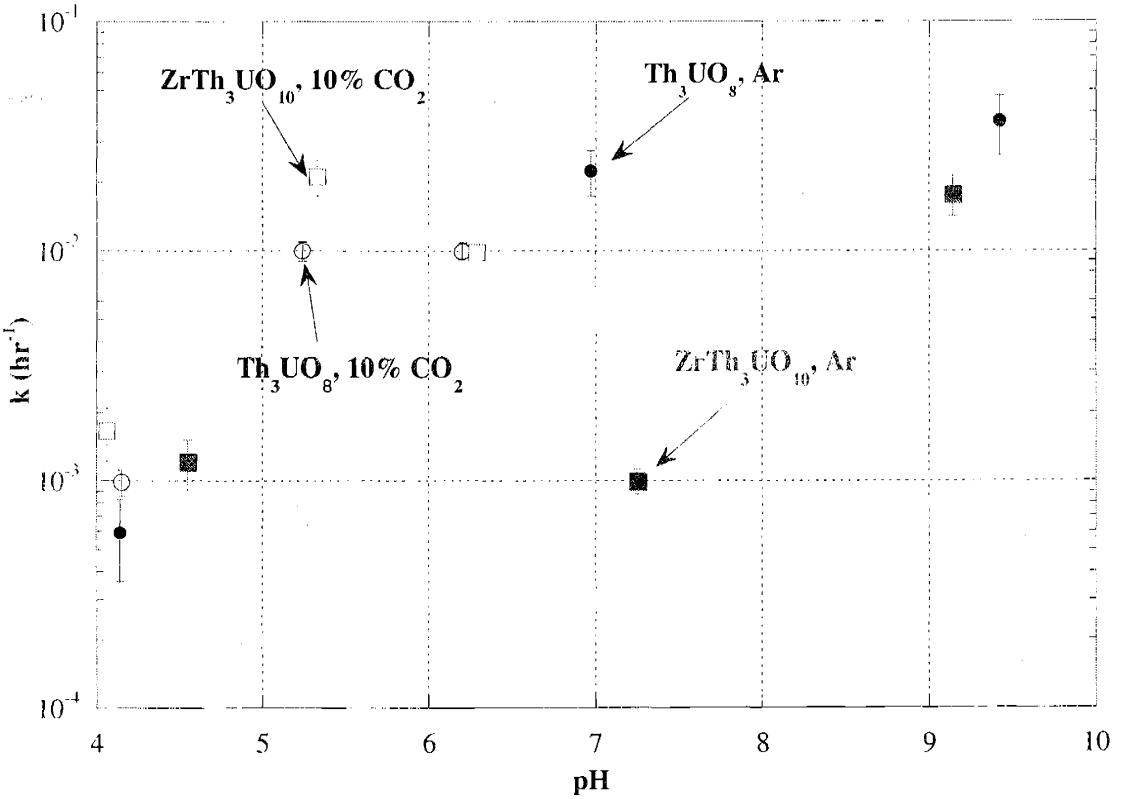

Figure 6.13. Rate constant k (hr^{-1}) for the dissolution of Th from Th_3UO_8 and $ZrTh_3UO_{10}$

Another method for comparison of Th dissolution from the ceramics is to normalize the results to ceramic surface area. The normalized Th mass loss (N_{lTh}) is found from

$$N_{lTh} = \frac{m_{Thsol}}{f_{ThO_2} m_c SA_c} \qquad \textbf{Eq. 6.2}$$

	Th_3UO_8		$ZrTh_3UO_{10}$	
pH	Ar	10% CO_2	Ar	10% CO_2
4.1	$3.66\pm0.49\times10^{-7}$			$4.86\pm0.48\times10^{-7}$
4.2		$3.48\pm0.40\times10^{-7}$		
4.6			$4.16\pm0.55\times10^{-7}$	
5.2		$8.89\pm1.10\times10^{-8}$		
5.3				$4.90\pm0.80\times10^{-8}$
6.2		$1.69\pm0.27\times10^{-8}$		
6.3				$4.20\pm1.29\times10^{-8}$
7.0	$8.02\pm0.37\times10^{-9}$			
7.3			$1.13\pm0.10\times10^{-8}$	
9.1			$4.76\pm0.65\times10^{-8}$	
9.4	$7.63\pm2.67\times10^{-9}$			

Table 6.13. Th surface area normalized dissolution rate ($gm^{-2}d^{-1}$) for Th_3UO_8 and $ZrTh_3UO_{10}$ at various pH under Ar and 10% CO_2

The Th mass in solution (m_{Thsol}) is obtained from Tables 6.7-6.10, the ThO_2 fraction in the ceramic (f_{ThO2}) is calculated from the composition, and the ceramic mass (m_c) and ceramic surface area (SA_c) are given in Table 6.6. The surface area normalized dissolution ($gm^{-2}d^{-1}$) is from

$$R_{LTh} = \frac{dN_{lTh}}{dt} \qquad \textbf{Eq. 6.3}$$

where t is in days. The results for the normalized Th dissolution from the examined ceramics are given below (Table 6.14, Figure 6.14). From this analysis the dissolution tends to decrease with increasing pH. In the experimental range examine there is little recognizable difference between Ar and 10% CO_2 atmosphere. This data indicates the ceramics will be more stable at lower pH. The

data can be used to evaluation the rate of Th dissolution under a variety of conditions and allow a comparison between different experiments.

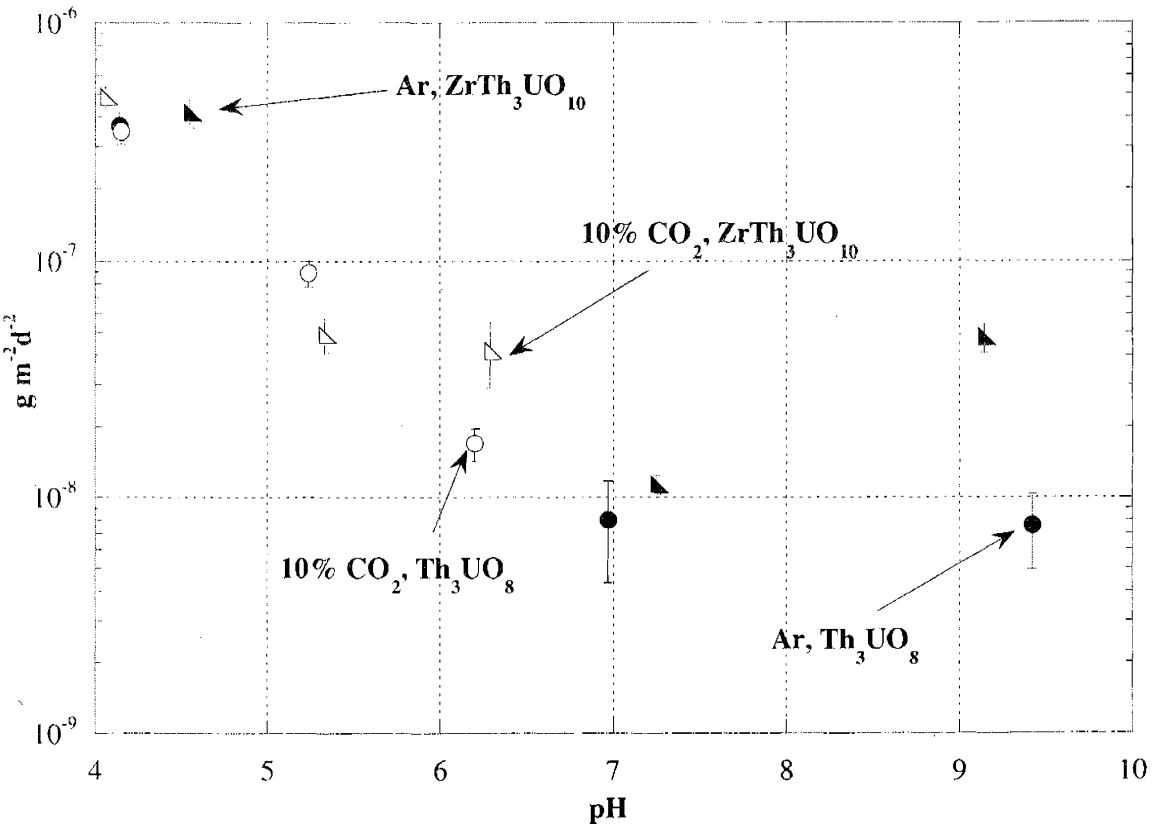

Figure 6.14. Surface area normalized Th dissolution ($gm^{-2}d^{-1}$) from Th_3UO_8 and $ZrTh_3UO_{10}$

6.12.3 Dissolution Equilibrium

The Th equilibrium concentration as a function of pH given in Table 4.9 (Figure 6.15) can be used to evaluate the Th solubility constant for the ceramics. Under the experimental conditions, the Th solution phase is composed of free Th^{4+}, Th hydroxide, and Th carbonate species as shown below:

$$[Th]_{sol} = [Th^{4+}] + \sum_{x} [Th(OH)_x^{4-x}] + \sum_{y} [Th(CO_3)_y^{4-2y}] \qquad \textbf{Eq. 6.4}$$

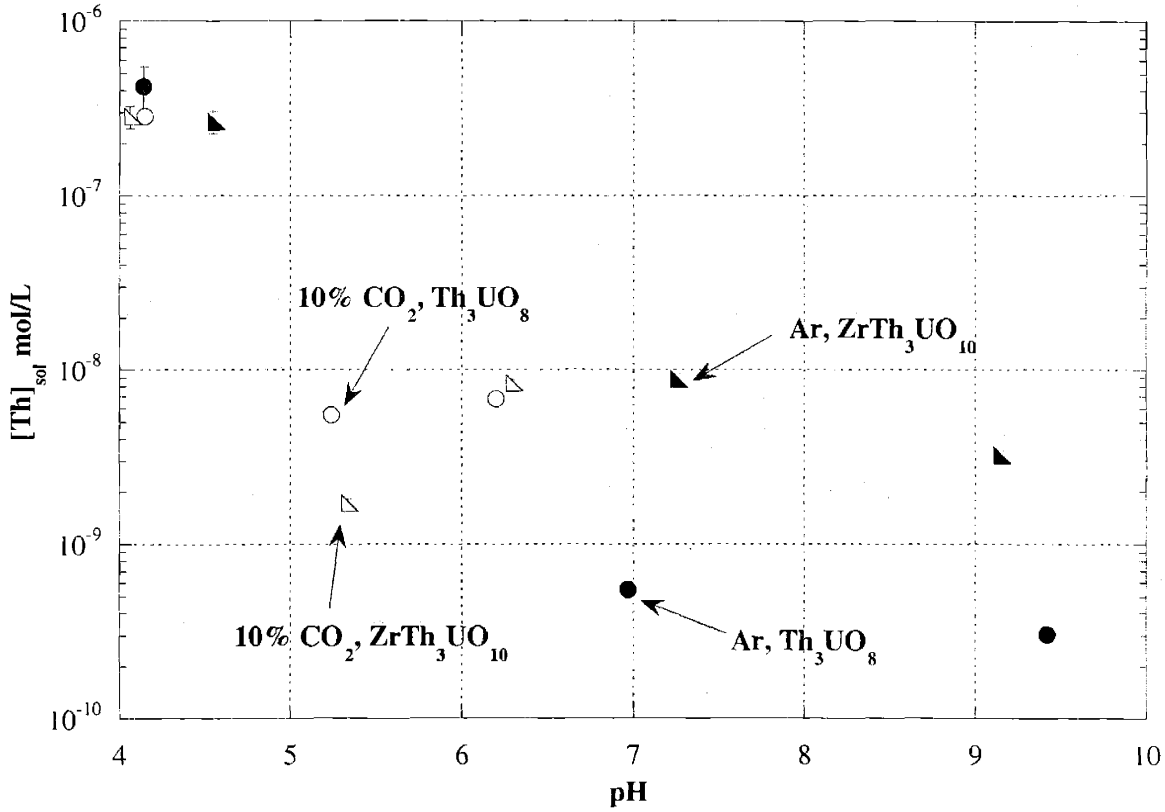

Figure 6.15. Equilibrium Th solution concentration from the dissolution of Th_3UO_8 and $ZrTh_3UO_{10}$

The total Th solution concentration is $[Th]_{sol}$ and the different hydroxide and carbonate species are represented according to the ligand coordination. Polymeric Th species are excluded since the experiment is initiated from conditions below saturation. Additionally, previous speciation analyses of ThO_2 show the polymeric species are not prevalent under the experimental conditions in this work [15]. For the hydroxide and carbonate species, the stability constants are given as:

$$\beta_{1z} = \frac{[ThL_z]}{[Th^{4+}][L]^z} \qquad \textbf{Eq. 6.5}$$

where L is either OH^- or CO_3^{2-} and Z the number of coordinating ligands. Charges for the ligands and Th complex are not included in equation 5 for simplicity. The solubility constant of the Th from the ceramic is defined as:

$$K_{spTh}=[Th^{4+}][OH^-]^4 \qquad \textbf{Eq. 6.6}$$

Rearranging equation 4, defining the free Th^{4+} from the K_{sp}, including the stability constants for the definition of the Th complex concentration and solving for the K_{sp} results in:

$$K_{spTh} = \frac{[Th]_{sol}[OH^-]^4}{1+\sum_x \beta_{1x}[OH^-]^x + \sum_y \beta_{1x}[CO_3^{2-}]^y} \qquad \textbf{Eq. 6.7}$$

The solution conditions provide the hydroxide and carbonate [16] concentrations. Constants for Th hydrolysis [10] and carbonate [17] complexation are from the literature. The solubility constants evaluated for Th from Th_3UO_8 and $ZrTh_3UO_{10}$ are presented below (Table 6.15). The speciation calculations show that Th hydroxide species are the dominant solution species. The resulting solubility constant values were consistent with the literature for the K_{sp} of ThO_2 analyzed under similar conditions [6]. This indicates the Th in the ceramic is well behaved and existing literature data can be useful in describing the behavior of Th in the system.

	Th_3UO_8		$ZrTh_3UO_{10}$	
pH	Ar	10% CO_2	pH	Ar
4.1	-48.5±0.1			-48.9±0.1
4.2		-48.7±0.1		
4.6			-48.0±0.1	
5.2		-48.6±0.2		
5.3				-49.0±0.1
6.2		-47.5±0.1		
6.3				-47.4±0.1
7.0	-48.2±0.2			
7.3			-46.9±0.2	
9.1			-47.2±0.1	
9.2	-48.2±0.2			

Ave $K_{spTh3UO8}$=48.3±0.4, Ave $K_{spZrTh3UO10}$=47.9±0.9

Table 6.14. Evaluate Th K_{sp} for Th_3UO_8 and $ZrTh_3UO_{10}$

6.12.4 Speciation Modeling

Based on the experimental results, the solubility of Th from the ceramics was calculated with the K_{spTh} from $ZrTh_3UO_{10}$ from pH 4-9 with a 1% CO_2 atmosphere in 0.1 M $NaClO_4$ at 25 °C. The resulting Th solution concentration is compared to U from the dissolution of UO_2 examined under the same conditions with an Eh of –200 mV, 0 mV, and 200 mV (Figure 6.16).

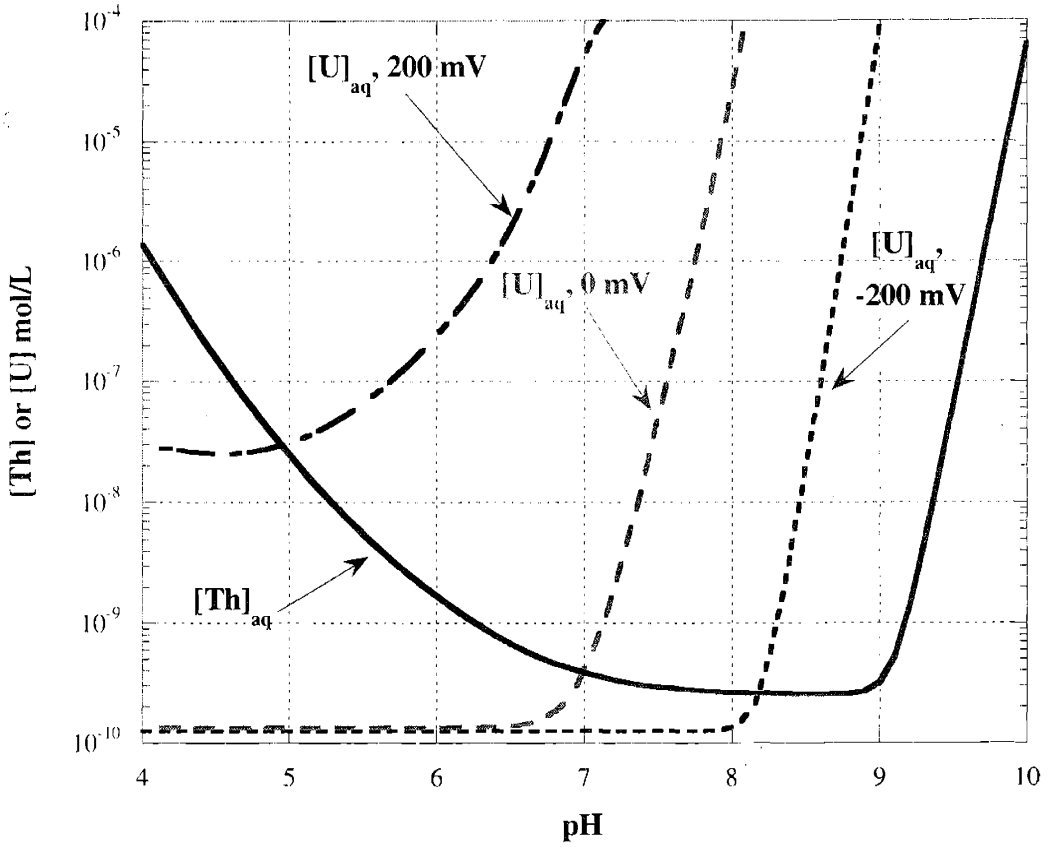

Figure 6.16. Calculated Th and U equilibrium solution concentration from $ZrTh_3UO_{10}$ and UO_2

The Th solubility is at a minimum from pH 7.2-9. For the UO_2 dissolution, the solubility is strongly affected by the redox conditions due to the IV/VI oxidation couple for U. The Th solution concentration minimum is greater than the U minimum for 0 and –200 mV. However, the U solution concentration increases above the Th solution concentration at pH 7 for 0 mV and pH 8.3 for –200 mV due to the formation of aqueous uranyl carbonate species. For the oxidizing condition at 200 mV, the crossover point for the solution concentrations is at pH 5. Above pH 5 the uranium solution concentration is greater than Th solution concentration due to uranyl carbonate formation and the oxidizing conditions preferential for hexavalent uranium.

These results indicate the ThO_2 will dissolve less than UO_2 under high pH and oxidizing conditions. This is important for direct disposal of fuels based on ThO_2-UO_2 and UO_2 ceramics. The nuclear waste repository near field water conditions are expected to evolve with time. The exact conditions of the evolving near field ground water are functions of numerous parameters, including temperature, time, backfill material, and container material [18]. However, the general trend is an increase in pH, possibly as high as pH 13 with elevated temperatures possible. If the repository is oxidizing, the dissolution of UO_2 is expected be greater than the dissolution of ThO_2.

6.13 Conclusions

The dissolution of Th from Th_3UO_8 and $ZrTh_3UO_{10}$ can be described with a 1st order rate constant. The rate constants vary from $6x10^{-4}$ hr^{-1} to $4x10^{-2}$ hr^{-1} and increases with pH under the experimental conditions examined. The Th dissolution normalized to the surface area is found to be the highest ($5x10^{-7}$ $gm^{-2}d^{-1}$) at the lowest pH and decreases with increasing pH. The evaluation of dissolution over time yielded equilibrium concentrations for Th under the experimental conditions. The Th solution concentration was largest at pH 4 as expected. The Th equilibrium data was used to evaluate solubility constants. Resulting K_{sp} values were found to agree with literature values from experiments performed with ThO_2 under similar solution conditions. The inclusion of Zr was found to have no noticeable affect on Th dissolution or solubility. The evaluated constants were used to calculate Th solubility from the Th_3UZrO_{10} ceramic in 0.1 M $NaClO_4$ from pH 4-9 with a 1% CO_2 atmosphere at 25 °C. Under oxidizing conditions, the solution phase concentration of Th was calculated to be less than the solution phase concentration of U.

References

1. Kazimi, Mujid et al.: Advanced Proliferation Resistant, Lower Cost, Uranium-Thorium Dioxide Fuels for Light Water Reactors, Nuclear Energy Research Initiative Project 99-0153 Quarterly Report, May 2000.

2. Gong, W.L.; Lutze, W.; Ewing R.C.: Zirconia ceramics for excess weapons plutonium waste, J. Nucl. Mat. **277**, 239-249 (2000).

3. Benedict, Manson; Pigford, T.H.; Levi, H.V. Nuclear Chemical Engineering 2nd Edition. 1981 McGraw-Hill 318-321

4. De Lima, N.B. and Imakuma, K.: X-Ray Diffraction Study Of The Formation Of Solid Solutions In Urania-Thoria Prepared By Aqueous Chemical Processes. J. Nucl. Mat., **135**, 215-221 (1985).

5. Balek, V.: Application Of Emanation Thermal Analysis For Characterization Of Intermediate Products Of Urania And Thoria Cermaics. J. Nucl. Mat., **153**, 41-49 (1988).

6. Ryan, J.L., Rai, D. : Thorium(IV) Hydrous Oxide Solubility. Inorg. Chem., **26(24)**, 4140 (1987).

7. Felmy, A.R., Rai, D., Mason, M.J.: The Solubility of Hydrous Thorium(IV) Oxide in Chloride Media: Development of an Aqueous Ion-Interaction Model. Radiochim. Acta, **55(4)**, 177 (1991).

8. Oesthols, E., Bruno, J., Grenthe, I.: On the Influence of Carbonate on Mineral Dissolution: III. The Solubility of Microcrystalline ThO_2 in CO_2-H_2O Media. Cosmochim. Acta. **58(2)**, 613 (1994).

9. Rai, D., Felmy, A.R., Sterner, S.M., Moore, D.A., Mason, M.J., Novak, C.F.: The Solubility of Th(IV) and U(IV) Hydrous Oxides in Concentrated NaCl and $MgCl_2$ Solutions. Radiochim. Acta, **79(4)**, 339 (1997).

10. V. Neck, V., Kim, J.I.: Solubility and Hydrolysis of Tetravalent Actinides, Radiochim. Acta **89**, 1 (2001).

11. Scatchard, G.: Concentrated Solutions of Strong Electrolytes. Chem. Rev. **19**, 309 (1936).

12. Curran, G., Sevestre, Y., Rattray, W., Allen, P.G., and Czerwinski, K.R.: Characterization and Dissolution of $ZrTh_3UO_{10}$ and Th_3UO_8 Ceramics. MRS Scientific Basis for Nuclear Waste Management XXV, 2002

13. Delany, J.M., and Lundeen, S.R.: The LLNL Thermodynamic Database. Technical Report UCRL-21658, Lawrence Livermore National Laboratory (1990).

14. Dzombak, D.A. and Morel, F.M.M.: Surface Complexation Modeling. Hydrous Ferric Oxide. John Wiley and Sons, New York (1990).

15. Baes, C.F. and Mesmer, R.E.: The Hydrolysis of Cations. Krieger Publishing Co., Malabar, FL, pp 162-168 (1986).

16. Fanghanel, T., Neck, V., and Kim, J.I.: The Ion Product of H_2O, Dissociation Constants of H_2CO_3 and Pitzer Parameters in the System $Na^+/H^+/OH^-/HCO_3^{2-}/ClO_4^-/H_2O$ at 25°C, J. Sol. Chem., **25(4)**, 327 (1996).

17. Grenthe, I., Lagerman, B.: Studies on Metal Carbonate Equilibria. 23. Complex Formation in the Th(IV)-H_2O-CO_2(g) System, Acta Chem. Scand., **45**, 231 (1991).

18. The Scientific and Regulatory Basis for the Geological Disposal of Radioactive Waste, David Savage Editor, Wiley and Sons, Chichester, England, pp 78-91, (1995).

Gamma-radiation effects on dissolution of Th_3UO_8

6.14 Abstract

The effect of gamma radiation on the dissolution of Th_3UO_8 ceramics was studied using the MIT research reactor spent fuel pool gamma source to simulate the radiation environment in a repository. Th_3UO_8 powders and pellets fabricated via a precipitation process were immersed in purified water solutions adjusted to pH 4, 7, and 10 and exposed to a dose rate of 300 Gy/hr. Samples were removed periodically for 6 weeks for actinide concentration analysis by ICP-MS or ICP-AES. In addition, similarly prepared samples were run in the lab at 25 °C and 65 °C as controls. Results showed strong pH dependence for the thorium samples, with a maximum Th solution concentration of 10^{-6} M at pH 10 under irradiation, two orders of magnitude higher than the non-irradiated controls. Irradiated uranium concentrations were consistent at 10^{-6} M, indicating no pH dependence. This can be attributed to oxidation from U(IV) to U(VI) by the radiolysis products produced in the γ-field. The largest increase over the control was a factor of 10 at pH 7. As total dose accumulated in all samples, the actinide concentration reached a peak and then began to decrease, indicating a possible precipitation reaction. It is hypothesized that the increased thorium solubility is caused by the formation of hydroxide or carbonate colloids, explaining the pH dependence of the reaction.

6.15 Introduction

Research into alternatives to the standard uranium oxide fueled boiling and pressurized water reactors has led to a resurgence of interest in the thorium fuel cycle. Evidence that in comparison with the uranium oxide cycle the thorium fuel cycle may be both economically superior [1] and a more robust waste form [2] has fueled this revival. Before the thorium fuel cycle can be implemented on an industrial scale, however, spent fuel behavior must be better understood.

Many laboratory experiments have been conducted to determine the solubility of thorium oxide under a various conditions [3]. However, since current US policy for the disposition of spent nuclear fuel calls for deep geological disposal, it is important to understand the behavior of thorium fuel in such an environment. This includes understanding the effects of the high gamma radiation field to which the spent fuel will be subjected over many years on the dissolution of the fuel components.

In addition, while the total ThO_2 solubility should remain constant with the same ligands present, colloid formation could increase significantly under radiation conditions. The effects on the thorium-uranium oxide solid solution are potentially more complicated due to uranium redox reactions. Studies of the effects of gamma radiation on UO_2 have shown that while some radiolytic decomposition products such as H_2O_2 increase the dissolution rate [4,5], radiolytically produced reductants like H_2 may limit the total solubility of uranium by inhibiting oxidation to the more soluble U(VI) [6].

6.16 Experimental

Th_3UO_8 was fabricated from the nitrate salts precipitated in as oxalates and hydroxides in a mixture of oxalic acid and ammonium hydroxide. The precipitate was dried at 150 °C and milled into a fine powder. The powder was calcined for 1 hour at 650 °C to produce the oxide. Some of the powder was pressed into 7 mm diameter cylindrical pellets and sintered at 1500 °C for four hours. The composition of the powders and pellets were confirmed by XRD using a Rigaku RU300 x-ray generator with a 185 mm diffractometer operating at 60 kV and 300 mA (18 kW).

Solutions were prepared from purified water and pH adjusted using 0.1 M HNO_3 and 0.1 M NaOH to pH 4, 7, and 10. Individual 7 mL glass containers were prepared for each sampling. The vials were filled with 6 mL of the appropriate pH solution and either 0.1 g of the powder or a sintered pellet under air. Powder sample sets of ten vials were prepared for each pH. Due to the limited number of pellets, one series of six vials at pH 7 was prepared. The vials were placed in the spent fuel pool at the MIT Nuclear Reactor Lab. Samples received an average dose of 30 kRad/hr. Samples were removed at gradually lengthening intervals beginning at three days for a period of 48 days. Control samples of powders and pellets were placed in 100 mL flasks at each pH and placed in an oven at 65 °C to simulate the thermal conditions in the sample location in the spent fuel pool. In addition, powder samples were placed in 100 mL flasks at each pH step at room temperature. Sampling intervals for the unirradiated samples were consistent with those of the irradiate samples.

Immediately following removal from the spent fuel pool, 5 mL of liquid was removed from each vial and filtered using at 0.45 μm Acrodisc filter. A 4.5 mL sample was pipetted into a fresh vial and spiked to 0.1 M HNO_3 with 30 μL of concentrated HNO_3. Additional 5 mL samples were taken from each unirradiated

flask and prepared in the same manner. Uranium and thorium concentrations were determined using a Fisons VG Plasmaquad ICP-MS or a Spectro Analytical Instruments Spectroflame ICP-AES depending on concentration. Standards were created using SCP Science 1000 μg/mL Th and U standards diluted in 5 vol% HNO_3 to cover a range of concentrations from 1 nM/L to 0.5 mM/L. For ICP-MS analysis, standards were spiked to 10 ppb ^{209}Bi for mass calibration.

6.17 Results and Discussion

Expected species concentrations for thorium and uranium under the range of conditions explored were calculated using the stability constants reported by Kim et al [3] and are shown in Figures 6.17 and 6.18 respectively. For the thorium system, the carbonate species become dominant for neutral pH and above. In the uranium system, the carbonate species dominate throughout the pH range examined.

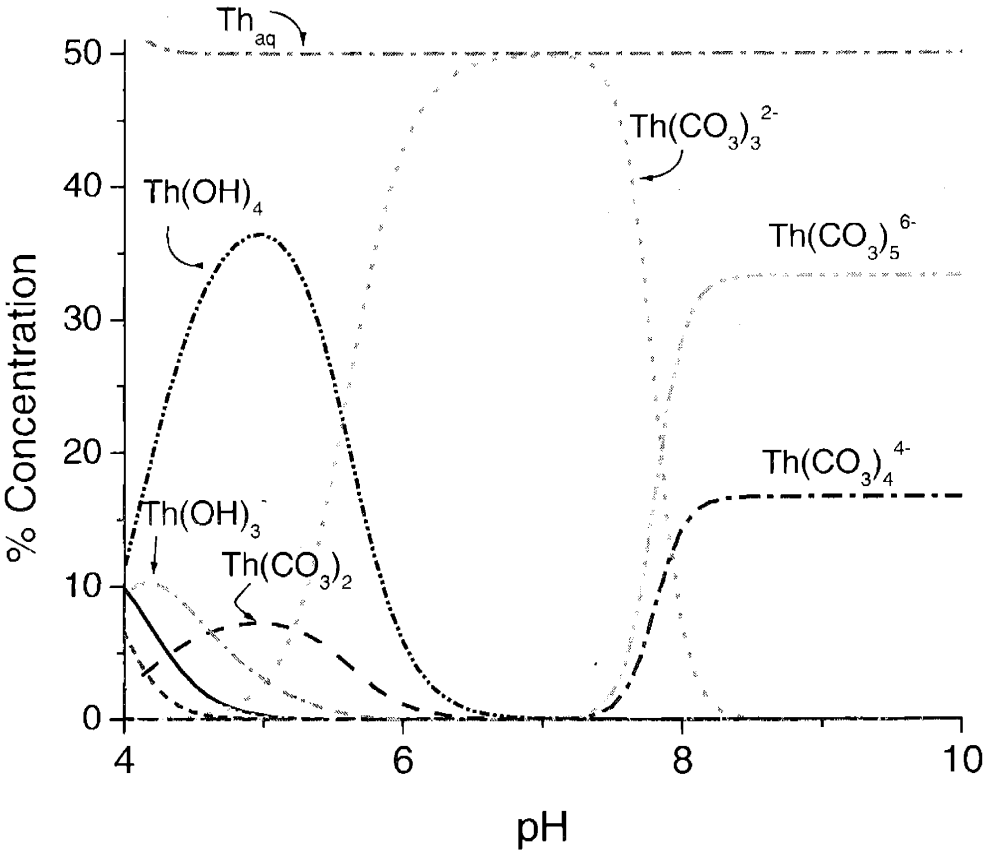

Figure 6.17. Expected thorium species concentration

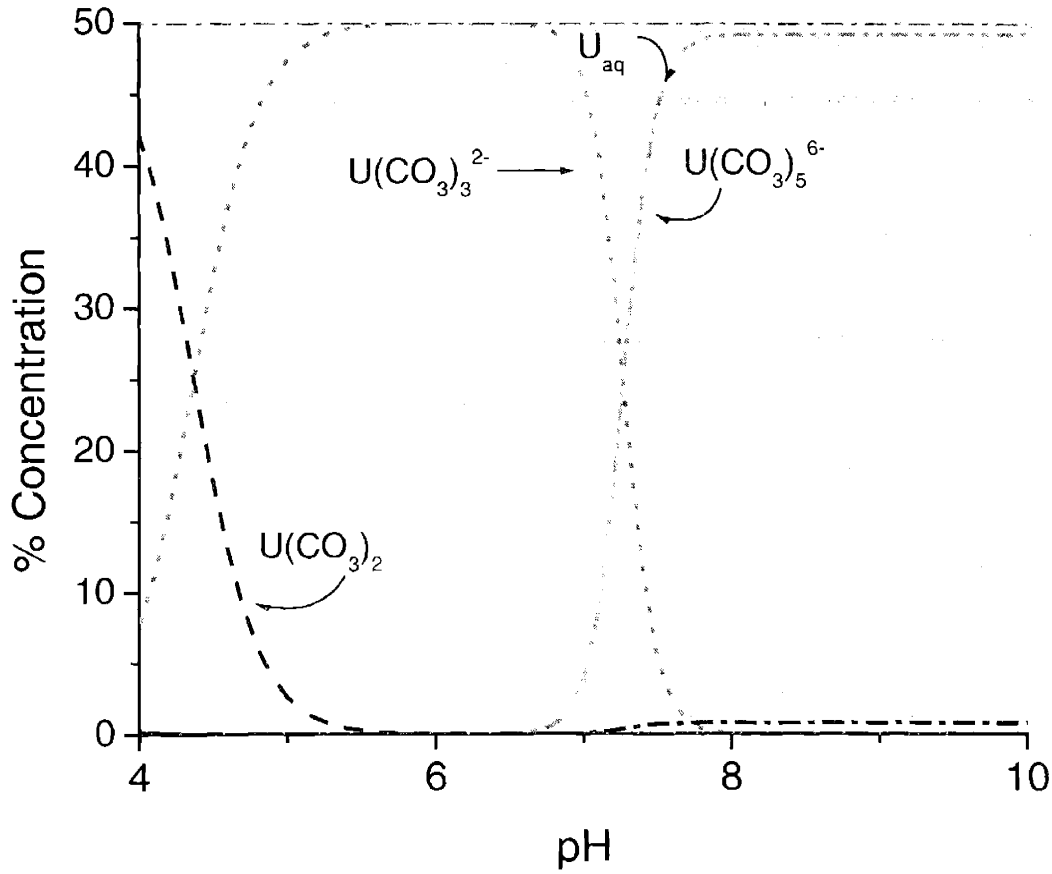

Figure 6.18. Uranium species concentrations over pH range studied

6.17.1 Thorium results

Figures 6.19-6.21 show thorium concentrations at pH 4, 7 and 10 respectively. Analysis of the solutions exposed to gamma irradiation shows that concentrations increase significantly compared to the unirradiated at pH 7 and 10, where the carbonato species are dominant. At pH 4, there is no real difference between the irradiated samples and the heated powders. The high degree of scatter in the data is due to the extremely low concentration of the samples.

The unirradiated room temperature powder samples and heated pellets showed much lower dissolution. Concentrations were consistent through the pH range for these samples. The pellets irradiated in the spent fuel pool also showed much less dissolution than the irradiated powders. This can be attributed to the fact that the surface area of the pellets is an order of magnitude lower than the powders. As pH increased from 4 to 7 to 10, the concentration of thorium in the aqueous phase of the irradiated powders increased an order of magnitude at each step. Since the thorium concentration from the other samples did not change significantly with pH, the effective increase in thorium solubility under the high intensity gamma field was two orders of magnitude higher than the unirradiated samples at pH 10.

No kinetics information could be derived from the data. The samples were exposed to the high gamma field for over a 45 days, however it appears that equilibrium was achieved rapidly and the sampling interval of 3-7 days was too long to obtain any useful kinetics data. In addition, in all of the irradiated samples, a feature appears toward the end of the data collection where the thorium concentration appears to increase by up to an order of magnitude and then return to the initial "equilibrium" concentration. This is most likely attributable to a saturation – precipitation reaction that occurs over time in the samples.

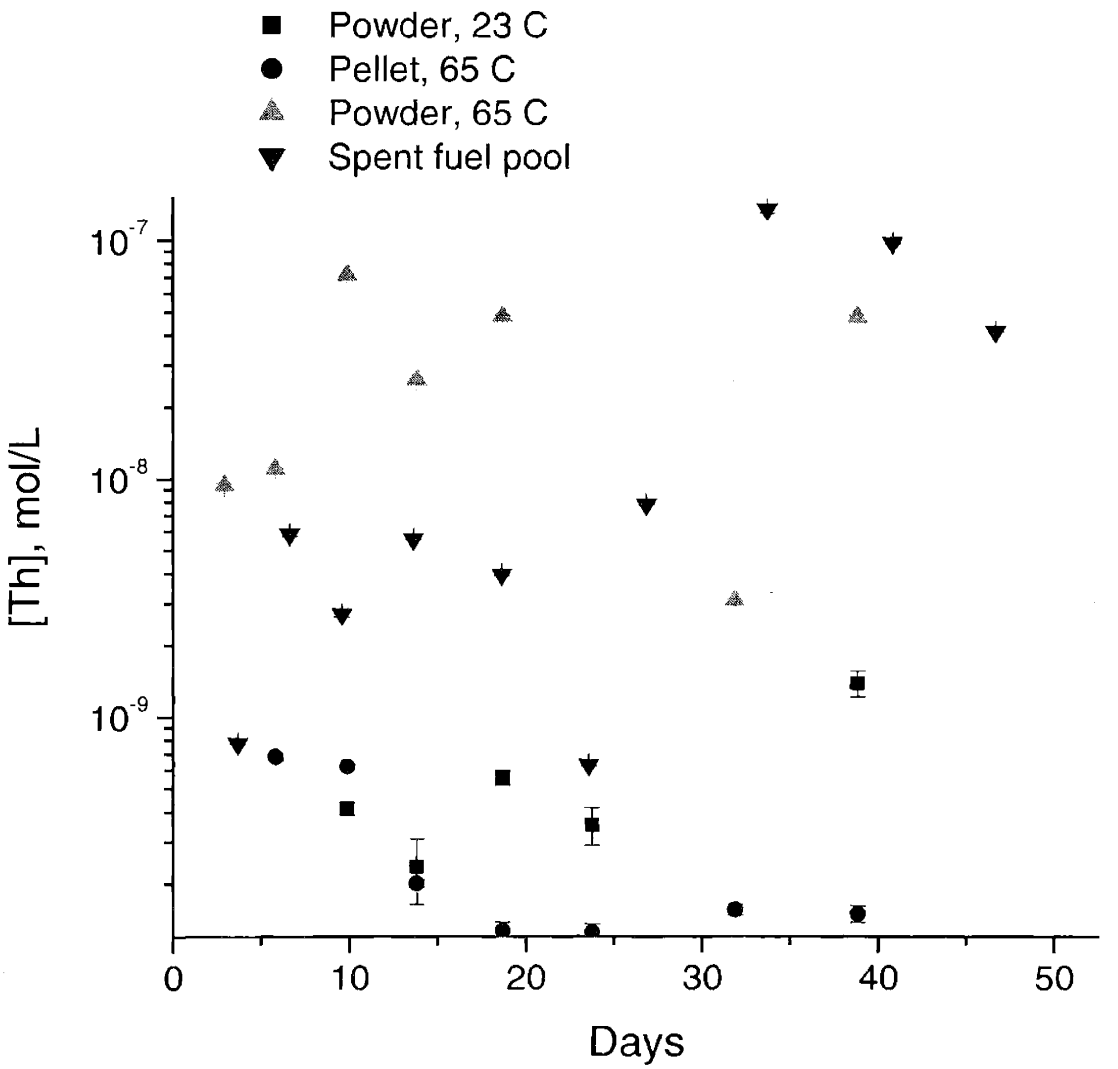

Figure 6.19. Dissolution results for thorium at pH = 4

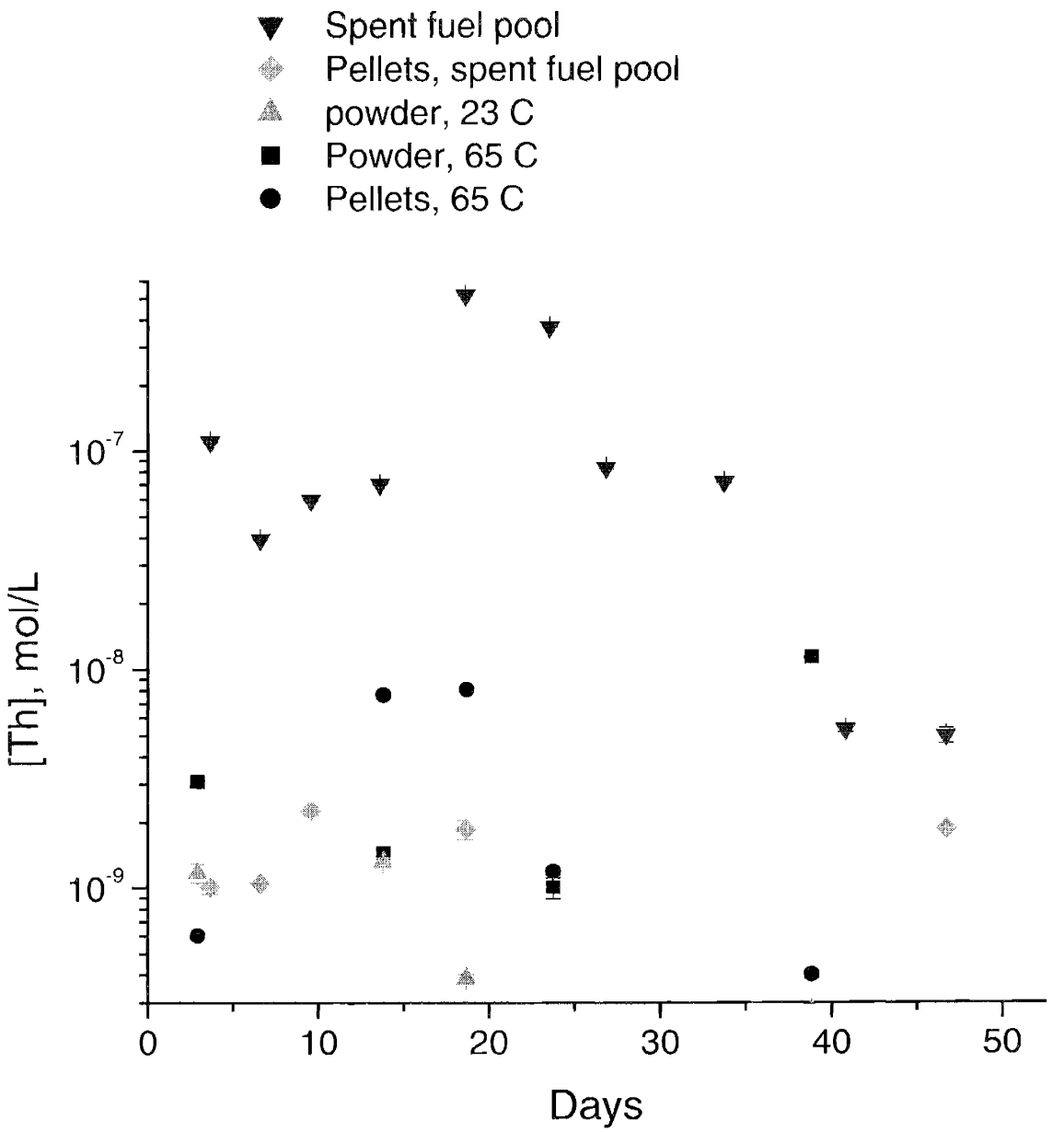

Figure 6.20. Dissolution results for thorium at pH 7

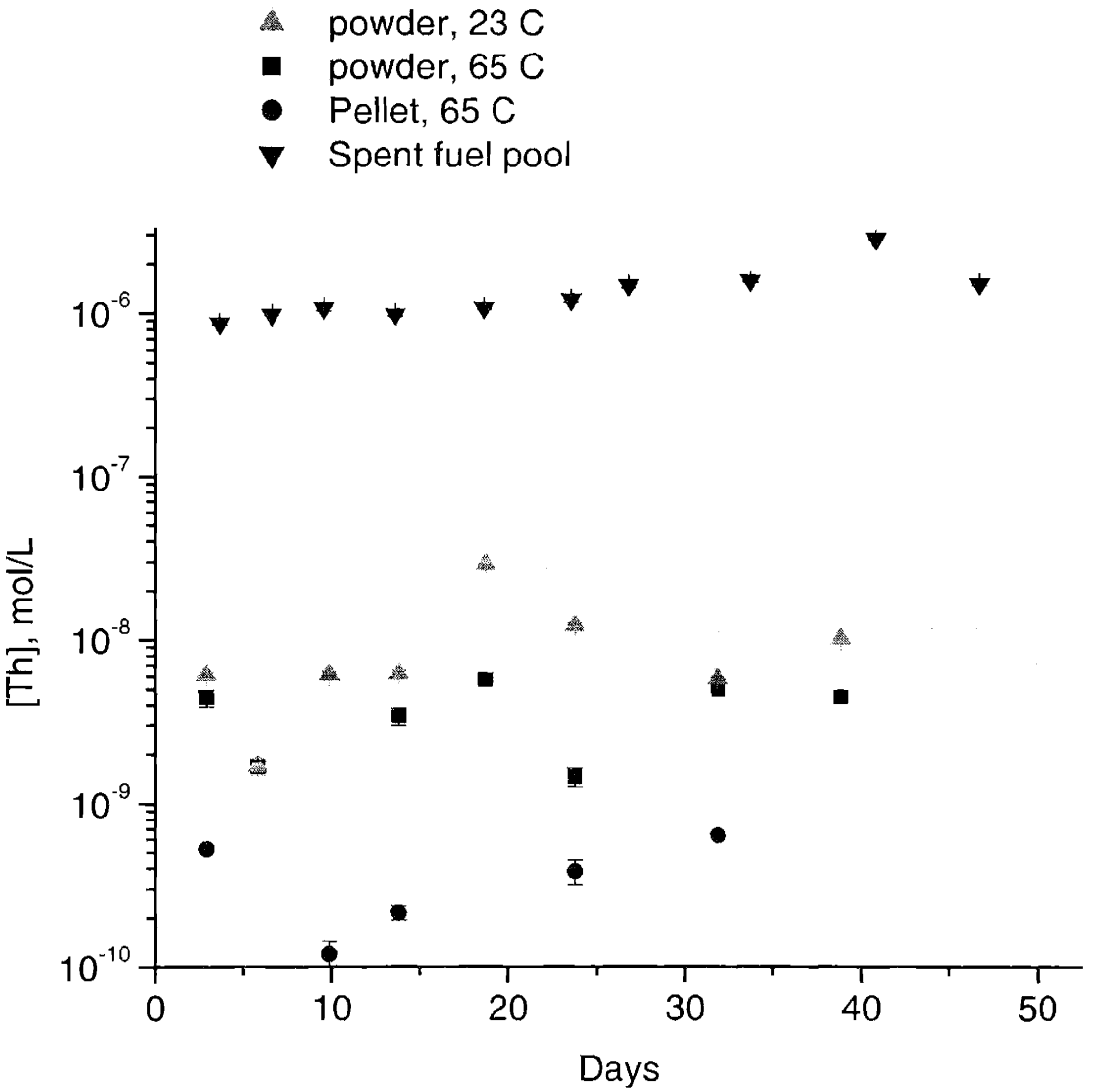

Figure 6.21. Dissolution results for thorium at pH 10

6.17.2 *Uranium results*

Uranium data is shown in Figures 6.22 – 6.24 for pH 4 -10, respectively. Unlike the thorium results, the uranium concentrations in the aqueous phase for the irradiated powder samples remains constant over the pH range studied at approximately 1 μmol/L. The pellets once again showed aqueous concentrations orders of magnitude lower, with the irradiated and unirradiated pellets at pH 7 showing relatively consistent concentrations. This is again attributed to the lower surface area of the pellets. The pH 7 unirradiated pellet data was the only dataset that could yield any kinetics information. Much more variation with pH was evident in the powdered samples. The greatest effect of gamma irradiation on the aqueous uranium concentration could be seen at pH 7, where the unirradiated concentration is at the minima. This is the known minima for uranium solubility under environmental conditions. At this pH, the irradiated samples show a solubility increase of an order of magnitude over the unirradiated samples. Like the thorium samples, in the irradated powder data, small increases develop that quickly peak and then return to the previous values over the course of a week or two.

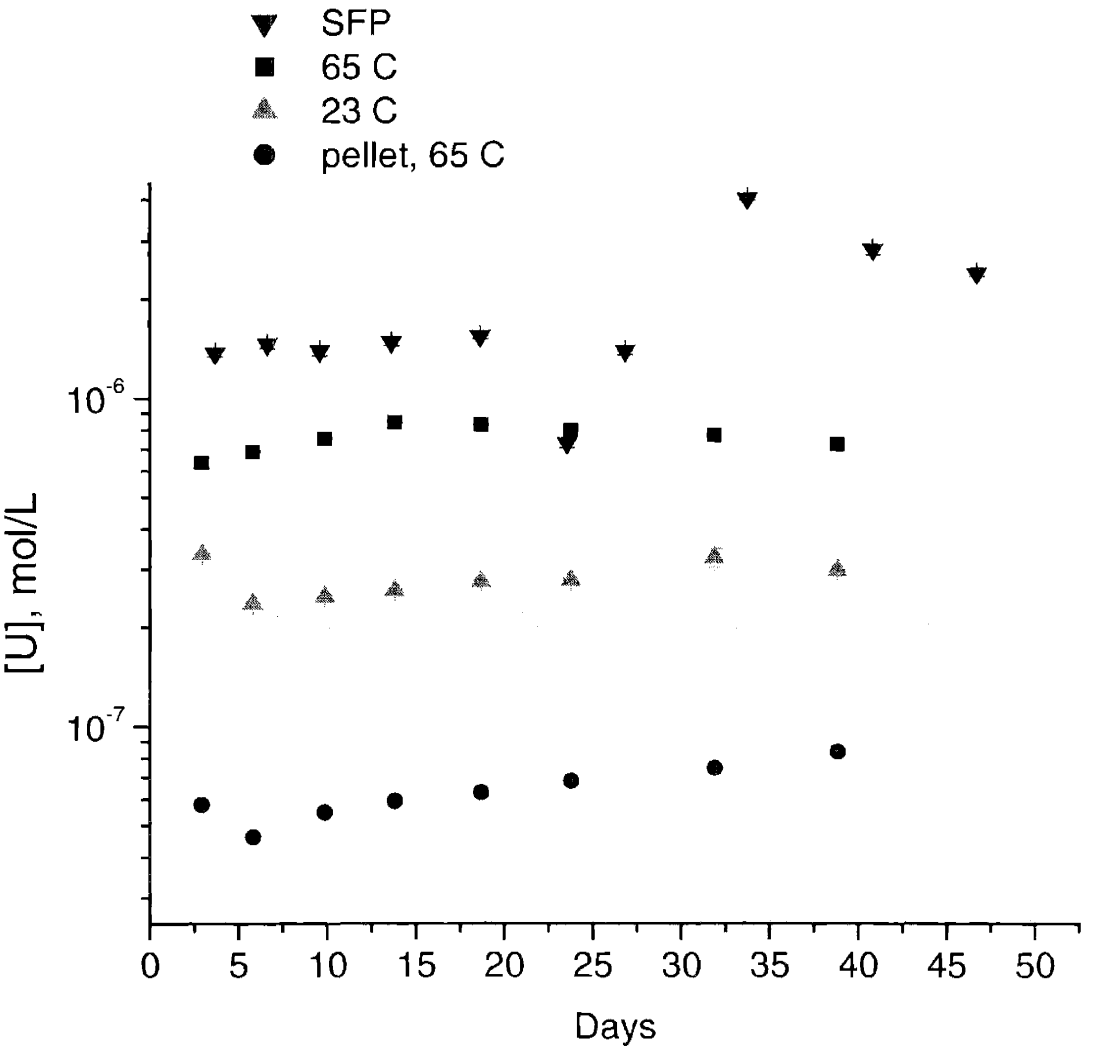

Figure 6.22. Dissolution results for uranium at pH 4

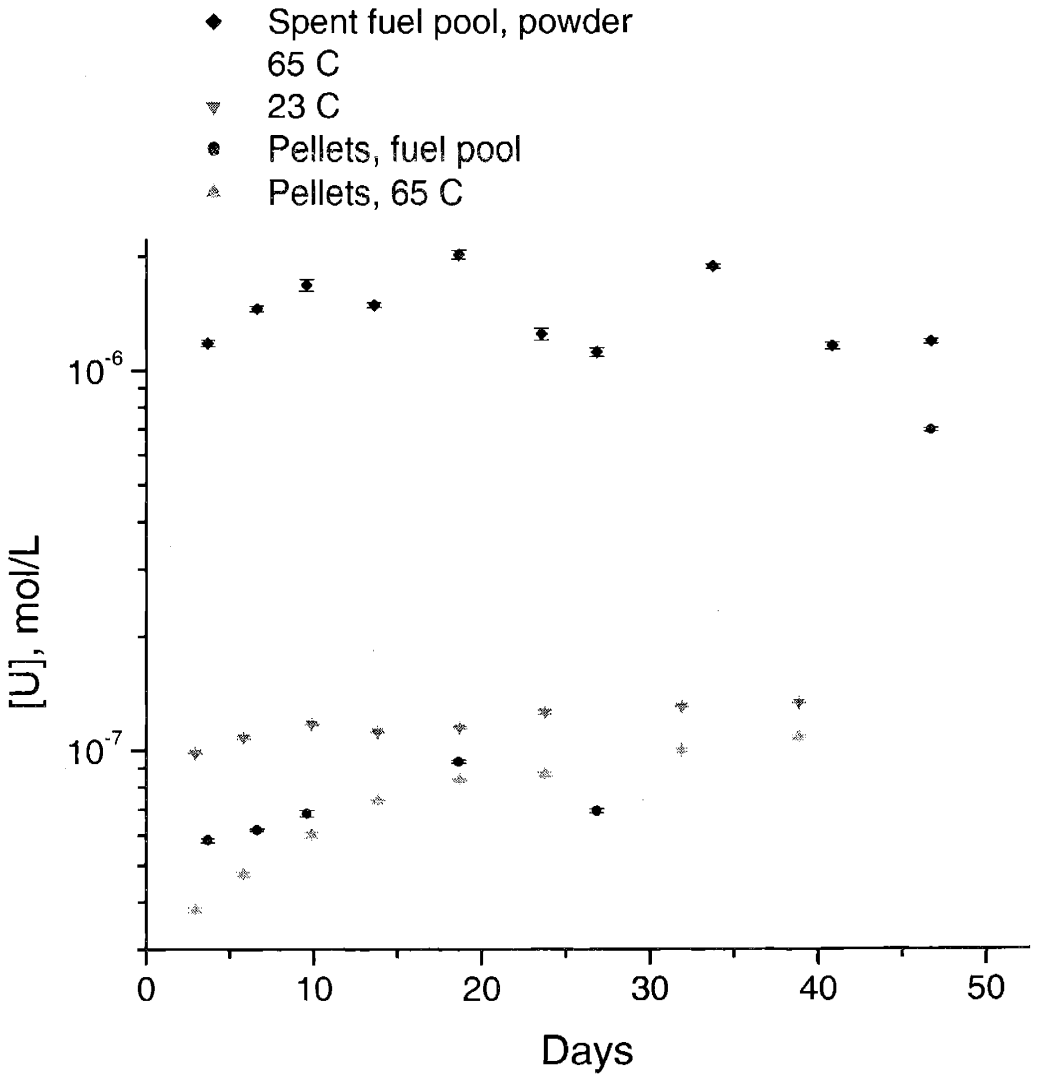

Figure 6.23. Dissolution results for uranium at pH 7

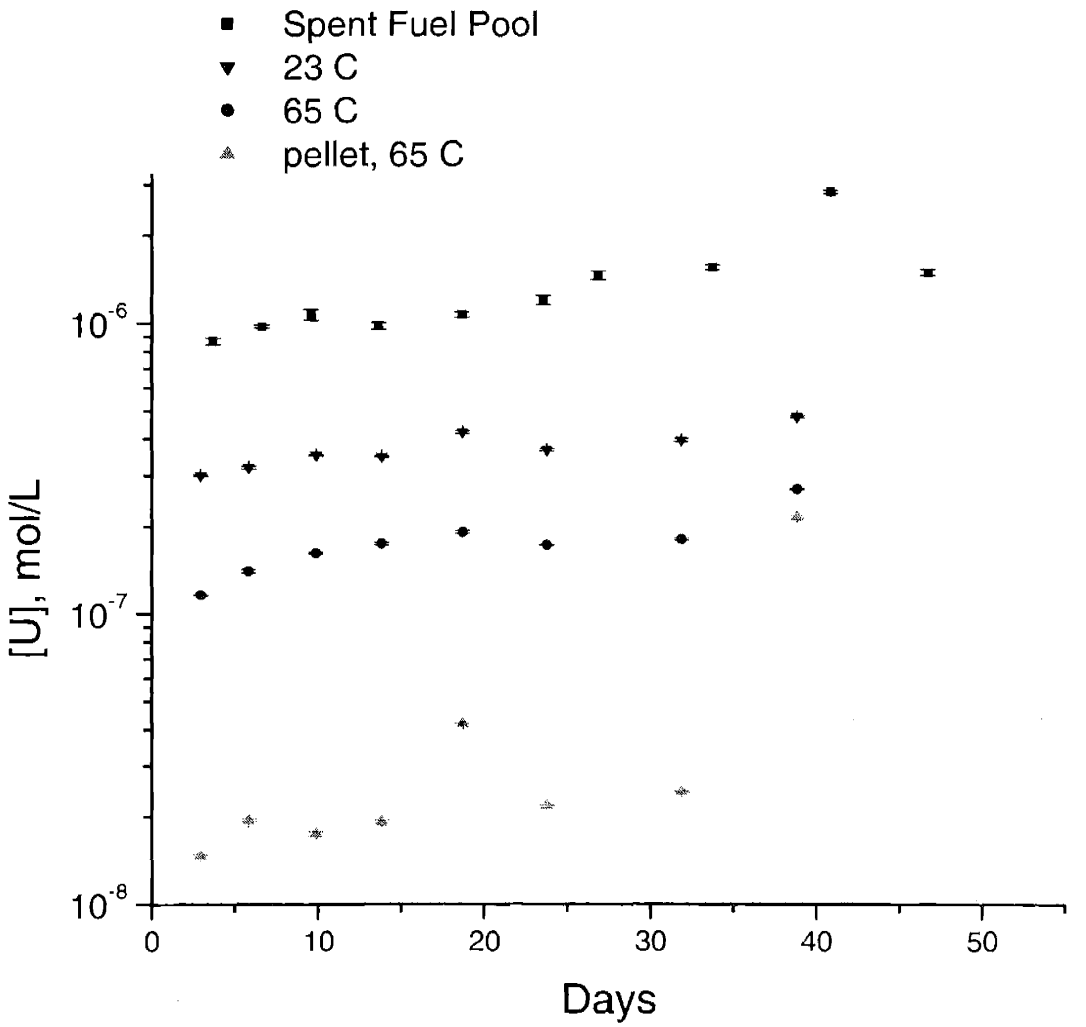

Figure 6.24. Dissolution results for uranium at pH 10

6.18 Conclusions

The effect of gamma radiation on the dissolution of Th_3UO_8 fuels is significant. Results show a maximum solubility increase of two orders of magnitude for thorium at pH 10 and one order of magnitude for uranium, at pH 7. The uranium solubility under the 30 kRad/hr gamma field was consistently 1 μmol/L throughout the pH range. This can be attributed to the fact that the increased solubility is caused by oxidation of the U(IV) to the much more soluble U(VI) by radiolysis products [5]. This effect overwhelms any pH effects that would have otherwise dominated. It cannot, however, explain the increased solubility of the thorium samples. Thorium exists solely as Th(IV) in natural systems and cannot be further oxidized. Because the increase in thorium solubility under γ-irradiation clearly varies with pH, it is postulated that the increased thorium solubility is due to the increased formation of carbonate colloids. Actinides in the +4 oxidation state are most likely to produce colloids [7]. The carbonate species only become important for pH greater than 5 (figure 6.17), so no effect would be seen at pH 4. In addition, above pH 8 the higher carbonate species begin to dominate. This could explain the further increase in thorium solubility at pH 10. The peak features can therefore be explained as the gradual formation of larger colloids that either precipitate back out of solution or are too large to pass through the filters used. In either case, this could indicate limited mobility of the colloid species formed in the far field as they will tend to precipitate out of solution.

6.19 References

1. Kazimi, Mujid et al. *Advanced Proliferation Resistant, Lower Cost, Uranium-Thorium Dioxide Fuels for Light Water Reactors,* Nuclear Energy Research Initiative Project 99-0153 Quarterly Report, May 2000
2. Curran, G. et al, Characterization and Dissolution of $ZrTh_3UO_{10}$ and Th_3UO_8 Ceramics, Mater. Res. Soc. Symp. Proc.(Scientific Basis for Nuclear Waste Management XXV), 2002
3. Neck, V. and Kim, J.L. Solubility and Hydrolysis of Tetravalent Actinides, *Radiochimica Acta,* 2001. 89 (1-16)
4. Ermatov, S.E. et al, Phase changes of uranium oxides under irradiation, *Prokhozhdenie Elem. Chastits Veshchestvo,* 1983 (78-83)
5. Gromov, V. Dissolution of uranium oxides in the γ-irradiation field, *Radiation Physics and Chemistry,* 1981. 18(1-2) (135-46)
6. King, F. et al, *The effect of hydrogen and gamma irradiation on the oxidation of UO_2 in 0.1 mol/L NaCl solution,* SKB Technical Report (TR-99-27), 1999.
7. Silva, R.J. and Nitsche, H. Actinide Environmental Chemistry , *Radiochimica Acta,* 1995. 70/71 (377-396)

6.20 Suitability of thoria-urania fuel for repository disposal

Thorium oxide based fuels show promise to be a more stable waste form in repository environments than the standard uranium oxide fuel. Results from the dissolution experiments indicate the ThO_2 will dissolve less than UO_2 under high pH and oxidizing conditions that will be expected in concrete-filled repositories after some time has passed. This is important for direct disposal of fuels based on ThO_2-UO_2 and UO_2 ceramics. If the repository is oxidizing, the dissolution of UO_2 is expected be greater than the dissolution of ThO_2. The inclusion of Zr was found to have no noticeable affect on Th dissolution or solubility.

Results from dissolution under high γ-irradiation indicate that increased solubility of both the urania and the thoria phases occurs. Because the increase of thorium solubility cannot be explained by oxidation by the hydrolysis products that increases the uranium solubility, a different mechanism must be proposed. Formation of thorium carbonate colloids at higher pH is the most likely candidate. The apparent precipitation of the colloids over time indicates the size eventually grows too large to remain in solution. Thus it is likely that the presence of the thorium carbonate colloids could hinder migration into the far field due to their large size.

7 Characterization of UC and UC/US fuels

7.1 Abstract

Uranium carbide (UC) and uranium sulfide (US) are of interest as potential replacements for UO_2 fuels in Generation IV nuclear reactors, specifically the Gas Cooled Fast Reactor (GCFR) project. Oxidation of UC under CO_2 is of concern at temperatures above 500 °C, and current GCFR design calls for 300 MW_e gas turbines that operate at 45% thermal efficiency at 550 °C. Mixed UC-US fuels have been shown to decrease oxidation effects under air. The structure of uranium in UC and mixed UC/US solid solutions fabricated for study of oxidation effects under CO_2 were analyzed using X-ray absorption spectroscopy (XAS). The UC samples were fabricated by carbothermic reduction of UO_2. The UC/US samples of varying ratios were fabricated with a two-step process utilizing zinc sulfide. Results revealed imperfections in the fabrication processes as significant concentrations of UO_2 were present in all samples. Uranium was found to be in the tetravalent state in all samples. Structures of all samples are presented. Differences in structure between UC samples were found, indicating a need to refine the synthesis procedure. UC/US ratios followed the expected trend but were not as predicted. The amount of UO_2 contamination increased with increasing UC content, indicating the UC fabrication process as the likely source.

7.2 Background

Research into new fuels for Generation IV nuclear reactors has led to increased interest in exotic fuels. Uranium carbide fuels have been proposed for use in the gas cooled fast reactor (GCFR), which will utilize a closed Brayton Gas-Turbine power cycle using supercritical CO_2 as the working fluid due to the unique nature of the plant and nuclear reactor physics requirements. Current GCFR design calls for 300 MW_e gas turbines that operate at 45% thermal efficiency at 550 °C [1]. Oxidation of uranium carbide under a CO_2 atmosphere is a potential concern, as previous studies have revealed interactions between UC and CO_2 at temperatures above 500 °C [2,3]. This could have potentially serious repercussions for safe operation of GCFRs in the event of cladding failure or a pinhole leak developing in the cladding of the reactor fuel at expected operating temperatures.

Addition of uranium sulfide (US) to UC fuel to stabilize the fuel matrix from oxidation has been proposed to balance chemical reactivity effects with reactor physics considerations. Previous work has demonstrated increased resistance of the UC-US solid solution to oxidation under air with increasing concentrations of US [4]. Oxidation effects of the CO_2 atmosphere on UC-US fuels have been studied by Plaue [5]. In order to better understand the oxidation processes and evaluate the stability of UC and mixed UC/US fuels, a better understanding of the materials fabricated for the oxidation studies is needed. X-ray absorption spectroscopy (XAS) was used to analyze the chemical composition of the uranium in the UC and UC/US samples. This complements previous characterizations by x-ray diffraction (XRD) [5].

7.3 Experimental

7.3.1 Synthesis

Uranium carbide was synthesized using the carbothermic reduction of UO_2 as optimized by Mukerjee [6]. A stoichiometric quantity of graphite was thoroughly mixed with UO_2 using a ball mill. This was heated at a rate of 8 °C per minute under flowing argon, followed by a 200 minute hold time at 1650 °C. Uranium carbide/ uranium sulfide solid solutions were fabricated using a two-step process [4]. For the first step, UC was reacted with ZnS in the substitution reaction

$$UC + ZnS \rightarrow US + C + Zn\uparrow \qquad \text{Equation 7.1}$$

where the Zn is volatilized and off-gassed. In the second step, the remaining carbon is reacted with added UO_2 to complete the synthesis:

$$3C + UO_2 \rightarrow UC + 2CO\uparrow \qquad \text{Equation 7.2}$$

Three UC samples created in separate batches were analyzed, in addition to three mixed UC/US samples fabricated to have 75%, 50%, and 25% US concentrations.

7.3.2 XAS preparation

UC and UC/US samples were prepared for XAS analysis by mixing 20-50 mg of finely ground powder from each sample with about 200 mg of biobeads, an x-ray transparent resin. This was placed in an aluminum sample holder and sealed with kapton tape. Samples were then doubly contained in heat sealed polyethylene bags.

Each sample was scanned twice on the uranium L_3 edge in transmission mode on beam line 11-2 at Stanford Synchrotron Radiation Laboratory. Data was collected on ion chambers. A UO_2 standard was measured in line with the samples to calibrate the edge location.

7.4 XAS Characterization

7.4.1 XANES

Oxidation states of uranium in the samples were examined using XANES. The expected oxidation state of U in UC is either +2 or +4, and in US is +2 [7]. The UC samples appear to be a bit more oxidized than the UO_2 standard, as their peaks occur at slightly higher energies. Mixed UC/US samples are more consistent with UO_2 but a trend of increasing edge energy with increasing UC content can be seen (Figure 7.1). All of the absorption edges are within 1.5 eV of the UO_2 standard. The uranium in these samples is on average in the U(IV) state.

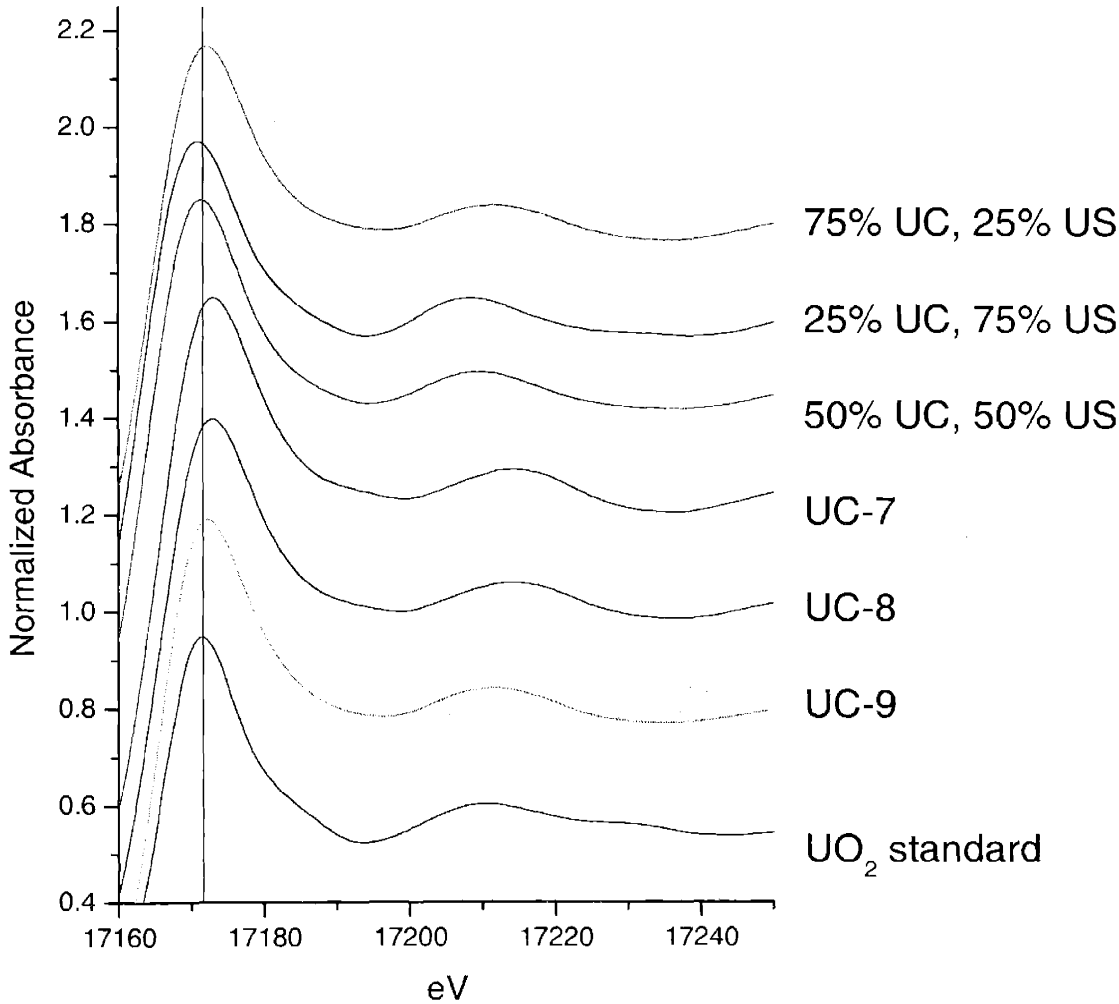

Figure 7.1 XANES spectra of uranium L_3 edge for UC and UC/US samples.

7.4.2 EXAFS

EXAFS analysis was performed using EXAFSPAK, ATOMS, and FEFF8. FEFF models were created for UC, US, and UO_2. Paths from each model were used as necessary in fitting the samples.

7.4.2.1 UC EXAFS

UC data and fits in k-space are shown in Figure 7.2. Data analysis revealed that the UC samples were actually a mixture of UC and some UO_2 impurities, corroborating previous XRD results [5]. While spectra for UC-7 and UC-8 are similar, UC-9 shows some differences, including a slight phase shift. Fourier transforms of the spectra highlight these differences (Figure 7.3). Coordination numbers for the U-U bond in the UC lattice are all below the expected N=12, at about N=6 for UC-9 and N=8 for UC-7 and UC-8 (Table 7.1). High disorder in the U-O bonds in the UO_2 phase is indicated by the large σ^2 values. Other elements are therefore probably contained in the shell fit for the U-O bond. The extended length of the bond in UC-7 and UC-9 corroborates this. A deconvolution of the fit for UC-7 shows the contribution of each shell in the overall Fourier transform (Figure 7.4)

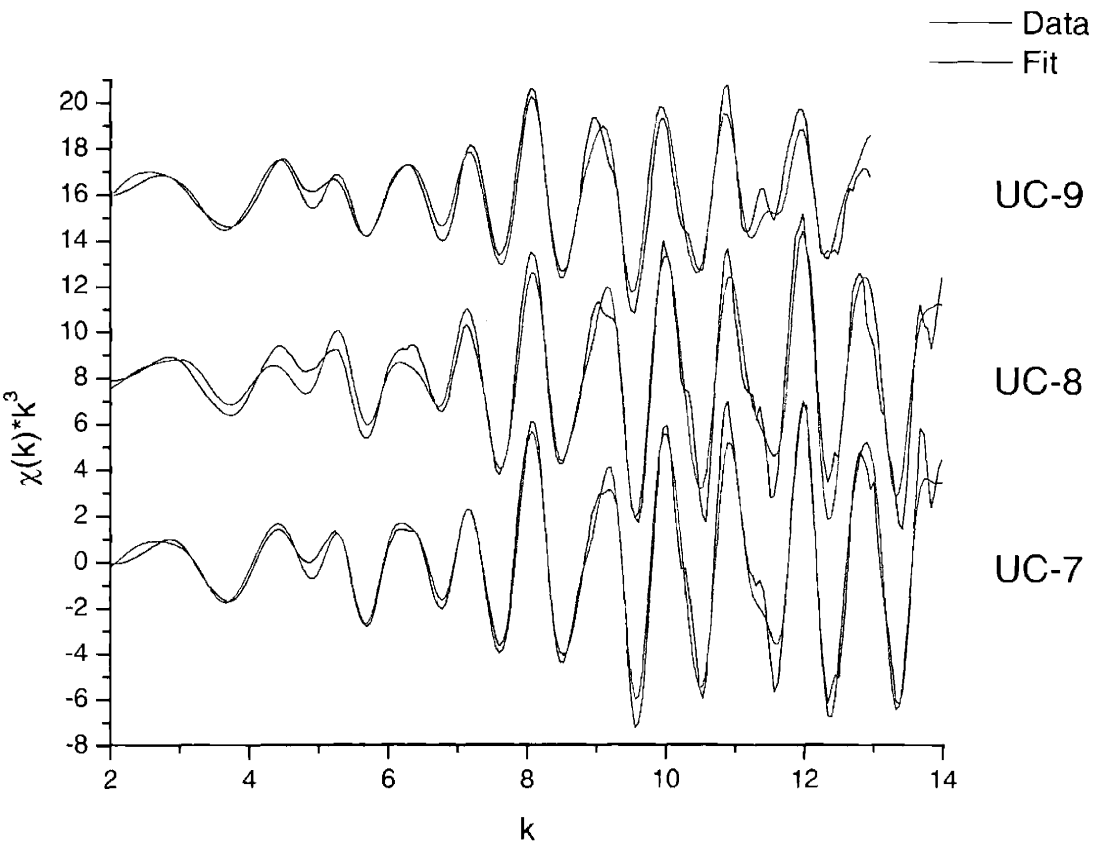

Figure 7.2. UC L_3 edge EXAFS data and fits.

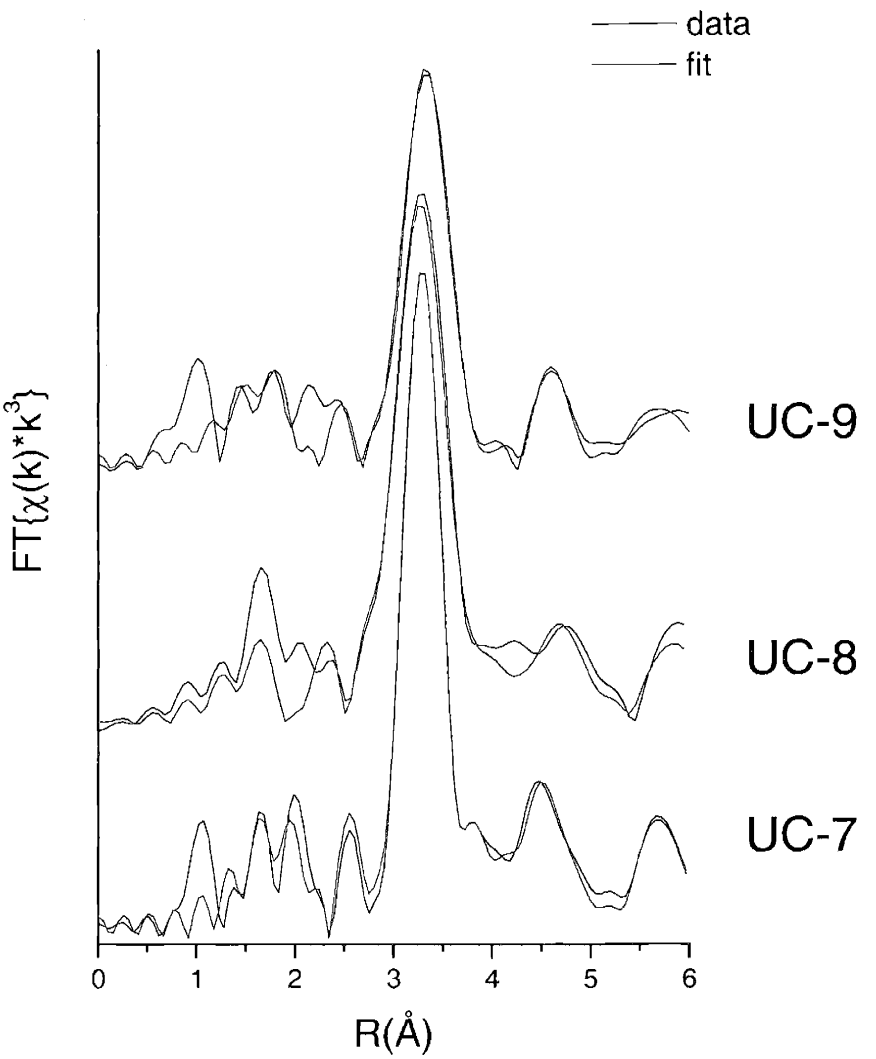

Figure 7.3. Fourier transforms and fits of UC samples. Varying amounts of UO_2 impurity can be seen in each.

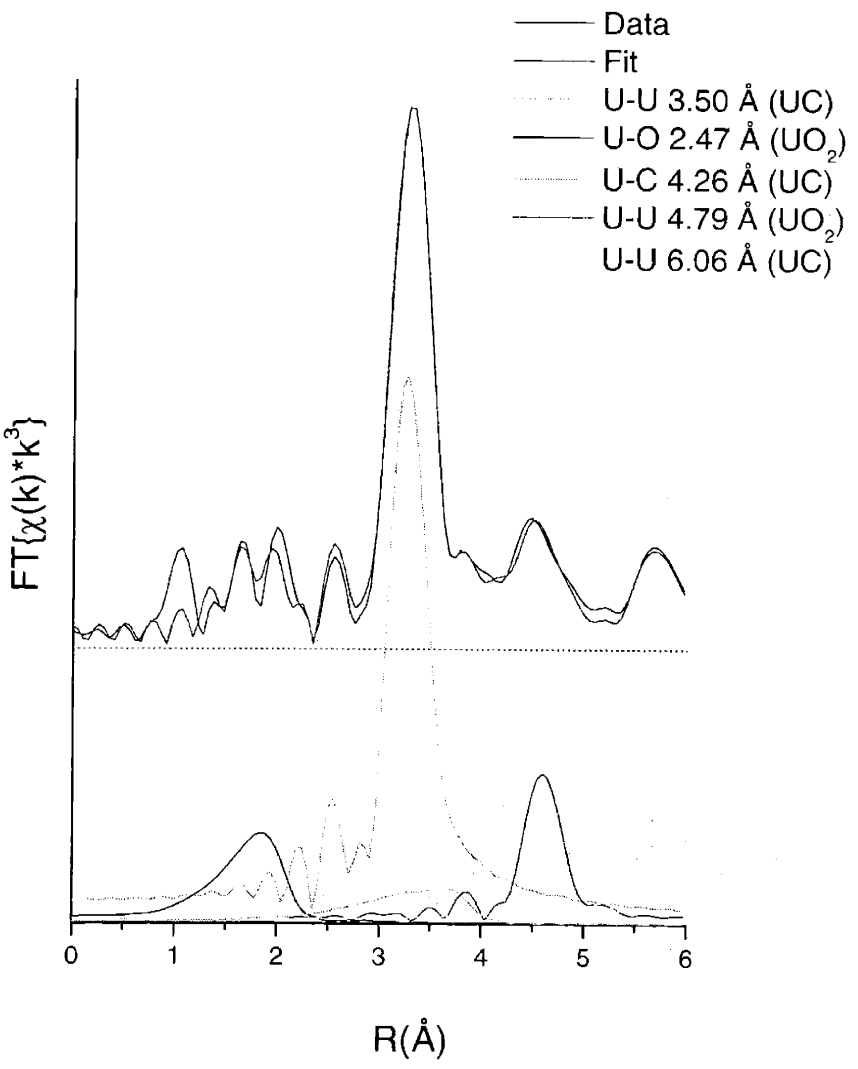

Figure 7.4. Components of fit to UC Fourier transform. Fit shows a mixture of UC and UO_2.

Sample	Phase	Bond	N	R(Å)	σ^2
UC-7	UC	U-U	7.5	3.50	0.00368
		U-C	19	4.26	0.00977
		U-U	5.8	6.06	0.00238
	UO_2	U-O	7.8	2.47	0.01202
		U-U	4.0	4.79	0.00355
UC-8	UC	U-U	8.1	3.51	0.00427
		U-C	29.8	4.24	0.01659
		U-U	5.6	6.06	0.00303
	UO_2	U-O	5.4	2.37	0.01679
		U-U	2.9	4.80	0.00297
UC-9	UC	U-U	6.4	3.51	0.00523
		U-C	22.6	4.26	0.00451
		U-U	3.6	6.07	0.00200
	UO_2	U-O	11	2.47	0.02418
		U-U	3.5	4.78	0.00664

Table 7.1 Coordination numbers and bond lengths calculated from fits of UC data.

7.4.2.2 UC/US EXAFS

Analysis of the mixed Uranium carbide and uranium sulfide solid solutions revealed obvious differences in structures. Data and fits in k-space are shown in Figure 7.5. Contributions of the UC and US phases can be clearly identified in the Fourier transforms (Figure 7.6). The UC concentrations are identified by the expected amount. The peak of the first U-S shell dramatically decreases in magnitude as the UC content increases. Likewise, the U-U peak at 3.5 Å from the UC phase appears much more prominent at the highest expected UC concentration, though it is not obvious at the two lower concentrations. Deconvolutions of the Fourier transforms of each sample show the contributions of each shell to the total spectra (Figures 7.7-7.9).

Coordination numbers for the U-S bond decrease with increasing expected UC content, indicating that the trend in UC/US concentrations followed the anticipated trend from the synthesis process, though actual concentrations differ [Table 7.2]. By comparing the coordination numbers from fitting with the expected N=8 from the NaCl-type structure of US, actual concentrations are calculated to be 66%, 38%, and 21% US, while the expected concentrations are 75%, 50%, and 25%, respectively. This comparison is more qualitative than quantitative by nature, however.

Identification of the UC portion of each spectra relied on fitting the most prominent shell of the UC structure, the U-U contribution at 3.5 Å. This shell did not appear in the 25% UC sample, though it could be masked by the nearby 3.87 Å U-U shell from the US phase. In the 50% UC sample, the increase in the distance to the 3.5 Å U-U shell and corresponding decrease in the radius of the 3.88 Å U-U shell were likely caused by the proximity of the features in the spectra rather than actual physical effects. The contribution of UO_2 to each spectrum increased with increasing UC concentration, indicating the origination of the impurity is probably in the UC fabrication process.

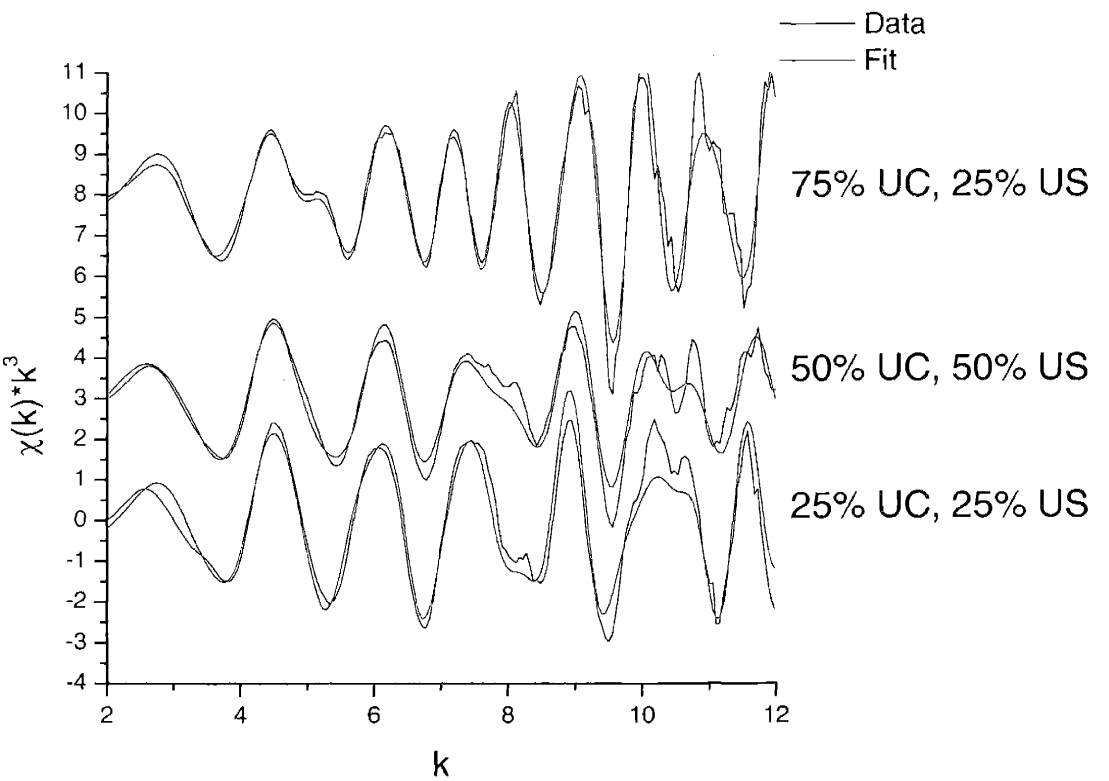

Figure 7.5 k^3 weighted EXAFS data and fits for UC/US solid solutions.

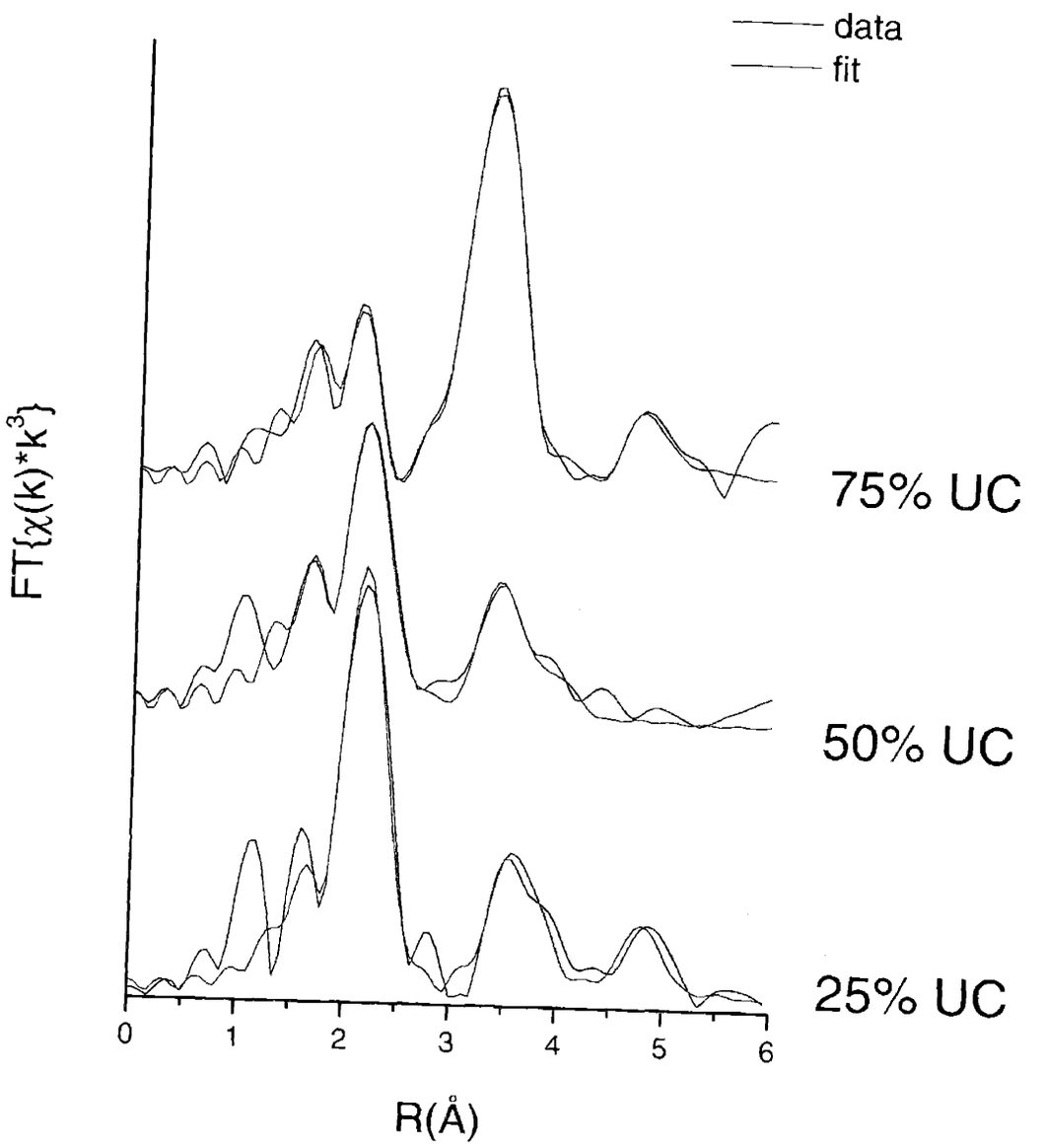

Figure 7.6. Fourier transforms and fits of UC/US data. Mixtures given in %UC, balance is US and UO_2.

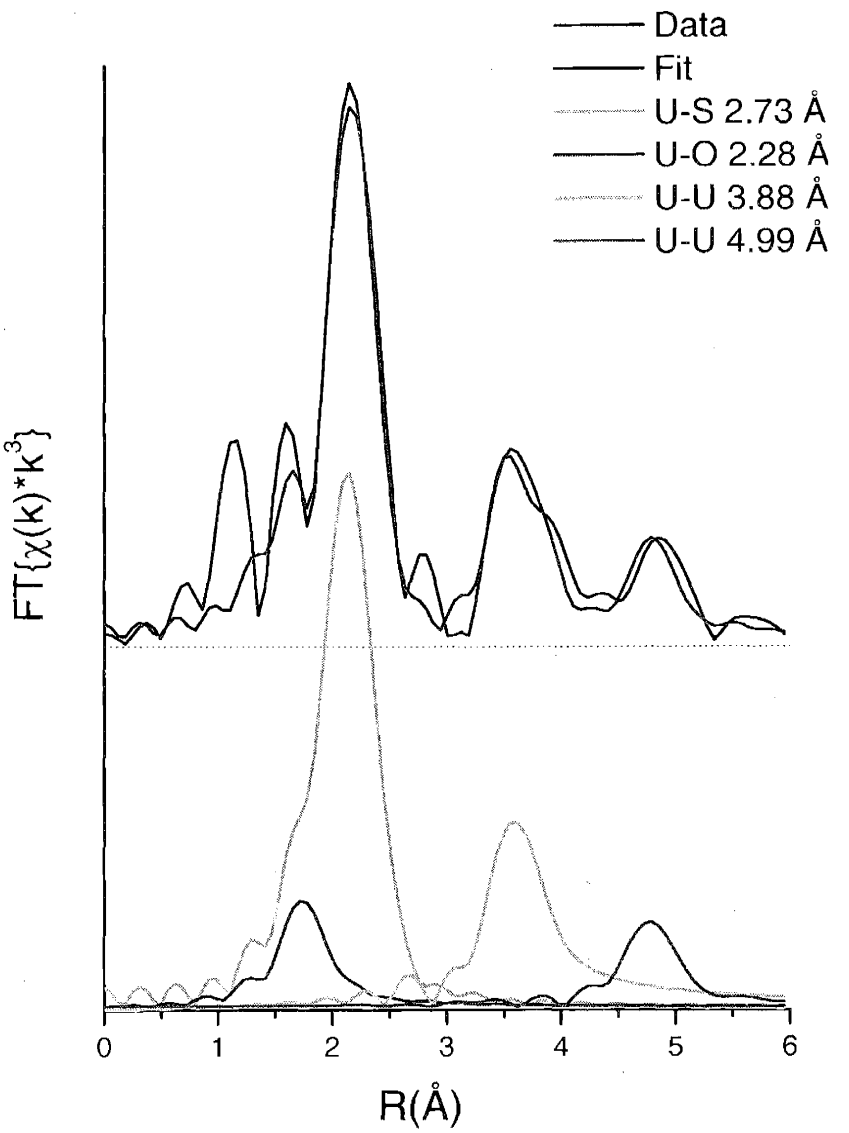

Figure 7.7 Deconvolution of Fourier transform fit of 25% UC sample. US is the primary phase, UO_2 secondary.

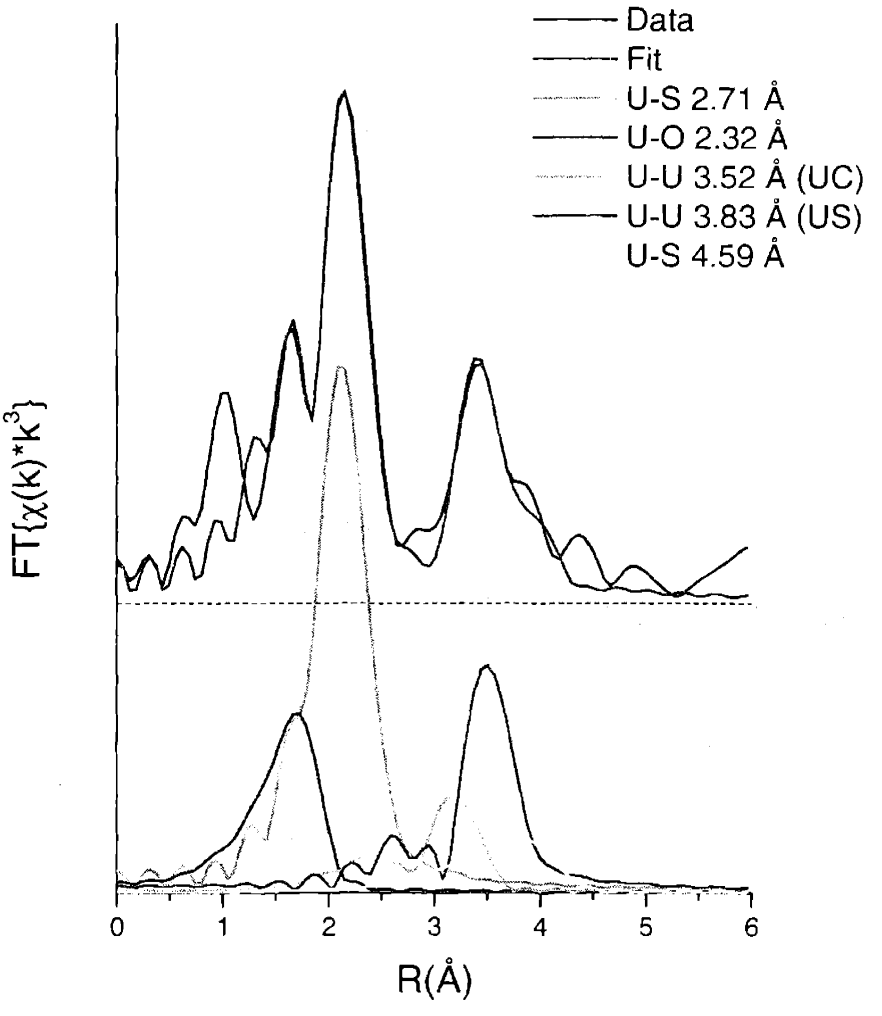

Figure 7.8 Deconvolution of Fourier transform fit of 50% UC sample. US is the dominant phase, followed by UO_2 and UC.

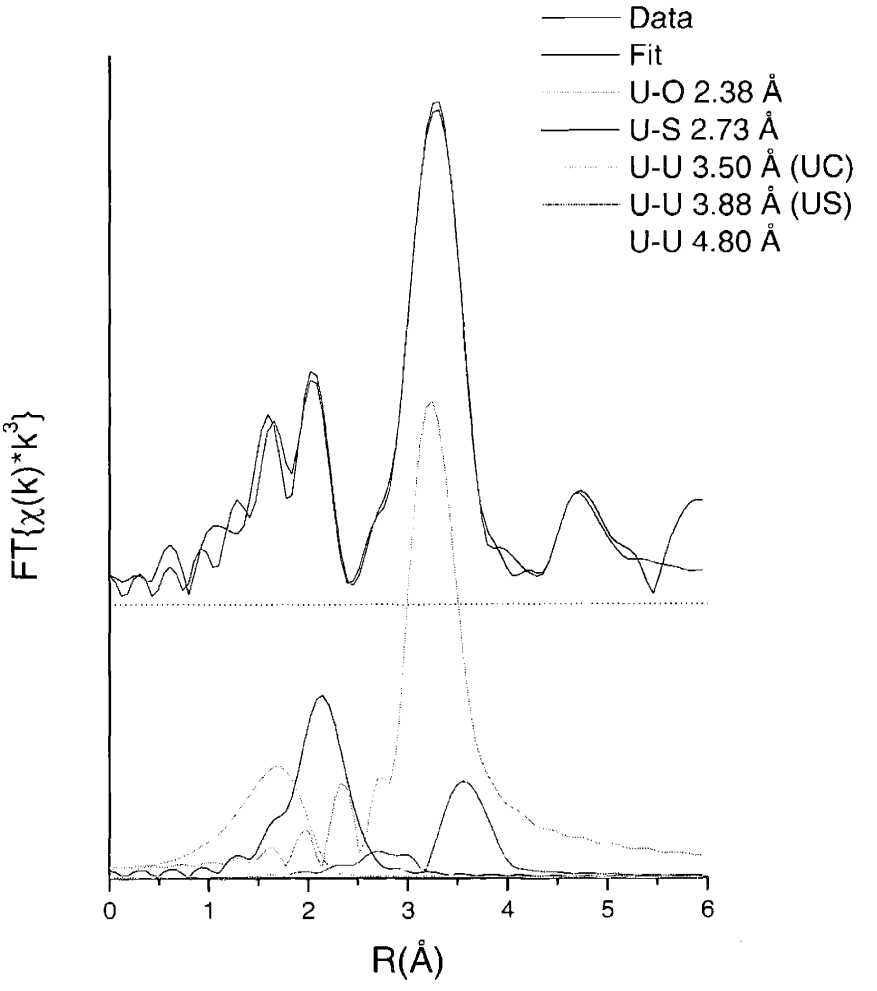

Figure 7.9 Deconvolution of fit of 75% UC data. Fit is a mixture of UC, US, and UO_2 phases, with UC the dominant phase.

Sample	Phase	Bond	N	R(Å)	σ^2
25% UC	US	U-S	5.3	2.73	0.00789
		U-U	1.4	3.88	0.00196
	UO_2	U-O	0.6	2.29	0.00193
		U-U	1.2	4.99	0.00300
50% UC	US	U-S	3.0	2.71	0.00622
		U-U	3.4	3.83	0.01096
		U-S	4.8	4.59	0.01401
	UC	U-U	2.8	3.52	0.01463
	UO_2	U-O	2.1	2.32	0.01096
75% UC	US	U-S	1.7	2.73	0.00712
		U-U	3.0	3.88	0.01031
	UC	U-U	3.8	3.50	0.0035
	UO_2	U-O	3.8	2.38	0.01996
		U-U	1.3	4.80	0.00188

Table 7.2 Coordination numbers and bond lengths calculated from fitting UC/US data.

7.5 Conclusions

The process used for fabricating UC and mixed UC/US solid solutions should be examined for potential improvements. Uranium dioxide contamination was found in all samples. Significant variations in structure were seen between the UC samples from different batches, indicating further need to refine and homogenize the process for synthesizing UC.

Analysis of the mixed UC/US samples showed that the trend in UC concentration was as expected from the synthesis processes, but the actual composition was not. Contributions from the US and UC phases could be clearly seen varying with composition. Interactions between close U-U shells from the UC and US phase caused difficulty in analyzing the lower concentration UC samples, with no obvious contribution from the UC phase in the lowest concentration sample in the spectra. In addition, in the mixed UC/US matrix, the amount of UO_2 impurity increased with the amount of UC present. This indicates that the source of the contamination is the UC portion of the fabrication process.

7.6 References

1. Dostal, Vaclav; Driscoll, Michael J.; Hejzlar, Pavel; Todreas, Neil E., Supercritical CO2 gas turbine power cycle for next-generation nuclear reactors. *ICONE 10, Proceedings of the International Conference on Nuclear Engineering, 10th,* Arlington, VA, United States, Apr. 14-18, 2002, 2 (567-574)
2. Murbach, E.W., Turner, W.D., Oxidation of Uranium Carbide by Carbon Dioxide, *NASA Doc.* N63-11826, 1962.
3. Lovell, G.H.B., Van Tets, A., Potential Nuclear Fuels in the US-UC-UC_2 System, *Journal of Nuclear Materials,* 1979, 79 (277-301)
4. Lovell, G.H.B., Van Tets, A., Britz, E.J., Preparation of some US-rich solid solutions in the UC-US system, *Journal of Nuclear Materials,* 1974, 51 (337-342)
5. Plaue, Jonathan Thesis, Massachusetts Institute of Technology, June 2003.
6. Mukerjee, S.K., Dehadraya, J.V., Vaidya, V.N., Sood, D.D., "Kinetics and mechanism of UO_2 + C reaction for UC/UC_2 preparation," *Journal of Nuclear Materials* 210, 107-114 (1994).
7. http://www.webelements.com/webelements/elements/text/U/comp/html

8 Application of XAS to Nuclear Chemical Engineering

8.1 Abstract

The speciation of actinides in two distinct materials that can affect the impact of radionuclides in the environment was determined using x-ray absorption spectroscopy. The first set of materials evaluated were actinide-imprinted resins synthesized by a polymerization technique. The resins are designed to selectivity for separation of specific actinides. The structure of thorium, uranyl, and samarium imprinted resins was examined. Samarium was used as a homolog for americium and curium. Resins were evaluated for both structure and reusability. Results showed the resin structures were as expected. In addition, structures did not change following actinide removal and resorption, indicating that the resins are reusable to some extent.

The method of uranium sorption to the metal reducing bacteria *Shewanella oneidensis* was also examined. By reducing uranium in the environment from the highly soluble species U(VI) to the rather insoluble U(IV), *S. oneidensis* and similar bacteria could significantly hinder the migration of uranium in the biosphere. Results showed that the uranium was attached to a phosphate group. Further studies are needed to determine if the interaction is external to the cell or via phosphate groups attached through the cell wall.

8.2 Actinide templated resins

8.2.1 Introduction

To create greater selectivity for the target ion in separation processes, molecularly imprinted resins were synthesized by way of a polymerization technique. Uranyl and thorium templated resins have shown fast kinetics and good separation efficiencies in previous studies. Lanthanides have also been used as homologs for americium and curium. The structures of uranyl, thorium, and samarium-imprinted resins were investigated in this study. Nontemplated samples were synthesized with no metal present and did not undergo the polymerization process.

8.2.2 Background

There is a desire to develop simple, fast, and accurate separation techniques and methods for actinides, both for analytical and potentially industrial purposes. Solid-liquid extractions are superior to the industry standard liquid-liquid approach because they provide a reusable binding source that is incinerable and does not produce by-products. Recent work in the area of solid-liquid actinide separations has been mainly involved in the development of resins with phenolic-based functional groups. These resins had slow kinetics, which was the large reason that this work examines carboxylic acid type functionality resins. A technique knows as molecular, or ion, imprinting was also implemented in the synthetic process. By imprinting resins, potential binding sites are tailored for the target metal in terms of both ion size and charge, thereby increasing efficacy. Although this technique has been widely applied for a number of applications, there has been little use with the lanthanides and actinides.

The concept of molecular-imprinted polymers was developed more than 20 years ago [1,2] and shows a potential for applications in analytical chemistry [3-7]. The technique of molecular imprinting can be used for the production of selective ion exchange resins. Both simple organic compounds and polymers have been created using these methods in order to separate lanthanides [8] and actinides [9]. The more traditional simple organic compounds utilized functional groups such as phenols, resorcinol, and catechol. The problems with these previous resins include slow kinetics and difficulty with creating a molecularly imprinted product. This lead to the investigation of templated resins with carboxylic functional groups.

8.2.3 *Experimental*

To synthesize each resin, the metal was added, while stirring, to a mixture of methacrylic acid ($C_4H_6O_2$, 15.80 mmol, 1.36g) in dichloromethane (CCl_2H_2, 450 mL) as a nitrate with triethylamine ($C_6H_{15}N$, 32.28 mmol, 4.5 mL) drop-wise. This reaction mixture was stirred at 40 °C for 2 hours under reflux. Ethylene glycol dimethacrylate ($C_{10}H_{14}O_4$, 59.13 mmol, 11.72 g) was added along with azobisisobutyronitrile (AIBN, $C_8H_{12}N_4$, 8.28 mmol, 1.36 g). The reaction mixture was heated to 60 °C (space between number and unit) and kept at this temperature overnight while stirring under reflux.

After evaporation, the resulting solid was ground and sieved to a particle size of 63-125 μm. To remove the template metal, 5 M nitric acid (30 mL) was added and the mixture was sonicated for 15 min. After filtration, the resin was then washed thoroughly with water until neutral, rinsed with ethanol, and kept at 60 °C in an air oven to cure for 2 days. Nontemplated resins were synthesized using the same procedure, except the metal and triethylamine were withheld.

Several resin samples were prepared for each ion, including templated and nontemplated resins. In addition, to assess the reusability of the resins, the ion was removed from some templated resins and later reabsorbed. 50 mg samples of loaded resins were ground and mixed in a 200 mg inert matrix and placed in an Al window. The samples were analyzed at the U and ThL_3 edges and the Sm K-edge. Data was taken in transmission mode using ionization chambers. Oxide standards for each element were simultaneously scanned for calibration.

8.2.4 Results

The uranium loaded resins are uranyl (UO_2^{2+}), as expected. XANES spectra showed the uranium contamination found in the thorium resin is U(IV), indicating that the contamination was in the thorium stock (Figure 8.1). EXAFS analysis of this sample was also consistent with UO_2 (Figure 8.2 and 8.3). The resin structure is consistent with the proposed structure shown below (Figure 8.4). A deconvolution of the EXAFS fit is shown in Figure 8.5.

Fits of the thorium-loaded resins revealed small changes in the Th-Th and Th-O bond lengths between the templated and nontemplated resins (Table 8.1). A deconvolution of the thorium fits is shown in Figure 8.6.

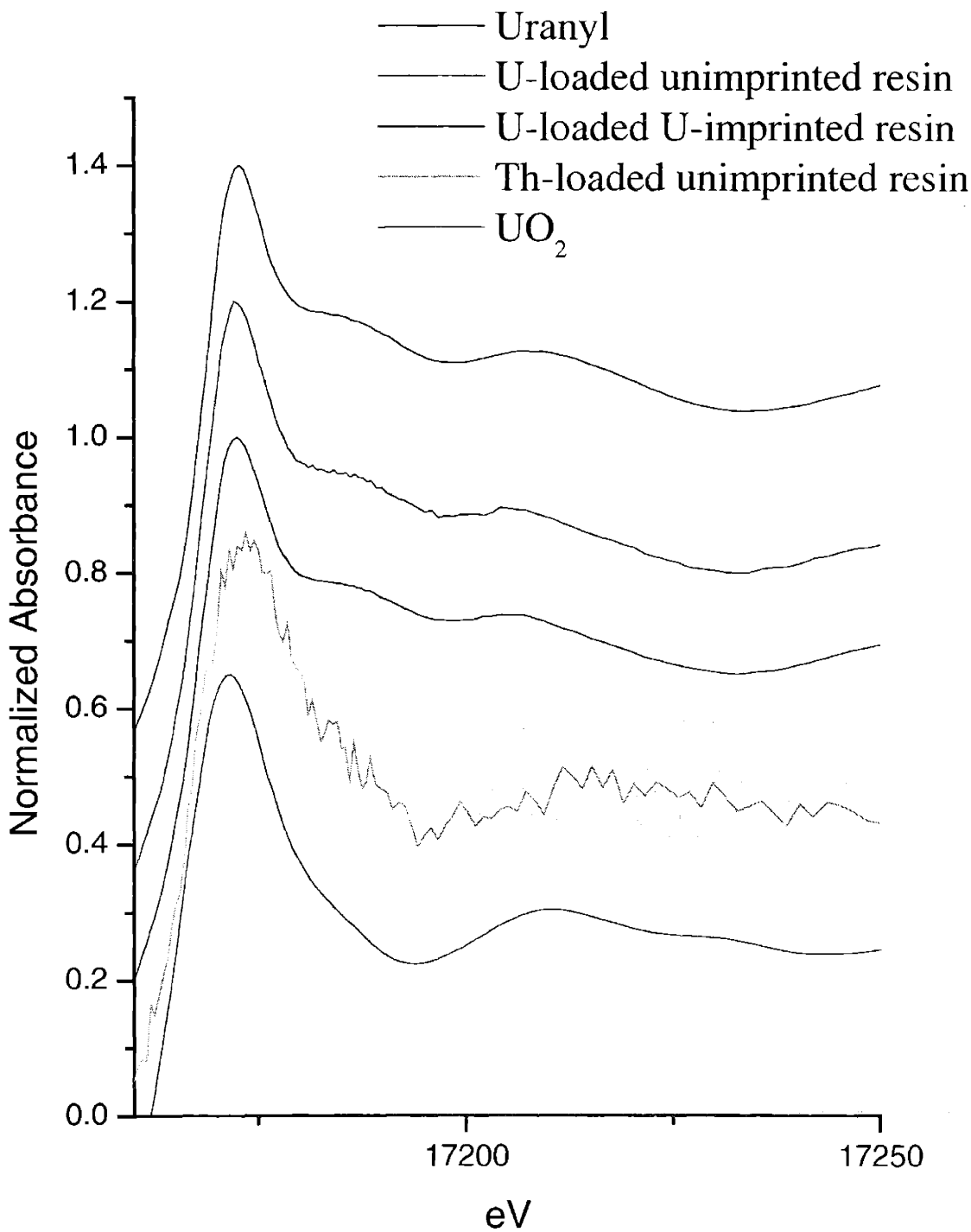

Figure 8.1. Uranium L3 XANES. Note the Th-loaded sample. This is from contamination in the sample. Even though quite dilute, the signal is clearly consistent with U(IV).

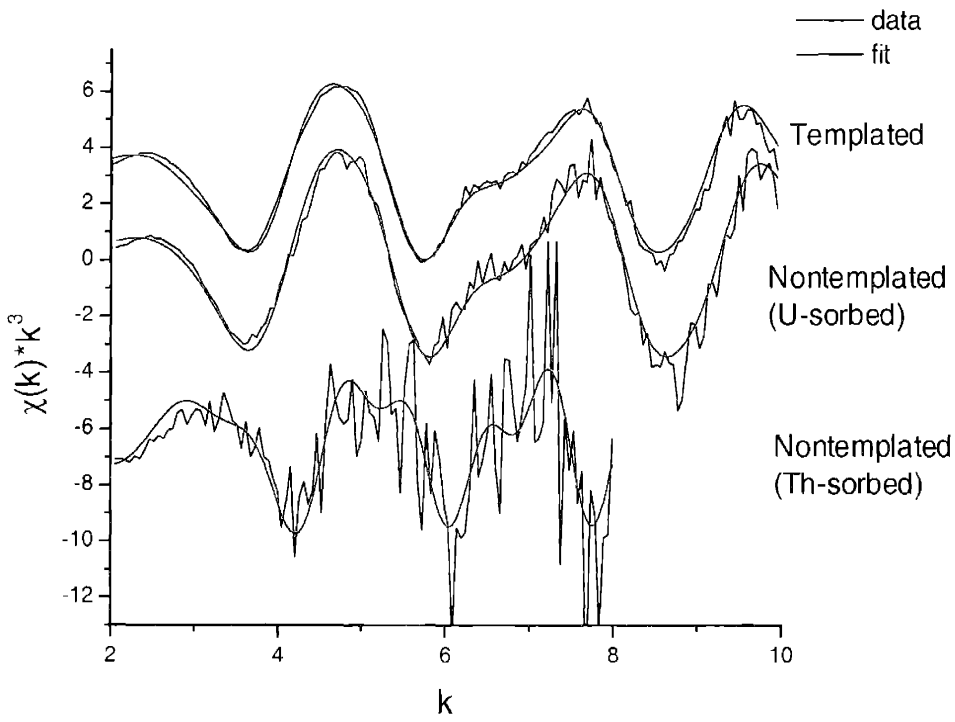

Figure 8.2. EXAFS data and fits. Once again, the Th-loaded sample is quite different. The phase shift of the first peak is also indicative of U(IV).

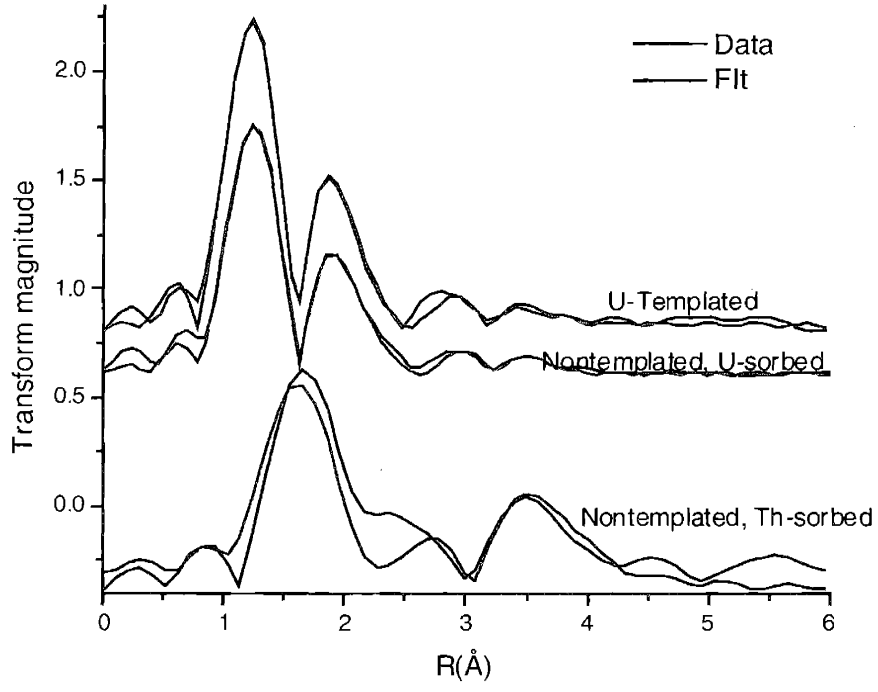

Figure 8.3. Fourier transforms of EXAFS data. The U-O bond length for UO_2 is significantly longer than the U=O axial bonds in uranyl.

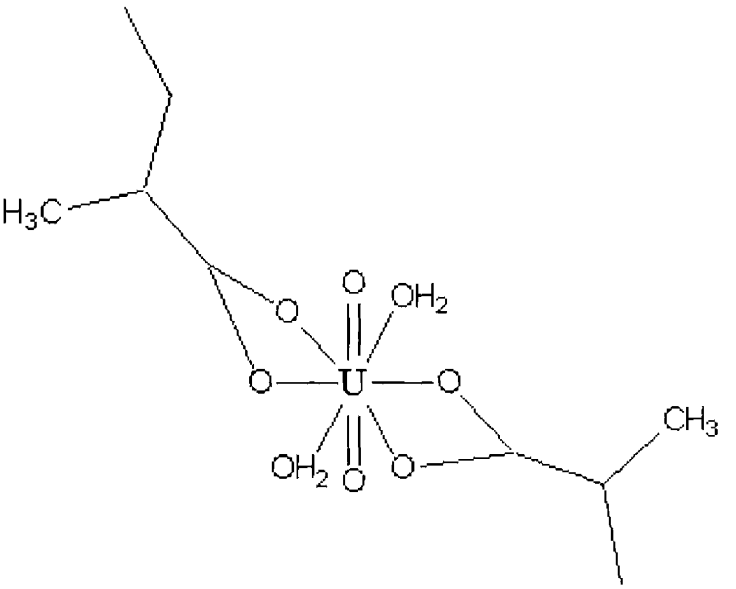

Figure 8.4. Expected Uranyl-templated resin structure. This is a small segment of the polymer chain.

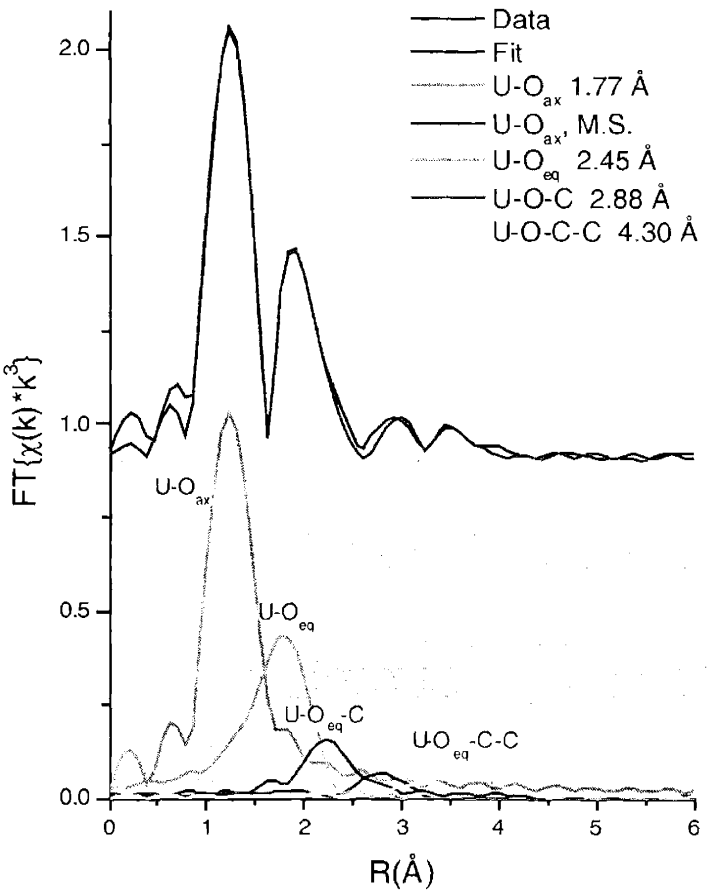

Figure 8.5. Deconvolution of the Uranium-templated nonreleased sample fit.

Sample	Bond	R(Å)
Templated (nonreleased)	Th-O	2.42
	Th-Th	3.92
Templated (reabsorbed)	Th-O	2.42
	Th-Th	3.93
Nontemplated (Th sorbed)	Th-O	2.44
	Th-Th	3.90

Table 8.1. Thorium resin bond lengths

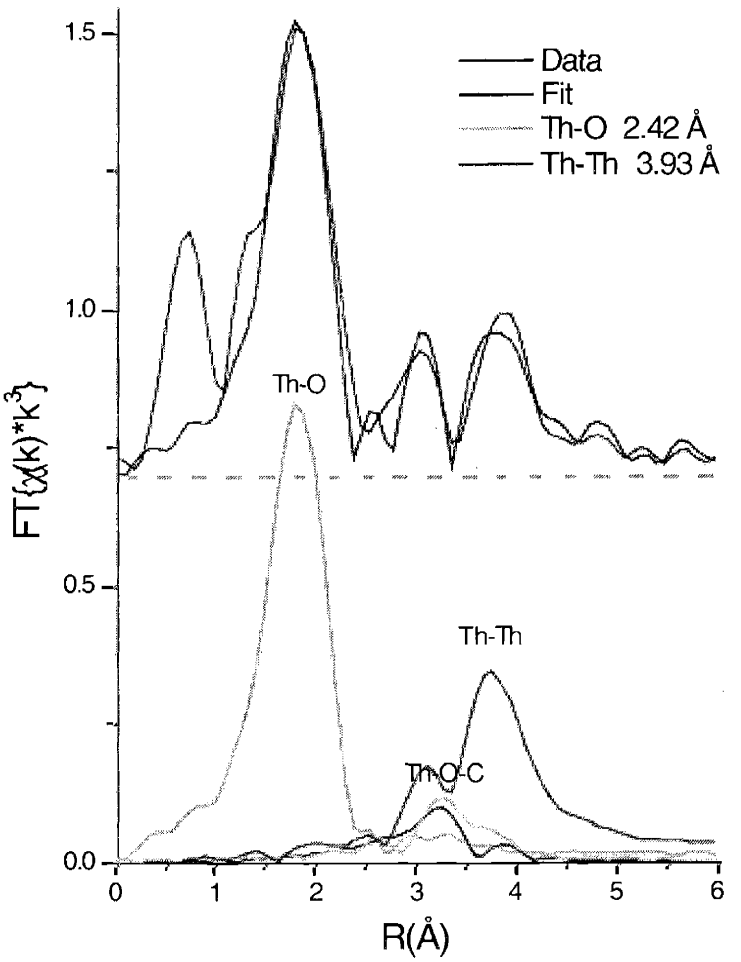

Figure 8.6. Deconvolution of the templated thorium fit. The results for the three resins were very similar.

The samarium-loaded resin samples were scanned to k=9, limiting analysis to the first shell. However, differences in the structures of the templated and nontemplated resins can still be seen. XANES spectra show no change in oxidation state between the samples. EXAFS oscillations of the nontemplated sample are slightly shorter wavelength, indicating lengthening of the Sm-O bond (Figure 8.7). These differences can also be seen in the Fourier transforms of the EXAFS spectra (Figure 8.8). Sm-O bond lengths are given in Table 8.2.

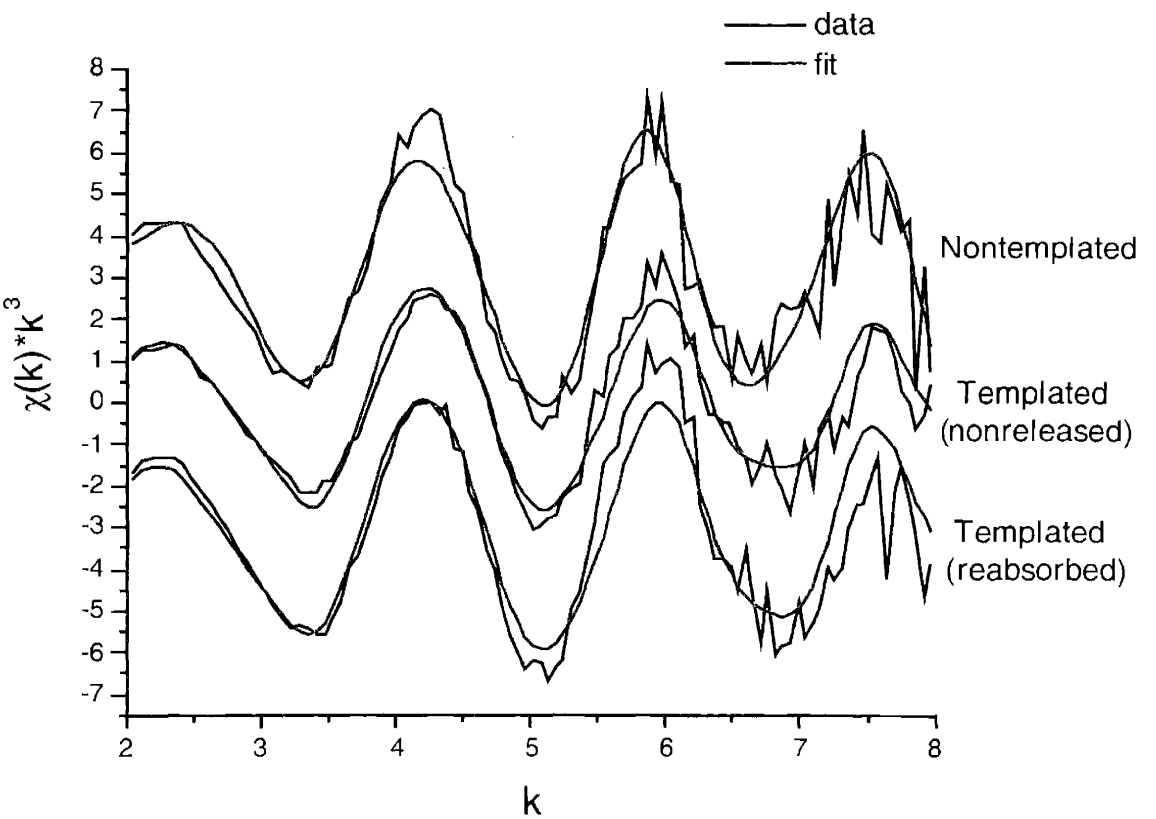

Figure 8.7. Samarium L_3 edge EXAFS and corresponding fits. Note the slightly higher frequency oscillations of the nontemplated resin.

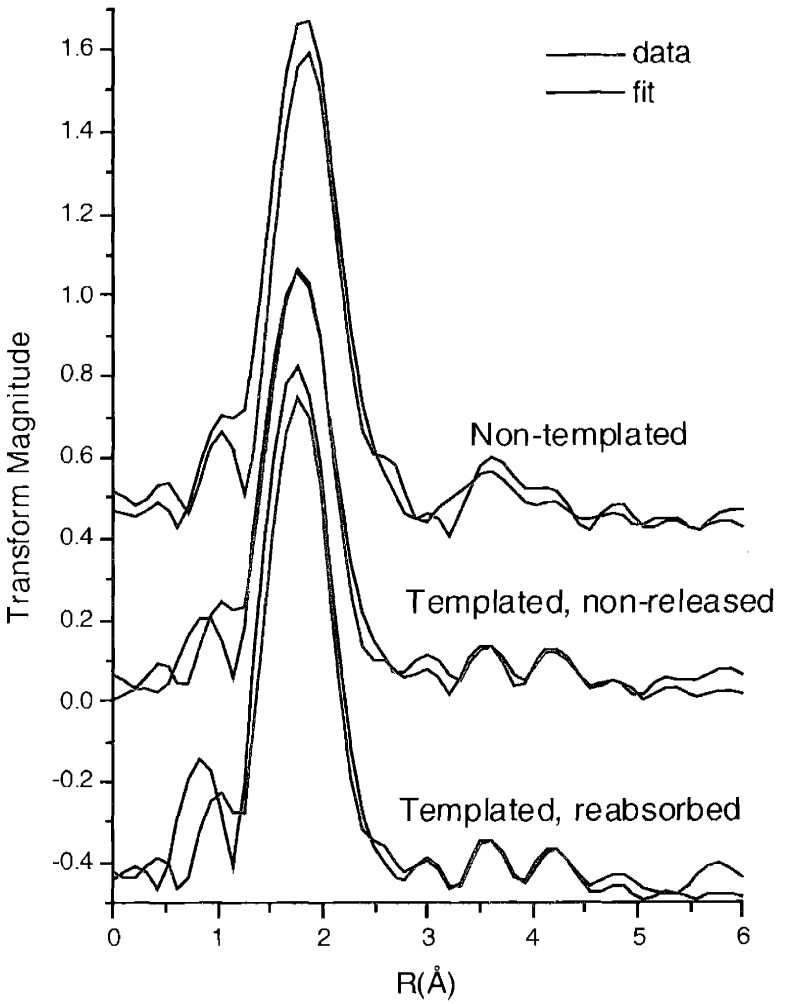

Figure 8.8. Fourier transforms of the samarium data and fits. Note the nontemplated peak is shifted slightly to the right.

Sample	R(Sm-O), Å
Nontemplated	2.48
Templated (nonreleased)	2.43
Templated (reabsorbed)	2.43

Table 8.2. Sm-O bond lengths

8.2.5 *Conclusion*

Analysis of the resin structures shows that there is a significant difference between the templated and nontemplated resins. These differences can be used to further explain differences in sorption abilities of the resins, as well as aid in refining the production of future ion-templated resins. No difference in structure was found between templated non-released and templated reabsorbed resins, indicating at least a minimal reusability of the resins. In addition, a previously unknown uranium contamination source was discovered.

8.3 Uranium reducing bacteria

8.3.1 Introduction

The bacteria *Shewanella oneidensis* is a widely distributed species known to utilize several elements such as iron, manganese and sulfur as electron acceptors. In an anoxic environment, S. oneidensis can also use uranium, reducing its oxidation state from hexavalent to tetravalent, by the following reaction:

$$H_2 + U(VI) \rightarrow 2H^+ + U(IV) \qquad \text{Equation 8.1}$$

Tetravalent uranium (UO_2) is insoluble, and the reduction reaction is a favorable one. Uranium in this state will tend to remain immobile in soil, while the more soluble hexavalent uranium will dissolve, leading to an increase in area of contamination. XAS studies of uranium exposed bacteria were conducted to determine the location and manner of the interaction between the bacteria and the uranium.

8.3.2 Background

The metal reducing soil bacterium *S. oneidensis* is known to metabolize several different metals including uranium [10]. In an anoxic environment S. oneidensis will reduce soluble uranium(VI) to uranium(IV), which is insoluble at a wide range of pH. Uranium in its insoluble form is much less mobile and reactive in soil and groundwater and microbially mediated reduction of uranium would help to sequester uranium at the site of contamination. It has been suggested that metal and sulfate reducing bacteria could be used for bioremediation of uranium contaminated soils [11].

8.3.3 Experimental

Shewanella oneidensis MR-1 (ATCC# 700550) is grown aerobically approximately 24 hours at room temperature in Tryptic Soy Broth (TSB). Cells are then concentrated by centrifugation and washed thoroughly with $NaHCO_3$ (2.5g/L) buffer. A 5mL solution of cells is then transferred into 100mL of sterile anaerobic bicarbonate buffered freshwater medium as described by Kuai et al. [12], with the following exceptions; phosphate was removed to prevent uranyl precipitation, the carbon source was 5mM lactate, and the electron acceptor was 4mM or 22 mM uranium. The cells do not grow in this media but remain metabolically active.

Cells were killed with a 10% formaldehyde solution and refrigerated. Samples were stored in epoxy-sealed Eppendorf centrifuge tubes. The precipitate that settled at the bottom of each sample was scanned on the uranium L_3 edge at room temperature in transmission mode using an ion chamber. A UO_2 standard was simultaneously scanned to calibrate the edge position of the data.

8.3.4 Results

Both the k^3 weighted EXAFS (Figure 8.9) and Fourier transforms (Figure 8.10) show a noteworthy difference between the two samples. While the 4 mM sample is a good example of uranyl phosphate, the 22 mM sample is a mixture of uranyl phosphate and uranium in an organic carbon structure, most likely uranyl acetate. Therefore, due to the high concentration of uranyl acetate present in the sample, the cells could not interact with all of it. A deconvolution of the 4 mM fit is shows the contribution of each shell to the total Fourier transform (Figure 8.11).

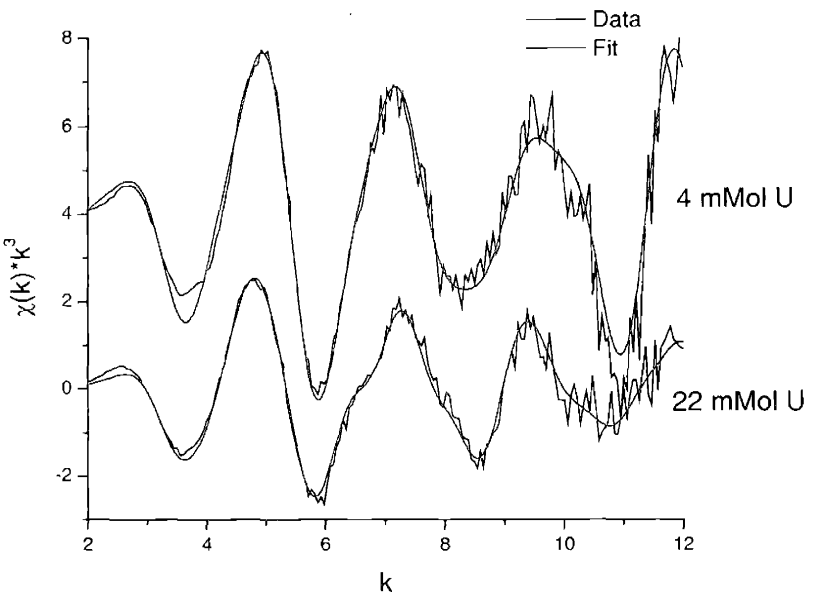

Figure 8.9. Uranium L_3 edge EXAFS spectra of bacteria samples and corresponding fits.

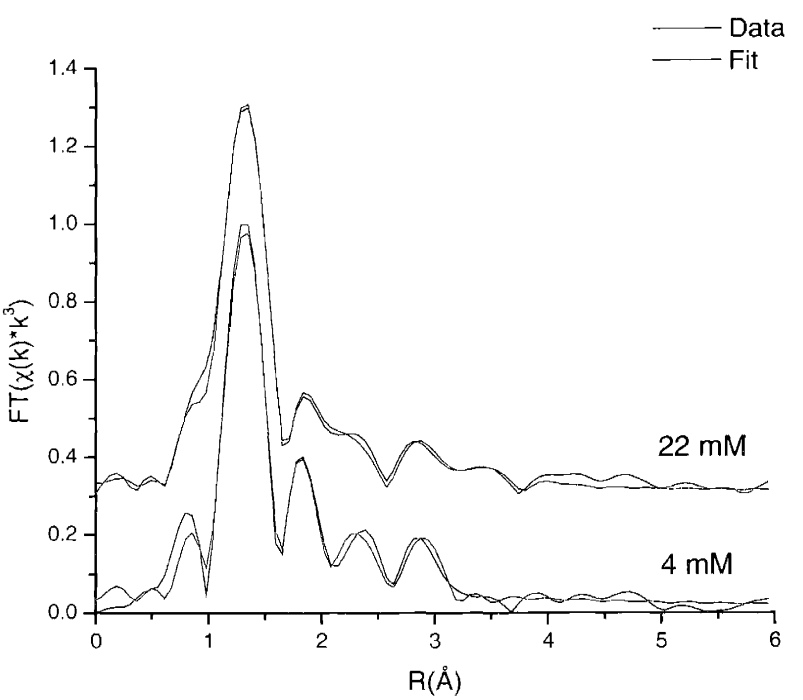

Figure 8.10. Fourier transforms of bacteria EXAFS, further emphasizing differences in the uranium environment.

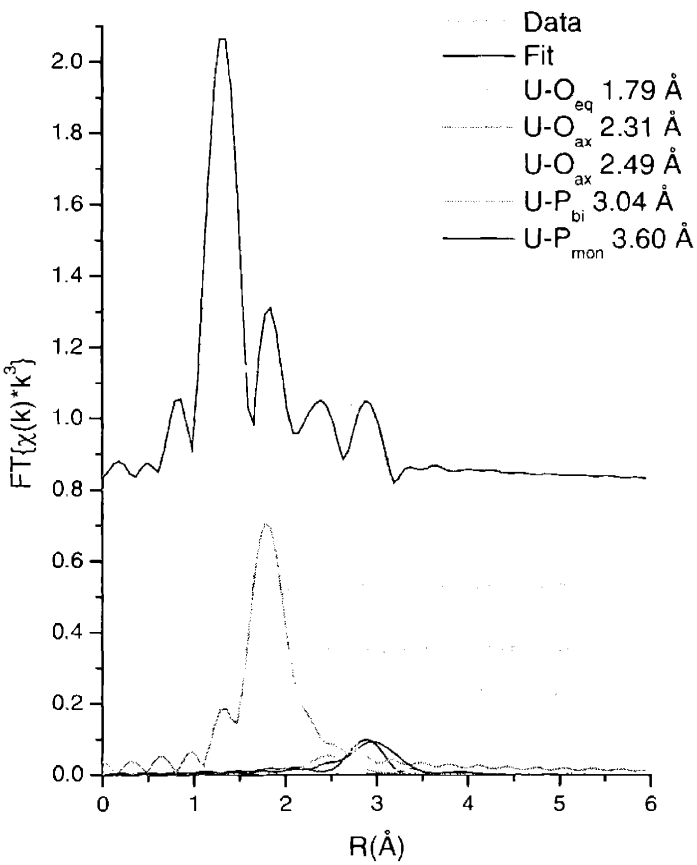

Figure 8.11 Deconvolution of 4 mM fit.

8.3.5 Conclusion

The method of interaction between the uranium and bacterium is through attachment to a phosphate group. However, it is possible that because the samples were kept at room temperature for over a week before scanning, this could be the inorganic phosphate released following cell lysis. Further analysis will need to be performed to determine the type of phosphate involved in this interaction.

8.4 References

1. G. Wulff, A. Sarhan, *Angew. Chem. Int. Ed. Eng.*, 1972, **11**, 341 ;
2. R. Arshady, K. Mosbach, *Makromol. Chem.*, 1981, **182**, 687-692
3. A. Sarhan, G. Wulff, *Makromol. Chem.*, 1982, **183**, 85-92 ;
4. G. Wulff, J. Haarer, *Makromol. Chem.*, 1991, **192**, 1329-1338
5. M. Kempe, K. Mosbach, *J. Chromatogr. A*, 1995, **694**, 3-13
6. B. Sellergren, M. Lepistö, K. Mosbach, *J. Am. Chem. Soc.*, 1988, **110**, 5853-5860
7. D. Spivak, M.A. Gilmore, K.J. Shea, *J. Am. Chem. Soc.*, 1997, **119**, 4388-4393
8. K. Uezu, M. Yoshida, M. Goto, S. Furusaki, *Chemtech*, 1999, 12-18
9. Saunders, G., Foxon, S., Walton, P., Joyce, M., and Port, S.: A Selective Uranium Extraction Agent Prepared by Polymer Imprinting. *Chem Commun.* 2000, **4**, 273-274.
10. D. R. Lovely, E. J. P. Phillips, Y. A. Gorby, E. R. Landa, *Nat.* **350**, 413 (1991).
11. L. L. Barton, K. Choudhry, B. M. Thompson, K. Steenhoudt, A. R. Groffman; *Radioact. Waste Manage. Environ. Restor.* **20**, 141 (1996).
12. Kuai, L., Nair, A., Polz, M.F., *Appl. Environ. Microbiol.* **67**, 3168 (2001).

9 Characterization of Uranium Speciation in a Heterogeneous Metallic Matrix

9.1 Abstract

Three metallic slag samples recovered from the site of their inadvertent creation several decades after the fact were sectioned and analyzed to determine uranium speciation to evaluate environmental behavior as well as assess proliferation resistance of the waste form. Uranium concentration in the highly inhomogeneous samples was up to 5% by weight as determined by gamma spectroscopy. Sample sections were milled in a hardened steel ball mill for x-ray absorption spectroscopy analysis (XAS). Powders were digested in a mixture of heated concentrated nitric acid and peroxide and analyzed for elemental content using ICP-AES and ICP-MS.

Though elemental content of the samples varied widely, high concentrations of Al were consistently found. Other metals of significance were Ti, Fe, Ni, Cu, Zn, and Sn. High Pb concentrations were occasionally found. XAS analysis revealed the two main phases present. Surface samples were a mixture of uranyl and a metallic uranium compound. The interior samples contained primarily the metallic uranium compounds, though in some cases small amounts of uranyl were also present. The metallic uranium compounds were identified as U-Al and U-Ti. The uranyl present on the surface is highly mobile, indicating low stability of the slags in the environment. In addition, the samples showed little proliferation resistance and could be dissolved with relative ease using commonly available chemicals.

9.2 Introduction

Three metallic slag samples recovered after an extended period of subsurface disposal were analyzed to determine uranium speciation and concentration variation. The results will be used to evaluate environmental behavior as well as assess proliferation resistance of the waste form. The three samples were created inadvertently when uranium-bearing containers were exposed to a fire. They consist of a mixture of various metals and local sedimentation exposed to high heat for a short duration of time. Evidence of residual firefighting chemicals as well as some vegetation was also present.

Subsamples were extracted from the interior and exterior of the three pieces. The speciation of the uranium was determined using x-ray absorption spectroscopy (XAS). The samples were also analyzed for elemental content using ICP-AES and ICP-MS. Sample descriptions are given in Table 9.1.

Sample	Mass (g)
Slag 1	259
Slag 2	882
Slag 3	517

Table 9.1. Uranium containing slag sample description

9.3 Experimental

Upon receipt, the three slags were washed to remove loose particles as well as organic matter that had integrated into the surfaces of the pieces during their lengthy environmental exposure. After cleaning, samples were obtained for elemental and XAS analysis by physically removing sections from various areas of the slags. The resulting samples ranged from hard metallic pieces to soft chips loosened from the

surface. The samples were massed, and then milled into a fine powder in a hardened steel ball mill chamber. Some of the samples could not successfully be ground using this method and were not included in this analysis. Uranium content of each sample was determined using a HPGe detector. Table 9.2 lists samples and uranium content. Uranium content varied widely with sampling location.

After milling, small amounts of each sample were dissolved in a heated mixture of concentrated HNO_3 and H_2O_2. Due to the widely varying heterogeneous compositions of the samples, a small amount of concentrated HF was added occasionally to assist the reaction. After digestion, samples were diluted to 10% HNO_3 with purified water.

9.4 Results

9.4.1 Elemental Analysis

A small array of dissolved samples was scanned using a FisonsVG Plasmaquad 2 ICP-MS in order to identify the elements of interest. Eleven metal ions were identified: Al, Ti, Fe, Ni, Cu, Zn, Ga, Nb, Sn, Pb, and U. All samples were then analyzed for elemental content using a Spectroflame ICP-AES. A series of multi-element standards containing the 11 elements of interest was created to calibrate the results. Concentration results varied widely among the samples. All samples contained significant quantities of aluminum. Sampling locations and elemental compositions for each slag are shown in Figures 9.1-9.3. To determine the relative concentrations of elements in each sample, the uranium results from ICP-AES analysis were correlated with the percent weights determined by gamma spectroscopy, as shown in Figure 9.4. Ratios of the metals present to uranium concentrations in each sample are given in Figures 9.5 and 9.6.

Sample	mass (g)	wt% U	Source
1-1	0.75	2.13	Top center-left, through "blue-ish" surface on front, bottom left
1-3	0.119	3.63	center
1-5	0.621	0.97	surface catchings
1-6	0.495	4.00	slight protrusion on bottom right front
1-7	1.07	0.81	Smaller bits loosened while chiseling off 1-6
2-1	0.976	5.15	tip at left edge, center
2-5	3.07	1.26	Surface bits loosened during chiseling
2-6	0.159	3.99	Bit from edge of hole chiseled in center left
2-7	0.855	0.48	center hole pieces loosened while chiseling
2-8	0.334	3.97	right top edge bit
2-11	0.435	3.52	back of middle lump
2-13	2.19	0.82	remaining bits loosened during chiseling
3-2	1.013	4.76	Powder/bits from surface
3-3	0.418	1.86	bits from rust-like surface chiseling
3-5	0.151	2.45	tip bit from middle top section
3-6	0.299	1.28	back middle surface (brown area)
3-7	0.137	2.04	Bottom rear protrusion (center-left)
3-8	0.394	0.09	front edge, left side, lower-center

Table 9.2. Sample list. Sample sets 1, 2, and 3 came from slags 1, 2, and 3 respectively. Samples that were too hard to mill were not included in this analysis.

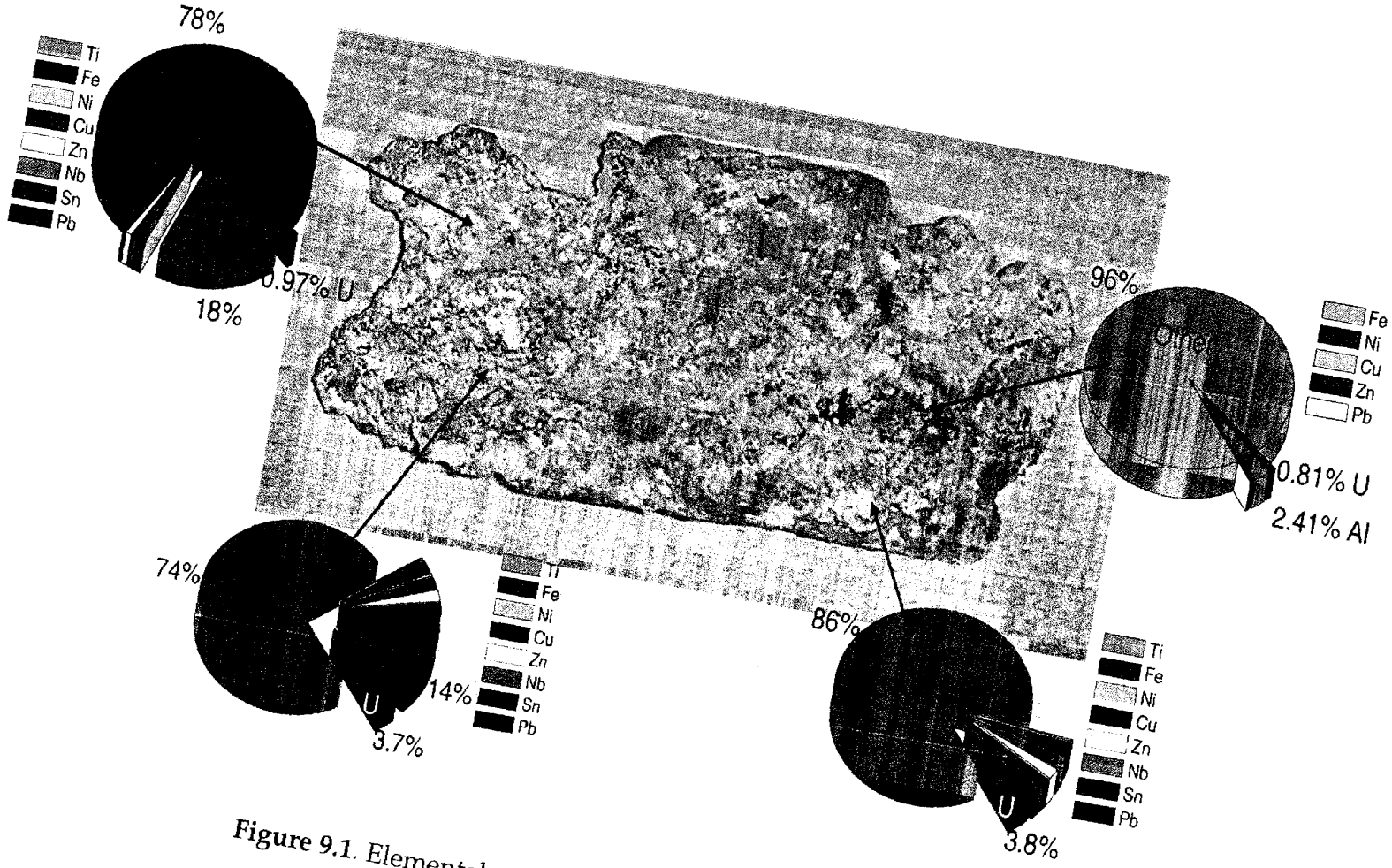

Figure 9.1. Elemental composition of various sectors of slag 1.

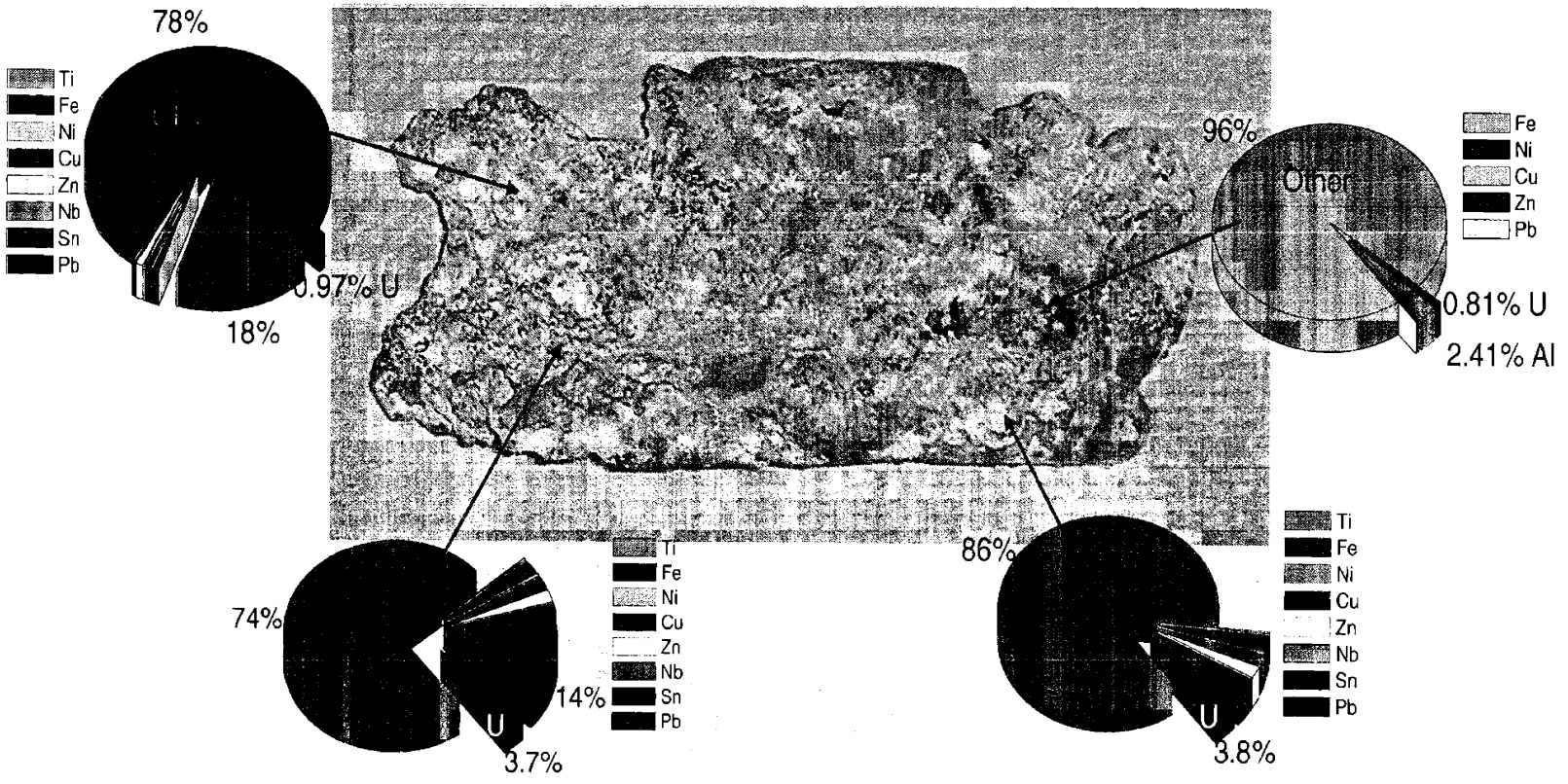

Figure 9.1. Elemental composition of various sectors of slag 1.

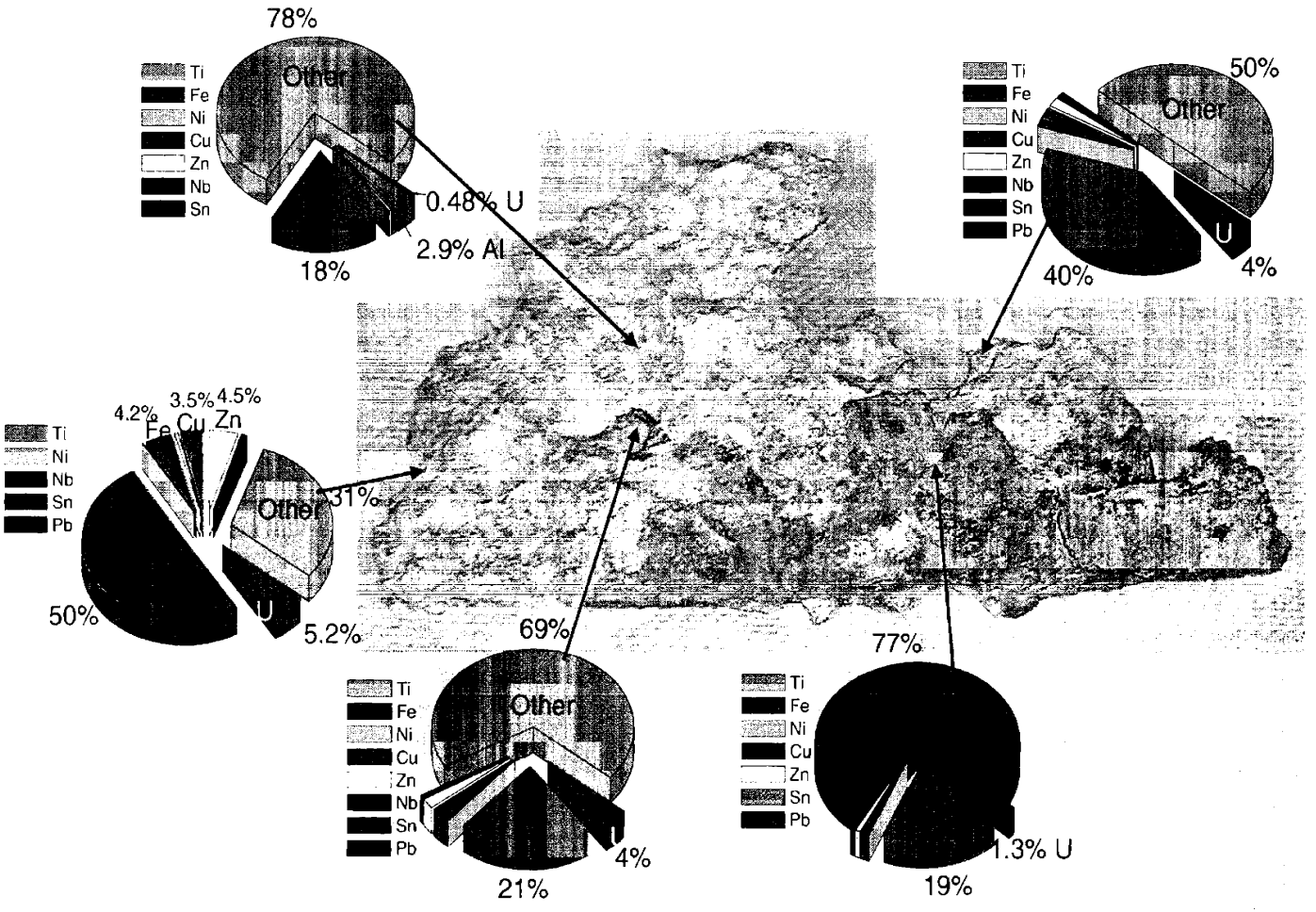

Figure 9.2. Elemental composition of various sectors of slag 2.

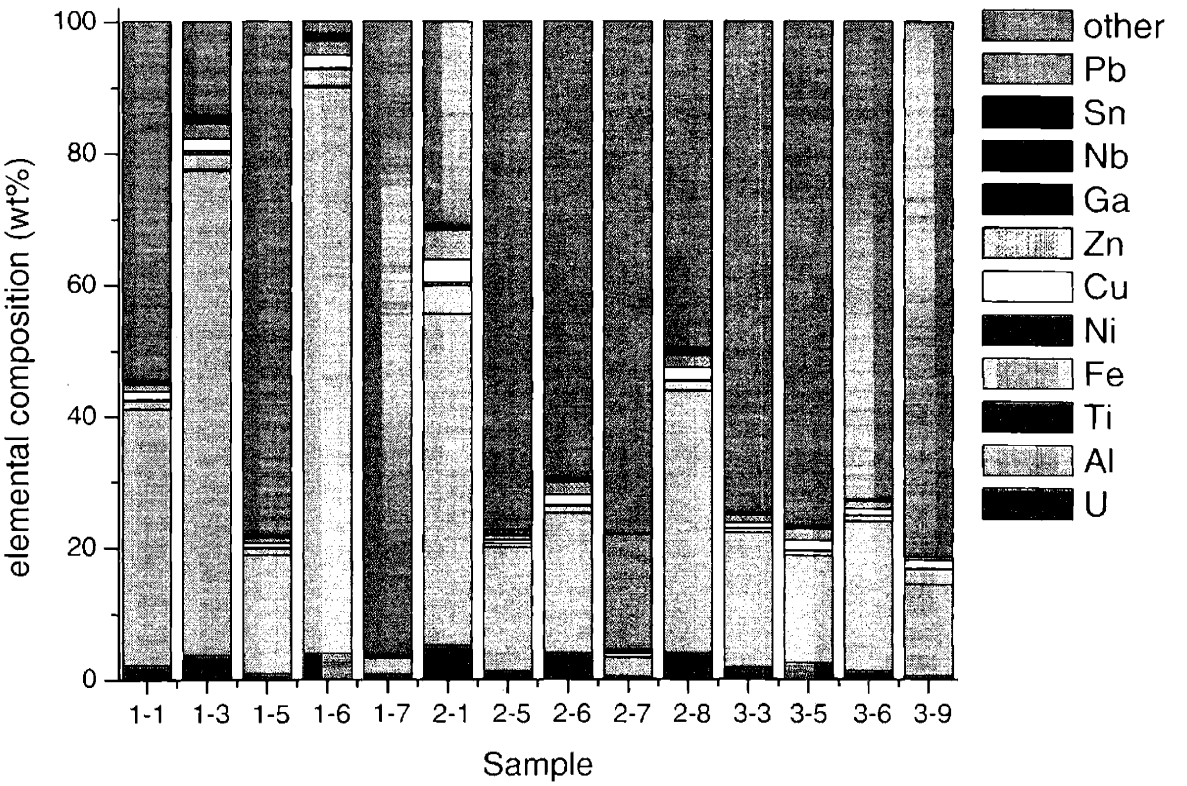

Figure 9.4. Elemental composition of slag samples. The "other" composition can be attributed to the organics and soil remnants that make up the balance of the slags. Note the high Pb content in sample 2-7.

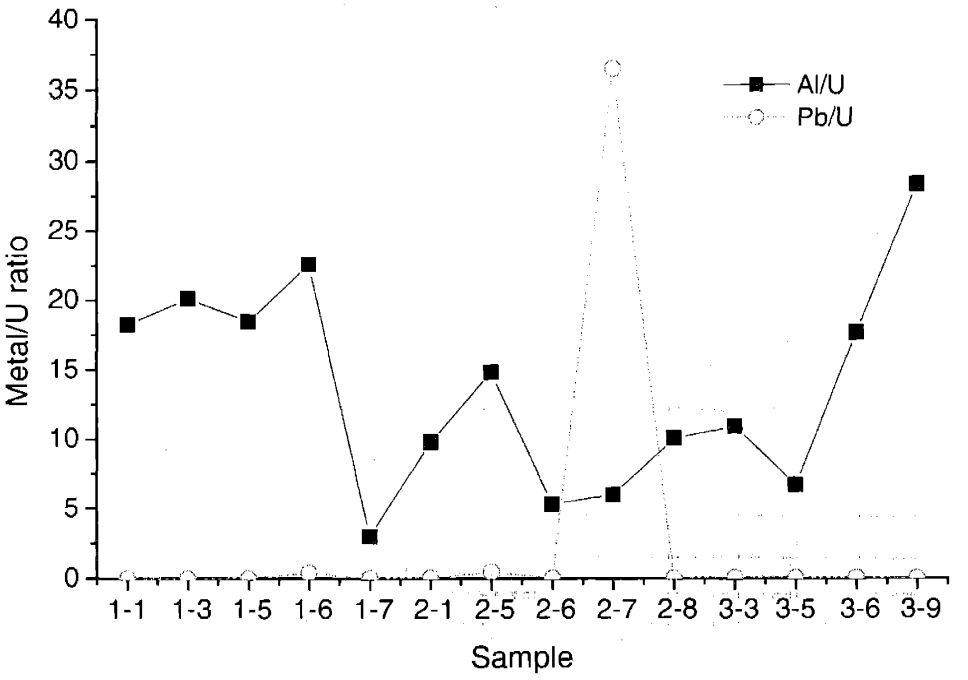

Figure 9.5. Metal/U ratios for Al and Pb.

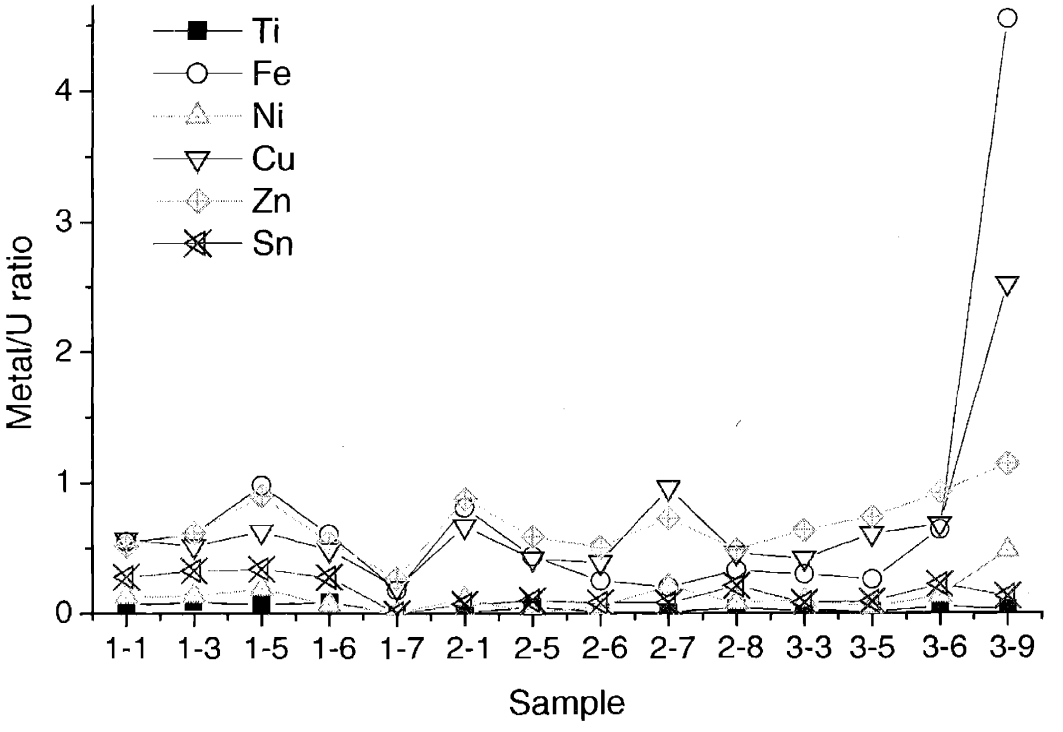

Figure 9.6. M/U ratios for remaining metal ions. These ratios are relatively constant with the exception of the surface sample 3-9, which has high Fe and Cu.

9.4.2 *XAS Analysis*

Speciation of the uranium in the three samples was determined using x-ray absorption spectroscopy (XAS), which utilizes a synchrotron-based x-ray source to probe local structure of various materials around a particular element. XAS samples were prepared from the pulverized powders. For each sample, approximately 20 mg of powder was mixed with biobeads to fill an aluminum window. The window was sealed with kapton tape.

Samples were scanned at the uranium L_3 edge to k=12. Data was collected on a Lytle detector. One scan of each sample was taken due to time constraints. Because of this, the useful k range for EXAFS analysis was limited to k =2-9. EXAFS analysis was performed using EXAFSPAK, ATOMS, and FEFF. Phase and amplitude functions were calculated using FEFF.

Analysis of the XANES spectra shows little variation in oxidation state between samples, all of which are a combination of U(IV) and U(VI) (Figure 9.7). EXAFS spectra and fits are shown in Figure 9.8. Further analysis of the EXAFS spectra indicates the uranium exists in two main phases. The surface samples show a mixture of uranyl and a metallic uranium compound (Figure 9.9). The oxygen peak at 1.8 Å is characteristic of the axial U-O bond in the uranyl structure, while the short bond distance between the central uranium atom and the element at the second peak indicates a metal-metal bond (Figure 9.10). Although aluminum was identified as the most prevalent metal species throughout the samples, two metal species were found to be present (Table 9.3). Both U-Al and U-Ti bonds were found. Percent composition of the two uranium phases in samples 1 and 3 was estimated by using the calculated coordination number for the $U\text{-}O_{ax}$ bond. A coordination number of N = 2 is expected for the pure uranyl species (Table 9.4).

In the interior samples, the U-O peak was either greatly degraded or not present (Figures 9.11 and 9.12). The two metal species were found to be the primary

form of U speciation beneath the surface. Bond lengths and coordination numbers were largely consistent for each compound (Tables 9.5 and 9.6).

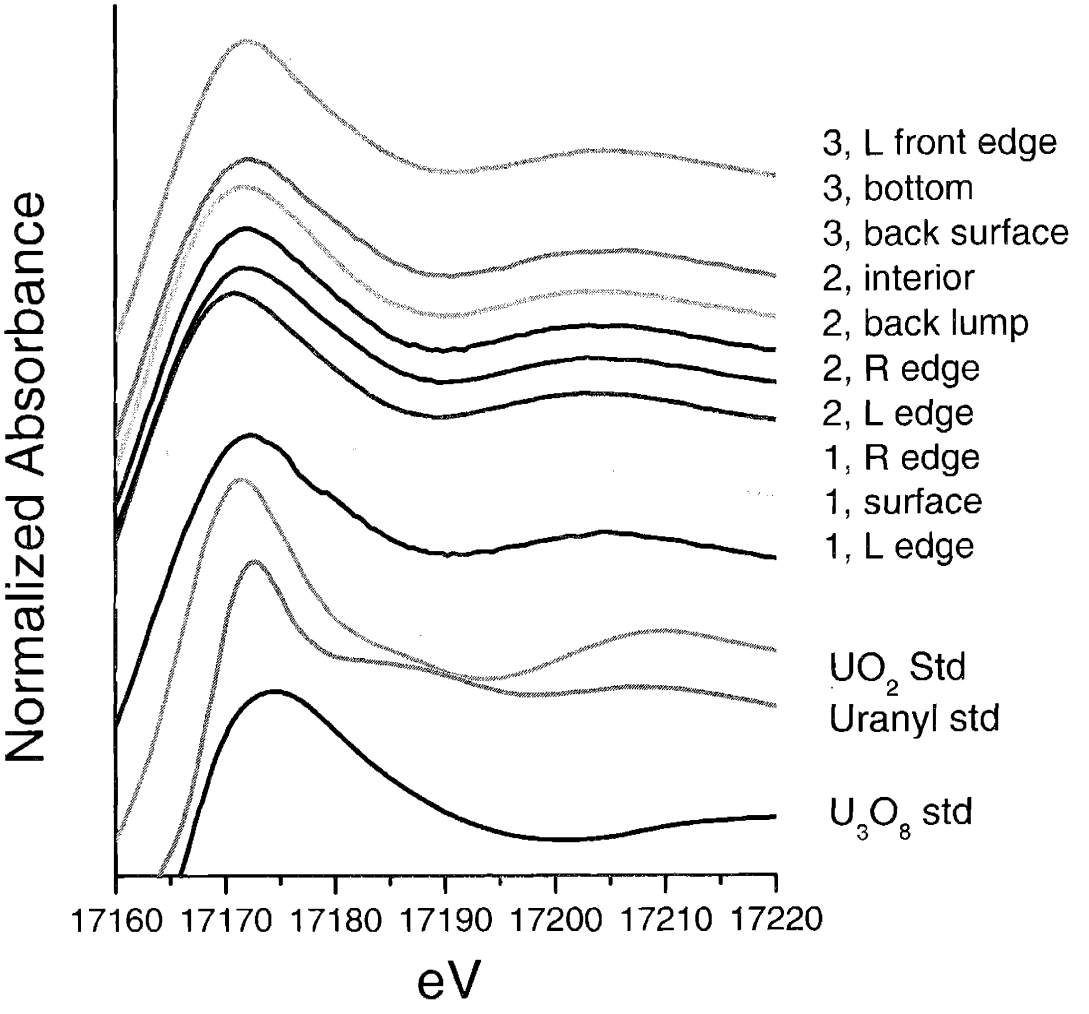

Figure 9.7. Uranium L_3 XANES spectra. The edge position varies among the samples, but tends to be U(IV) on average.

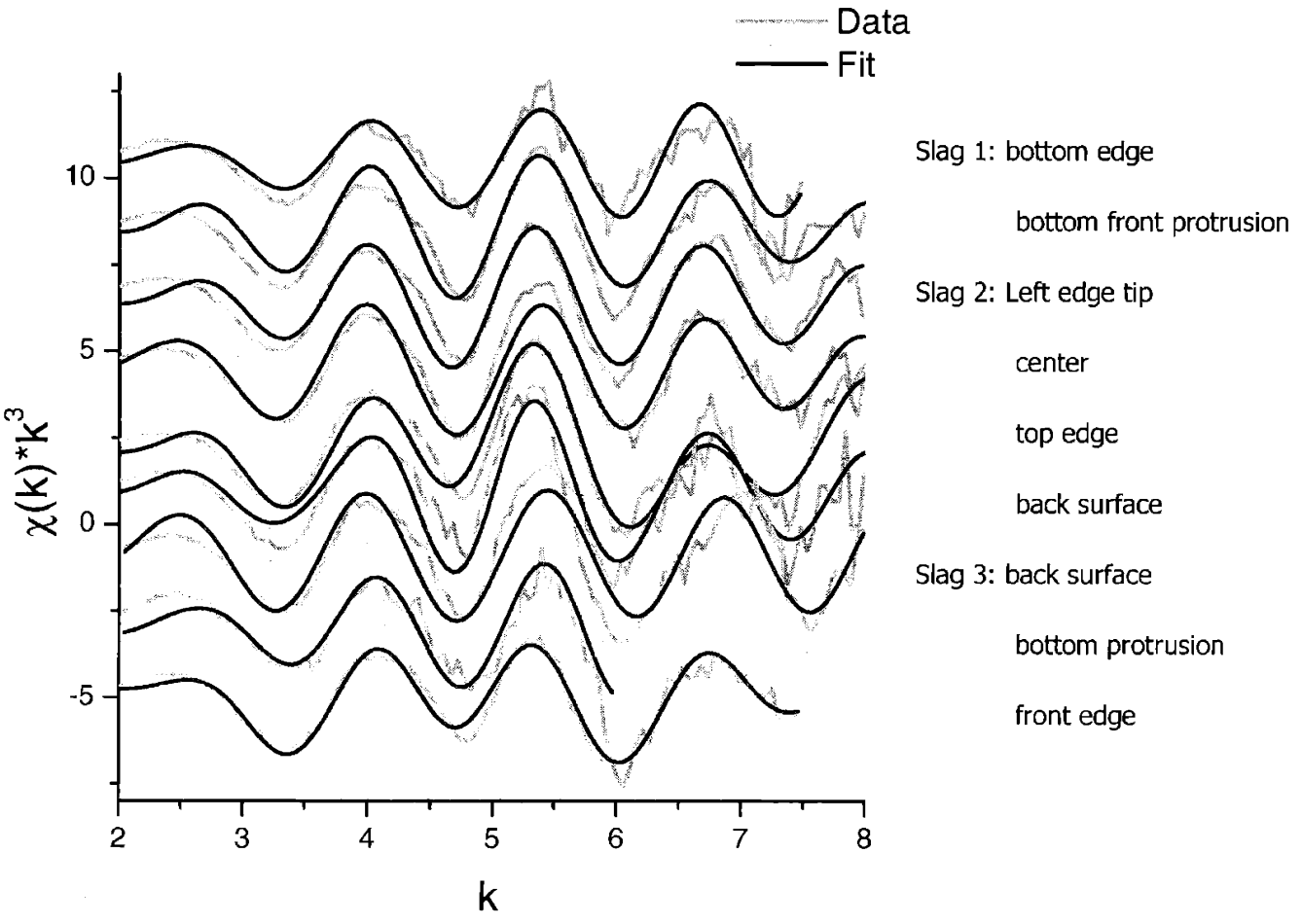

Figure 9.8. EXAFS data and fit

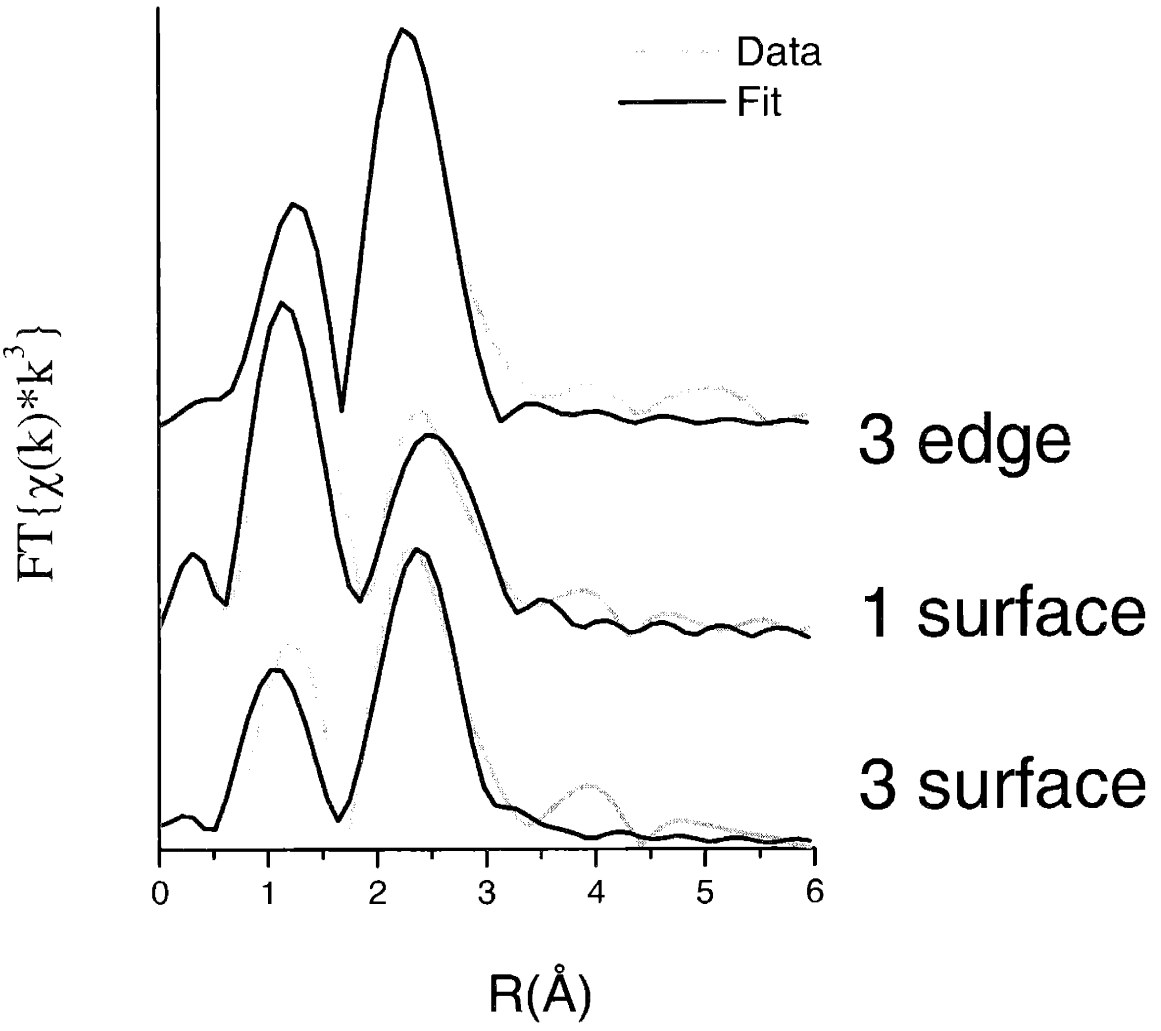

Figure 9.9. Fourier transforms and fits for surface samples. Spectra show the presence of mixed uranyl and metal compound species. The 3 edge sample is U-Ti, while the others are U-Al.

Sample	bond	N	R(Å)	σ^{2}
3, edge	U-O	1.0	1.79	0.005
	U-Ti	3.0	2.89	0.018
1, surface	U-O	1.2	1.80	0.005
	U-Al	1.5	3.19	0.005
3, surface	U-O	0.7	1.75	0.009
	U-Al	3.2	3.11	0.010

Table 9.3. Bond lengths and coordination numbers calculated for the spectra of the surface samples.

Sample	$N(O_{ax})$	% UO_2^{2+}
3, edge	1.0	50
1, surface	1.2	60
3, surface	0.7	35

Table 9.4. Percent of uranium present in uranyl phase.

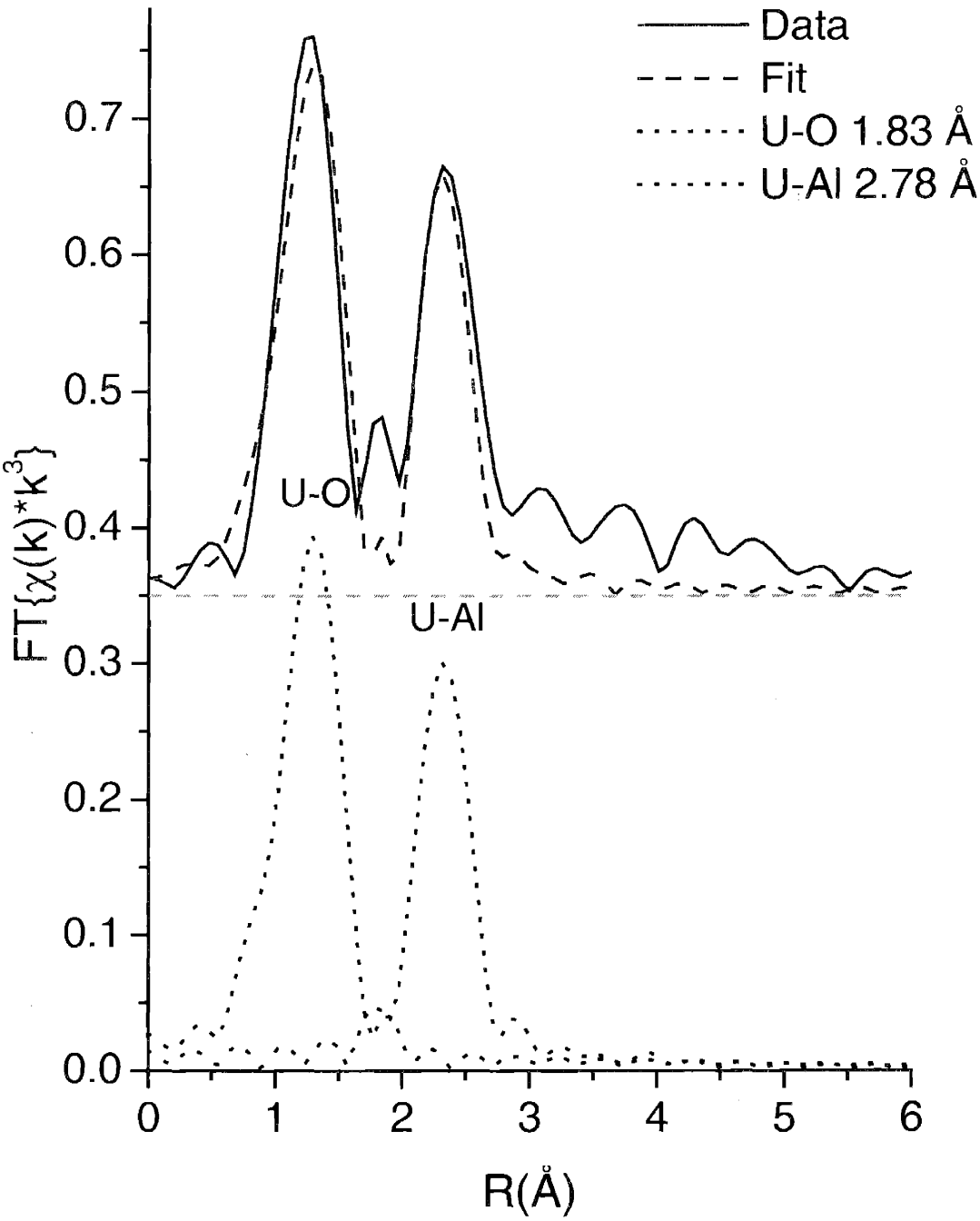

Figure 9.10. Deconvolution of the EXAFS fit for Sample 1. The U-O bond length of 1.8 Å is characteristic for the uranyl structure. The relatively short U-Al bond distance indicates a metallic structure.

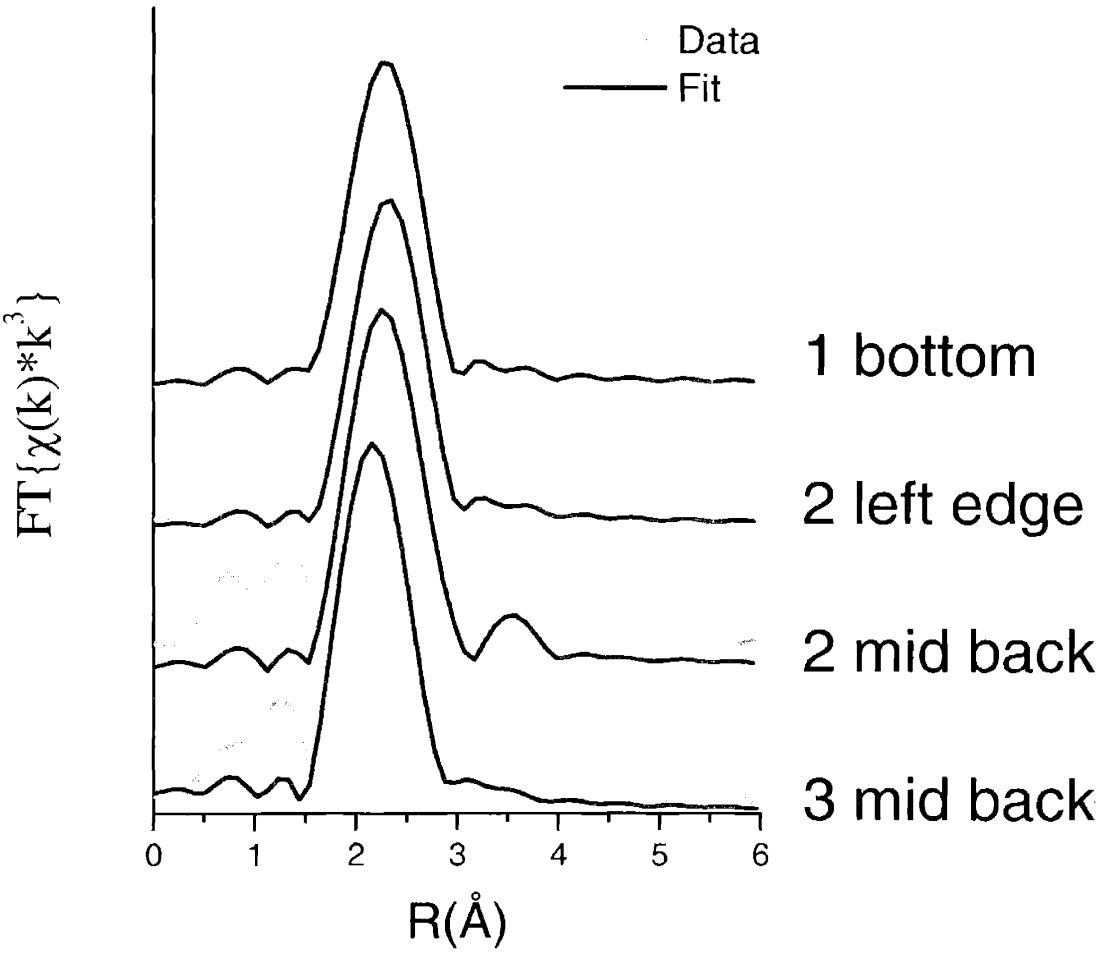

Figure 9.11. Fourier transforms and fits for U-Ti compound samples from below the slag surfaces. While the uranium in these samples is primarily in the metallic form, a small peak corresponding to the U-O bond of the uranyl ion can be seen, evidence of the start of formation of that phase in the subsurface.

Sample	bond	N	R(Å)	σ^2
1, bottom edge	U-Ti	4.1	2.85	0.018
2, L edge	U-Ti	3.3	2.88	0.015
2, mid back	U-Ti	3.4	2.85	0.014
3, mid back	U-Ti	2.8	2.77	0.012

Table 9.5. Bond lengths and coordination numbers calculated from U-Ti fits. The bond lengths and coordination numbers are both consistent through the samples.

Sample	Bond	N	R	σ^2
1, bottom	U-Al	2.3	3.08	0.003
2, interior	U-Al	6.1	3.04	0.013
3, protrusion	U-Al	2.8	3.09	0.012

Table 9.6. Bond lengths and coordination numbers calculated from U-Al fits. While the bond lengths and coordination numbers of samples 1 and 3 are similar. Sample 2 shows a similar bond length, but much more Al is present. This sample also showed evidence of the nascent U-O uranyl bond.

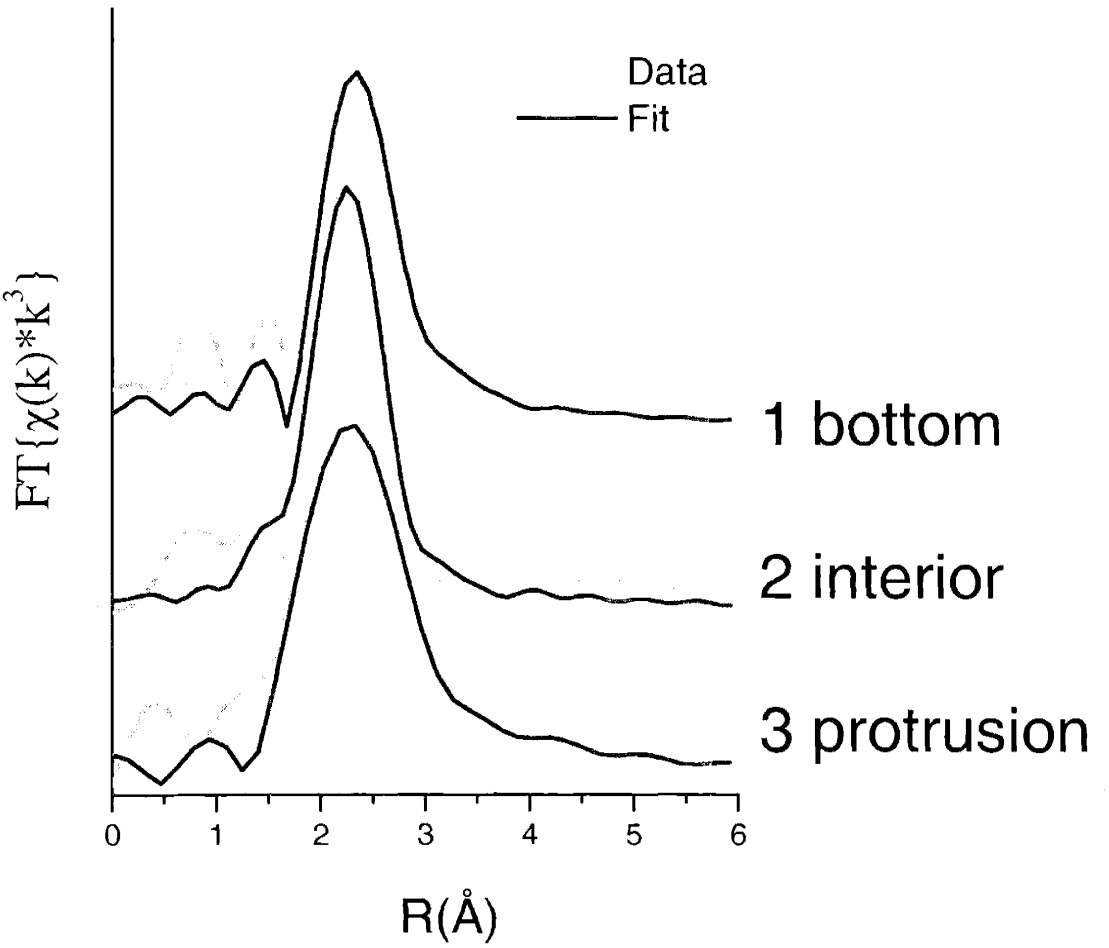

Figure 9.12. Fourier transforms and fits for U-Al compound samples from below the slag surfaces. The U-O bond peak is less obvious in these spectra, though it can be seen somewhat in 2 interior.

9.5 Conclusions

Samples of the three pieces of mixed phase materials containing uranium were analyzed for elemental content using ICP-AES and uranium speciation using x-ray absorption spectroscopy. Elemental composition varied widely between the samples, but several metals were consistently found to be present, including Ti, Zn, Cu, Ni, Fe, Sn, and Nb. While the ratios Al and Pb varied widely, the remaining metal ratios were more consistent throughout the samples.

Results from XANES data show the uranium is a mixture of uranyl (UO_2^{2+}) and a less oxidized species. The other species is identified as a metallic uranium compound by EXAFS analysis. Though the dominant metallic species was consistently Al, the uranium was found to be bonded to both Al and Ti. Phase composition ranged from 33% to 50% uranyl in the surface samples, indicating high uranium mobility when the samples are environmentally exposed. In the interior samples, the two metallic uranium compounds were the primary uranium phase, though a nascent U-O peak could be seen in many samples, revealing the formation of the uranyl species. In addition to their environmental instability, the samples showed little proliferation resistance and could be dissolved with relative ease using commonly available chemicals.

9.6 Acknowledgements

Part of this work was performed under the auspices of the U.S. Department of Energy (DOE) by the University of California Lawrence Livermore National Laboratory under Contract No. W-7405-Eng-48. This work was done (partially) at SSRL, which is operated by the Department of Energy, Division of Chemical Sciences. XAS data was collected with the assistance of Karen Noyes and Lisa Mullen at MIT and Erik Nelson at LLNL.

10 Conclusion: Using Actinide Speciation in Environmental Remediation

10.1 Abstract

The distribution coefficient (K_d) is a rough measure of contaminant mobility in environmental systems, however neither the empirical nor theoretical determination of K_d is well defined. Although we understand the limitation of the K_d parameter, the reality is that the K_d is often the only parameter used in environmental fate and transport models to account for the mobile fraction of contaminate in predicting total risk. In this paper, we present a fresh approach to calculating the K_d using a combination of empirical and theoretical modeling. The paper provides two examples of actinide K_d determination: the dissolution of UO_2 and U_3O_8 under different pH and carbonate conditions and the sorption of Np to goethite, montmorillonite and tuff. The modeling results predict the expected solution species and initial data points for the analysis of experimental results. The experiments evaluate the change in actinide solution concentration over time, permitting a kinetic based determination of equilibrium conditions. The results show that current methods for evaluating actinide transport/solubility in the environment do not accurately predict the empirical results. Our speciation method is shown to produce equilibrium data that can be used to develop more accurate K_d determination and to validate environmental models. This combination of empirical laboratory methods and speciation modeling improves upon current environmental remediation methods, and provides an improvement over direct K determinations. The method can also be used with advanced remediation techniques to target the critical actinide chemical forms that require treatment.

10.2 Introduction

There has been a large effort in evaluating U, Pu, and other actinide species present in the environment [1-4]. The works identify important actinide phases and processes in the environment, namely precipitation, sorption, complexation, and colloid formation. The papers also stress that speciation dictates the environmental behavior of the actinides allowing an analysis of mobility, toxicity, and risk arising. Actinide speciation has been incorporated into performance assessment models for evaluating actual and potential repositories. However, the use of actinide speciation in environmental remediation has been limited.

The general plan for remediation of a site contaminated by actinides includes field radiological assessment, testing and verification surveys, and risk assessment modeling. The main goal is to determine the actinide concentration along with the near and far field conditions. Once contaminants are identified, evaluation methods are established to develop concentration levels that define the endpoint.

Current analysis of actinide for remediation relies upon distribution coefficients (K_d) in evaluating mobility. The K_d is defined as the concentration of a contaminant in the solid S divided by the solution phase concentration C ($S=K_dC$) and is usually expressed in mL/g. This relationship is used in analysis models for estimating the actinide concentration in soil and solutions. The values for K_ds can vary greatly and are strongly dependent upon soil and solution chemistry even if consistent methods are used [5,6]. Incorporating speciation can mitigate the well-known limitations inherent to K_ds in describing environmental behavior and provide a direct determination of the chemical forms of the mobile actinides [7].

Actinide speciation can be integrated into remediation efforts mainly the determination of solubility and solution phase concentration [8]. The resulting data can be used to develop site survey methods, target radionuclides of concern, and provide data for input into dose assessment codes. A new method based on actinide

speciation described in this paper employs a combination of modeling and laboratory analysis to critically evaluate the actinide speciation through the following:

1. Geochemical modeling
2. Laboratory experiments to evaluate change in actinide solution concentration over time
3. Utilization of modeling results to analyze experimental data

In this work the speciation method is used to evaluate the behavior of U solids and Np sorption. Geochemical modeling of the U and Np under the experimental conditions is performed. The variation of actinide solution concentration over time is experimentally determined. The evaluation of the U solids provides a simple example involving a system that can be easily modeled and understood. The effect of pH and carbonate concentration is examined on the solution speciation of U from the dissolution of UO_2 and U_3O_8. The Np study is more complicated since sorption to goethite, montmorillonite and tuff solid phases are examined. The sediments are relatively complex and are not supported by thermodynamic data for the initial modeling.

Through a combination of modeling and kinetic experiments, the actinide equilibrium solution concentration can be determined over a wide range of solution conditions. The speciation data is compared against resulting distribution coefficients, showing where large variations in distribution values may occur depending upon the evaluation conditions. Both the U and Np experiments show that a single K_d cannot describe actinide behavior and the determination of the K_d is dependent upon experimental conditions. This provides evidence for the utility of incorporating actinide speciation in environmental remediation to produce meaningful and functional data.

10.3 Experimental

10.3.1 Modeling

The geochemical code CHESS (CHemical Equilibrium and Speciation with Surfaces) was used to calculate U and Np speciation from the examined conditions in this work. CHESS is a robust model for examining speciation of actinides and auxiliary species in complex, multi-phase solutions [9]. The main database for CHESS is from the literature [10,11]. Solution parameters and actinide concentrations are the input parameters. For the modeling of UO_2 and U_3O_8 the solid phase concentrations, CO_2 partial pressure and pH were varied. For the Np study the solution speciation was modeled against pH. No values were available for determining Np sorption to the examined solids. The values for the numerical precision and the iteration thresholds were adapted to reach stability within a reasonable time.

10.3.2 U solid dissolution

The U_3O_8 samples were prepared by sintering UO_2 purchased from Alpha Aesar in a furnace for three hours at 600° C under normal atmosphere. X-Ray diffraction confirmed formation of U_3O_8 using a Rigaku RU300 x-ray generator with a 185 mm diffractometer operating at 60 kV and 300 mA (18 kW). The pH ranged from 4.5 to 7.5 and the atmospheric conditions were 20% O_2 with 0.032%, 1% and 10% CO_2 with the remainder being Ar. The carbonate concentration is from $\log [CO_3^{-2}] = -17.56 + \log(P_{CO2}) + 2pH$ [12].

Dissolution experiments on 0.3 g of solid U samples were performed in 100 mL of 0.1 M $NaClO_4$ in a round-bottomed, three-necked flask. The solutions were sampled by removing 5 mL aliquots at regular intervals, every three days for the first

two weeks and weekly thereafter, for 75 days. Each 5 mL sample was passed through a 0.45 μm filter. A 4 mL sample was removed and diluted with 23 μL of concentrated HNO_3. Inductively Coupled Plasma Atomic Emission Spectroscopy (ICP-AES) with a Spectroflame ICP D calibrated with NIST traceable standards was used to determine the U solution phase concentration.

10.3.3 Np sorption experiments

Goethite, montmorillonite and tuff materials were obtained respectively from Alfa AESAR, Aldrich and Topopah Springs Site, NV. The samples were sieved to obtain particles within the size range 45-75 μm. The ^{237}Np was obtained from Argonne National Laboratory (>99% $^{237}NpO_2$, calcined at 500°C) and dissolved in nitric acid and oxidized to the pentavalent state.

The proton exchange capacity of the solid phases was determined by titration using a 736 GP Titrino instrument from Metrohm combined with Brinkmann Titrino Workcell software version 4.0. The electrode was calibrated with a three point method using pH 7, 4, and 10 buffers. The soils were conditioned with 0.1M NaOH, washed with de-ionized water and freeze dried. Around 1 g soil samples were added to 40 mL of 0.1M $NaClO_4$ and titrated with 0.1M HCl under Argon.

Batch sorption experiments were conducted to investigate Np sorption kinetics under Argon atmosphere at 25 °C at pH 7 and pH 9. The Np concentration was evaluated over 7 days by removing samples and determining the Np concentration through alpha scintillation counting with a Packard 2900 Tricarb.

10.4 Results and Discussion

10.4.1 Modeling

The modeling results indicate at equilibrium the solution phase concentration of U will be similar for both UO_2 and U_3O_8. This result is extremely useful for the analysis of dissolution experiments since it provides an initial point for the examination of the experimental system. Evaluation of the total U solution phase concentration for the examined conditions demonstrates the importance of carbonate (Figure 10.1).

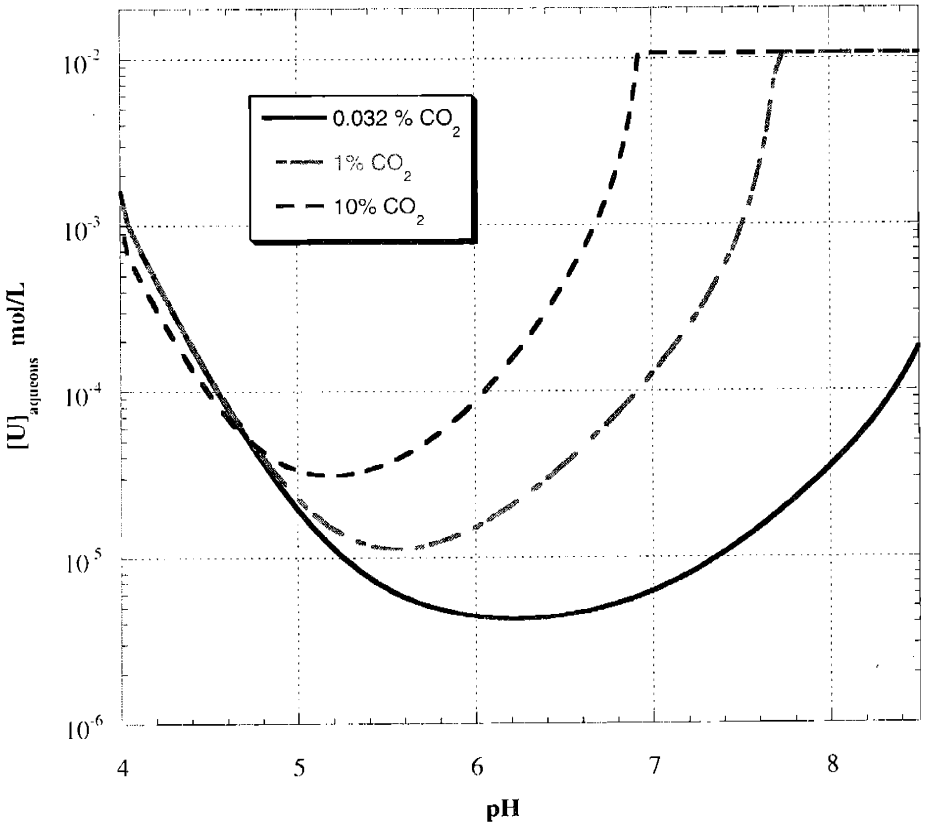

Figure 10.1. Solution phase U concentration from the dissolution of 3 g/L U_3O_8 under different CO_2 partial pressures

Overall, the solubility is driven by the oxidation of the U to the uranyl species. At lower pH, the free uranyl and hydroxide species dominate in the solution phase. As the carbonate concentration increases with increasing pH and CO_2 partial pressure, uranyl carbonate species become prominent in the solution phase. Formation of the carbonate species increases the solution minimum and shifts it to lower pH. The plateau reached at high pH is due to the complete dissolution of the U_3O_8. The modeling results show that a K_d would vary over 5 orders of magnitude under the conditions examined, making it difficult to choose a single K_d for U. Even for the 0.032% CO_2 condition the distribution coefficient would vary from $7x10^5$ mL/g to $2x10^3$ mL/g.

For Np speciation modeling the predominance of the pentavalent Np is found from pH 7-9. The database does not include the solid phases examined in the experiment, so sorption of Np is not considered in the model. This prevents the direct calculation of Np solid phase speciation and determination of corresponding distribution between the solid and solution. However, the modeling shows the expected dominance of pentavalent neptunyl in the solution phase and is applicable to analysis of the experimental results.

10.4.2 U dissolution

The experiments demonstrate that the U solution phase concentration is dependent upon the solid specie, the pH, the CO_2 partial pressure, and the time at which the measurement was taken. The dissolution of the U phases can be fit to a 1st order equation:

$$[U]_{sol} = [U]_{eq}(1 - e^{-kt}) \qquad \text{Eq. 10.1}$$

where $[U]_{sol}$ is the measured U solution concentration at time t and $[U]_{eq}$ is the U solution concentration at equilibrium. Modeling results are used to provide initial data for analysis using equation 10.1. This provides the ability to determine equilibrium conditions even when final states are not reached. The equilibrium U concentration values determined from Figure 10.2 using equation 10.1 are $7.23\pm0.37\times10^{-5}$ M for U_3O_8 and $5.42\pm0.51\times10^{-5}$ M for UO_2. Both these values are in excellent agreement with the modeling data presented in Figure 10.1.

While the use of equation 10.1 simplifies the determination of U solution concentration at equilibrium, evaluation of K_d is not straightforward (Figure 10.2). Without regard for equilibrium or initial specie, K_d analysis would provide a wide range of values. The time at which the measurement is made is particularly crucial since the K_d should describe a system at equilibrium. For U_3O_8 the K_d value is consistent after 500 hours. For UO_2, with slower dissolution kinetics, the measured K_d decreases during the measurement period. To evaluated equilibrium conditions for the U dissolution equation 10.1 can be used. This provides an experimental method to evaluate solution concentrations for actinide species with slow kinetics.

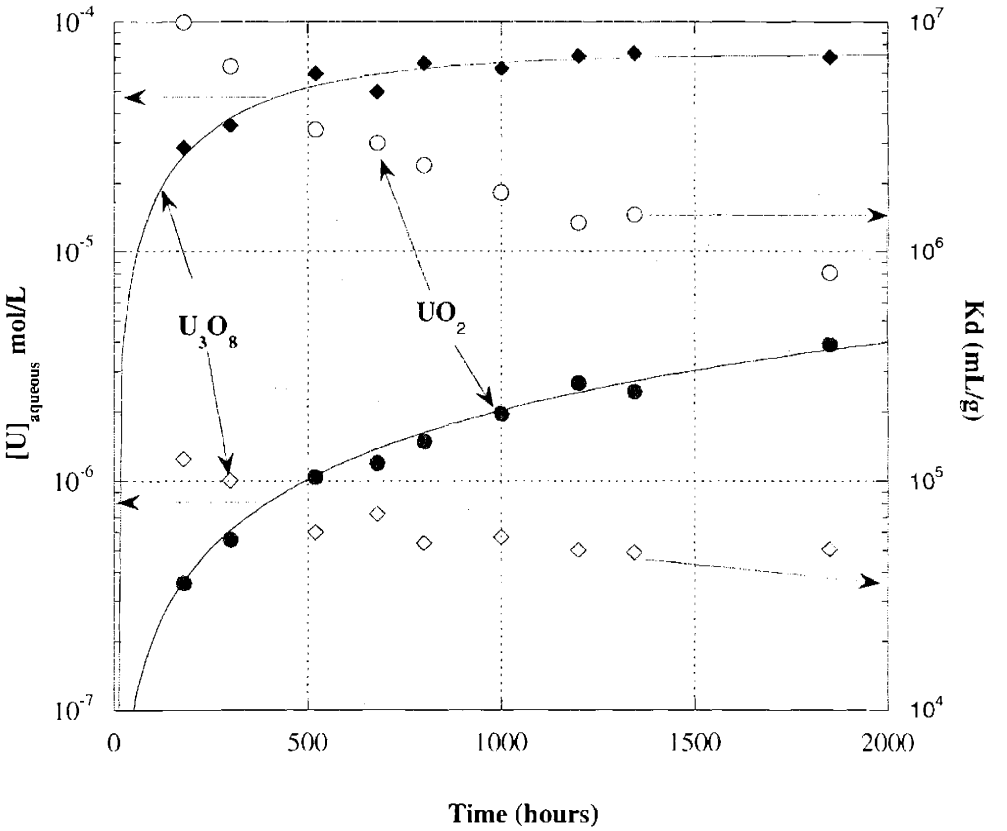

Figure 10.2. Comparison of U solution phase concentration and K_d for U_3O_8 and UO_2 at pH 4.7 under 0.032% CO_2.

Similar variations in U solution concentration with time from the dissolution of UO_2 under various pH (Figure 10.3) and CO_2 partial pressures (Figure 10.4) are also observed. As with the analysis for UO_2 at pH 4.7 under 0.032 % CO_2 a decrease of K_d with time is evident from the continued increase in U solution concentration. Applying equation 10.1 to the data produces U equilibrium concentrations with agreement to the modeled data, with error from 5-10 %. This again shows the utility of modeling and experiment for determining U equilibrium solution concentrations rather only direct K_d evaluation.

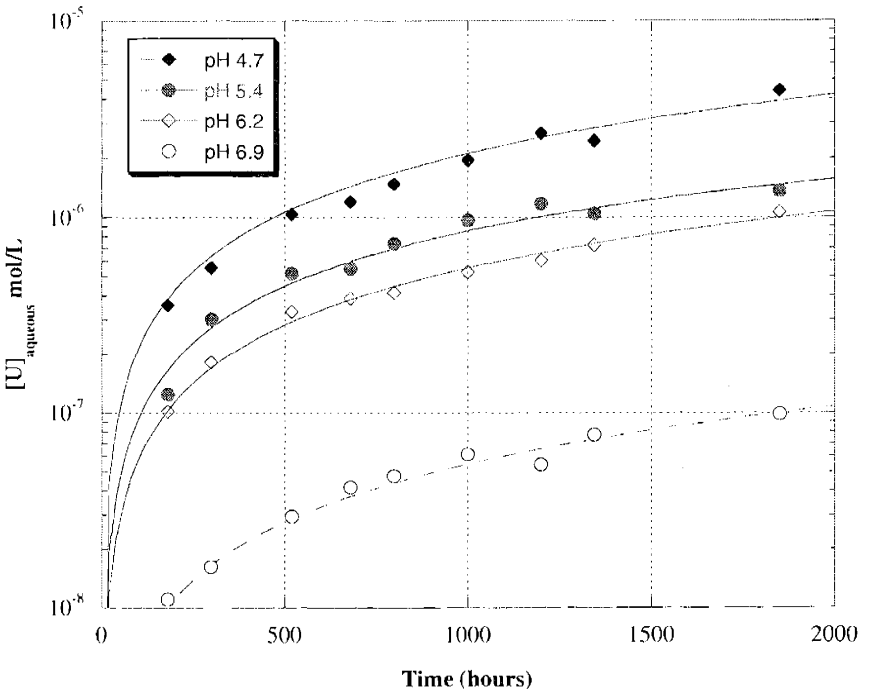

Figure 10.3. Dissolution of UO_2 at various pH under 0.032% CO_2

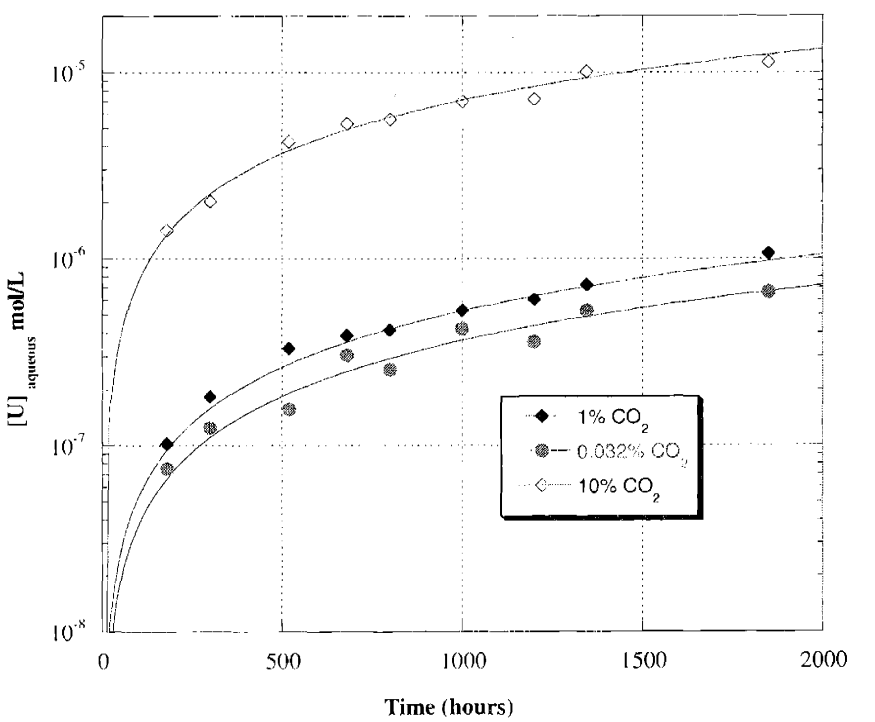

Figure 10.4. Dissolution of UO2 at pH 6.1±0.1 under various CO2 partial pressures

10.4.3 Np sorption

The results for the Np sorption studies reveal a kinetic component in the evaluation of the Np solution concentration (Figure 10.5). The equilibrium concentration can be evaluated by:

$$[Np]_{sol} = [Np]_{eq} + [Np]_{sorbed} * e^{-kt} \qquad \text{Eq. 10.2}$$

where $[Np]_{sol}$ is the Np solution concentration at the measured time, $[Np]_{eq}$ the Np solution concentration at equilibrium and $[Np]_{sorbed}$ is the Np concentration sorbed to the mineral phases. Unlike the U experiments, equilibrium is rapidly achieved in the Np experiments since the Np is proceeding from solution to solid phase. While K_d can be determined, the results are similar to U in that pH will affect the values. By using a speciation analysis, experimental data can be used to produce constants for a robust evaluation of Np speciation under a range of conditions.

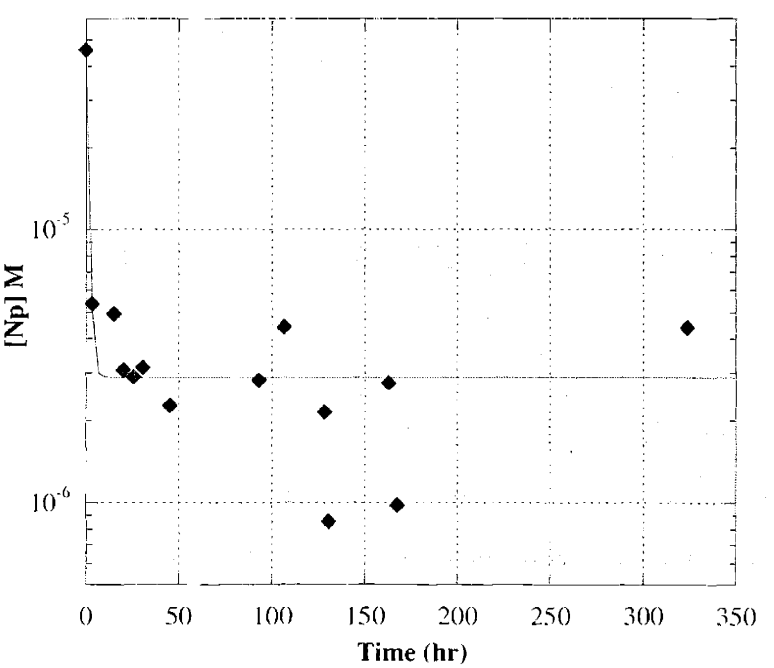

Figure 10.5. Sorption of Np to Tuff at pH 9

The Np equilibrium species solution concentration is composed of all aqueous species. The initial modeling determined only the free ion is expected to present in solution, therefore the equilibrium concentration provides the free ion concentration. Using equation 10.2, the data in Figure 10.5 gives $[Np]_{eq}$= 2.89±0.37x10^{-6} M and $[Np]_{sorbed}$ = 4.31±0.13x10^{-5} M. Through the proton exchange capacity, the concentration of sediment can be determined and used to produce equilibrium constants 12].

The constants are based on the reaction

$$Np_{free} + Solid \Leftrightarrow Np - Solid \qquad \text{Eq. 10.3}$$

with a complexation constant equal to:

$$K = \frac{[Np]_{sorbed}}{[Np]_{free} * [Solid]_{free}} = \frac{[Np]_{sorbed}}{[Np]_{free} * ([Solid]_{tot} - [Np]_{sorbed})} \qquad \text{Eq. 10.4}$$

The complexation constants (Table 10.1) can be used to model the sorption of Np to sediments, determining solid and solution phase species. Additionally, K_d values for a range of conditions that correspond with the aqueous phase speciation can be derived. Conditions were the aqueous Np species include those not examined in the experimental system (i.e., carbonate and hydroxide species in the current example) may not produce valid speciation results due to the formation of solid ternary species. Experiments would need to be performed under the relevant conditions to provide constants suitable for modeling. If speciation is not

considered, as is case with direct K_d measurements, errors would result and the produced data would not accurately reflect Np behavior.

Solid	log K	Proton exchange capacity (meq/g)
Goethite	6.27±0.22	0.228±0.018
Tuff	6.71±0.25	0.165±0.028
Montmorillonite	6.94±0.27	0.195±0.067

Table 10.1. Complexation constants for the Np with solids

10.5 Discussion

A combination of modeling and experiments can provide data for evaluating different actinide species for a variety of solution conditions and solid phases. The resulting solution concentration results can be directly incorporated into models evaluating the environmental consequence of actinides [13]. In addition, K_d values for specific conditions can be produced. These values will be responsive to the conditions evaluated and provide an improvement over existing methodologies for determining K_d.

The inclusion of speciation can also improve actinide detection and analysis of remediation schemes. Through the speciation, advance and specific procedures for determining actinide concentration in a sample can be developed. For example, if a known fraction of actinides reside in a particular sediment phase, then extraction and detection procedures can be developed to target that phase. This can result in lower

detection limits and reduced error, vastly improving the selected remediation method.

Inclusion of speciation will prove critical with the use of advance remediation techniques such as bioremediation or active barriers. These techniques rely heavily on interaction with a distinct chemical form of the actinide or operate only on a specific oxidation state. The kinetics and final chemical forms will be dominated by the actinide speciation. The described speciation method will enhance the efficacy of these techniques through the enhanced understanding of the important chemical forms and their dynamics under given conditions.

There is obviously a pressing need to formally incorporate speciation into actinide remediation. The use of modeling and laboratory studies provide a strong basis for a reliable analysis of actinide chemical forms present in a contaminated site. When applicable, inclusion of advanced techniques, such XAFS, should be applied to actinide remediation projects. This would provide support of the inclusion of species and help confirm the initial modeling and experimental results. Combining and utilizing all existing efforts would provide the greatest benefit to actinide remediation.

10.6 References

1. Kim, J.I.: Chemical Behavior of Transuranic Elements in Natural Aquatic Systems, Handbook on the Physics and Chemistry of the Actinides, A.J. Freeman and C. Keller Eds., Elsevier Publishers, 1986, 413-455.
2. Von Gunten, H.R., and Benes, P.: Speciation of Radionuclides in the Environment. Radiochim. Acta, **69**, 1-29 (1995).
3. Silva, R.J. and Nitsche, H.: Actinide Environmental Chemistry, Radiochim. Acta, **70/71**, 377-396 (1995).
4. Moulin, V and Moulin, C.: Radionuclide Speciation in the Environment: A Review. Radiochim. Acta, **89(11-12)**, 773-778 (2001).
5. Porro, I., Newman, M. E., Dunnivant, F. M.: Comparison of Batch and Column Methods for Determining Strontium Distribution Coefficients for Unsaturated Transport in Basalt. Environmental Science and Technology, **34(9)**, 1679-1686 (2000).
6. Bethke, C. M. and Brady, P.V.: How the K_d approach undermines ground water cleanup. Ground Water, **38(3)**, 435-443 (2000).
7. J.F. McCarthy, K.R. Czerwinski, W.E. Sanford, P.M. Jardine, and J.D. Marsh: Mobilization of Actinides from Disposal Trenches by Natural Organic Matter. J. Contam. Hydro. **30**, 49 (1998).
8. J. Plaue and K.R. Czerwinski: Actinide Speciation in Environmental Remediation. Journal of Nuclear Science and Technology (2002) 461-465.
9. J. van der Lee (1998) Thermodynamic and mathematical concepts of CHESS. Technical Report Nr. LHM/RD/98/39. CIG-Ecole des Mines dc Paris, Fontainebleau, France.
10. Delany, J.M., and Lundeen, S.R.: The LLNL Thermodynamic Database. Technical Report UCRL-21658, Lawrence Livermore National Laboratory (1990).
11. Dzombak, D.A. and Morel, F.M.M.: Surface Complexation Modeling. Hydrous Ferric Oxide. John Wiley and Sons, New York (1990).

12. J.I. Kim and K.R. Czerwinski: Complexation of Metal Ions with Humic Acid: Charge Neutralization Model. Radiochimica Acta **73**, 5 (1996).
13. Kamboj S; LePoire D; Yu C.: External Exposure Model in the RESRAD Computer Code. Health Physics, **82(6)**, 831-9 (2002).